Synthesis and Characterization of NbO_x Thin Film

A Thesis Submitted to the College of
Graduate and Postdoctoral Studies
In Partial Fulfillment of the Requirements
For the Degree of Master of Science
In the Department of Mechanical Engineering
University of Saskatchewan
Saskatoon
Canada

By

Nazmul Hossain

© Copyright Nazmul Hossain, April, 2019. All rights reserved.

Permission to Use

In presenting this thesis in partial fulfillment of the requirements for a postgraduate degree from the University of Saskatchewan, I agree that the Libraries of this University may make it freely available for inspection. I further agree that permission for copying of this thesis in any manner, in whole or in part, for scholarly purposes may be granted by the professor who supervised my thesis work or, in their absence, by the College of Graduate and Postdoctoral Studies (CGPS), Head of the Department or the Dean of the College in which my thesis work was done. It is understood that any copying or publication or use of this thesis or parts thereof for financial gain shall not be allowed without my written permission. It is also understood that due recognition shall be given to me and to the University of Saskatchewan in any scholarly use which may be made of any material in my thesis.

Requests for permission to copy or to make other use of material in this thesis in whole or part should be addressed to:

Head of the Department of Mechanical Engineering
57 Campus Drive,
University of Saskatchewan
Saskatoon, Saskatchewan, S7N 5A9
Canada

OR

Dean
College of Graduate and Postdoctoral Studies
University of Saskatchewan
116 Thorvaldson Building, 110 Science Place
Saskatoon, Saskatchewan, S7N 5C9

Canada

Abstract

Niobium Oxides (NbO_x) thin films have been deposited on silicon (100) and quartz substrates by magnetron sputtering using metallic Nb target in an optimized argon-oxygen atmosphere. To date, suitable deposition conditions for crystalline NbO_x thin films by reactive sputtering techniques have not been established. Therefore, this work investigates the dependence of structure-property relations on the key deposition parameters towards establishing optimum deposition conditions for the growth of NbO_x crystalline films. It is found that a substrate temperature of 720 °C, low gas pressures of 8 mtorr and a target to substrate distance of 45 mm gives NbO_x thin films with good homogeneity and a high degree of crystallinity. X-Ray Diffraction (XRD) and Raman spectroscopy confirmed the tetragonal phase of NbO_2 and orthorhombic phase of Nb_2O_5 for similar deposition temperatures. Scanning Electron Microscopy (SEM) observations indicate that NbO_2 has a unique nanoslice structure while Nb_2O_5 has a flake-like structure. Effect of post deposition annealing on the structural properties are also investigated in this dissertation. It is found that structural changes in NbO_2 samples are prominent after annealing in air or Ar atmosphere. In contrast, well crystalline Nb_2O_5 samples do not show significant changes after annealing in air atmosphere. However, amorphous Nb_2O_5 can be transformed to tetragonal NbO_2 after annealing in Ar atmosphere (reduction). The electrical conductivity and optical transmittance of the films have been investigated and found to be dependent on the oxygen gas content; the conductivity increases, and the optical transmittance decreases with increasing O_2 gas content. Optical constants of the films were calculated by fitting model calculations to experimental transmittance data using the modified Swanepoel technique. The nanohardness and stress in the films were measured by nanoindentation and an optical profilometer, respectively. Nano hardness and stress in the film show no large dependence on the oxygen gas content except at high oxygen gas content. V being one of the prominent transition metals, is doped with NbO_2 to evaluate the structural variations and the optical transmittance. It is found that higher sputtering power of V is required to be doped with NbO_2 and V contents have less effect on optical transmittance of NbO_2.

Acknowledgments

I would like to express my sincere gratitude to my supervisors, Professor Qiaoqin Yang and Professor Safa Kasap for their continuous instructions and encouragements. I will always be thankful to my supervisors for their immense support, patience and kind advice throughout my master's research.

I would like to appreciate my committee members Professor W.J. (Chris) Zhang and Professor Duncan Cree for their valuable advice.

I am very thankful to the members of this project Dr. Cyril Koughia, Dr. Zhang Chunzi, Ozan Günes and my group colleagues Dr. Yuanshi Li, Masoud Mohammadtaheri, Jesus Corona Gomez and Irtaza Khan for their insight discussion and advice of my research.

I would like to thank Mr. Zhao Nan Fang, Mr. Robert Peace and Dr. George Belev for their assistance, training and technical support during my experimental studies. I am thankful with Dr. Jason Maley for Raman spectroscopy training, Dr. Jianfeng Zhu for Grazing XRD training and Dr. Danielle Covelli for XPS measurements at the Saskatchewan Structural Science Center and Dr. Eiko Kawamura for SEM imaging at WCV Image Centre. I highly appreciate the financial support throughout this project by the Cisco, Natural Sciences and Engineering Research Council of Canada (NSERC), Canada Foundation for Innovation (CFI), and the University of Saskatchewan.

Finally, I would like to thank my parents and entire family members for their love and support all during my life and my aunt Dr. Jebunnaher and my cousin Dr. Jahangir for giving inspiration and motivations from my childhood.

To my beloved parents Amir Hossain and Nurunnaher Begum, my brother Fahim Hossain and my family members…

Table of Contents

Permission to Use……………………………………………………………………………… i
Abstract…………………………………………………………………………………... ii
Acknowledgments………………………………………………………………………......…iii
Table of Contents……………………………………..…………………………………….....iv
List of Tables……...…………………………………………………………….............................viii
List of Figures……...…………………………………………………….................................ix
Acronyms………………………………………………………………….............................xii

1 - Introduction 1

1.1 Motivation……………………………………………………………………………1

1.2 Objectives…………………………………………………………………………..3

1.3 Methodology……………………………………………………………………….3

1.4 Organization of Dissertation………………………………………………………..3

2- Literature Review 5

2.1 Niobium and Its Oxides……………………………………………………………5

2.1.1 Niobium (Nb).. …………………..5

2.1.2 Niobium Oxidation 7

2.1.2.1 Niobium Mono-Oxide (NbO) 8

2.1.2.2 Niobium Di-Oxide (NbO_2) 9

2.1.2.3 Niobium Penta-Oxide (Nb_2O_5) 11

2.1.2.4 Metastable Niobium Oxide s 13

2.1.3 Doping Niobium Oxide s 15

2.2 Deposition Techniques…………………………………………………………16

2.2.1 Fundamentals of Sputtering Deposition 17

2.3 Structural Characterization………………………………………………………..22

2.3.1 Raman Spectroscopy 22

2.3.2 X-ray Diffraction (XRD) 24

2.3.3 X-ray Photoelectron Spectroscopy (XPS) 26

2.4 Surface Morphology........ 27

2.4.1 Scanning Electron Microscopy (SEM) 27

2.4.2 Optical Profilometer 29

2.5 Mechanical Characterizations........ 31

2.5.1 Nano Indentation 31

2.6 Optical Characterization........ 33

2.6.1 Optical Spectrophotometer 33

2.7 Electrical Characterizations........ 35

2.7.1 Four Point Probe 35

3- Experimental Methods 38

3.1 Thin Film Deposition........ 38

3.1.1 DC/RF Sputtering 38

3.2 Experimental Design........ 39

3.3 Effect of Annealing........ 42

3.3.1 Post Deposition Annealing 43

3.4 Characterization Techniques........ 43

3.4.1 X-Ray Diffraction (XRD) 43

3.4.2 Raman Spectroscopy 44

3.4.3 X-ray Photoelectron Spectroscopy (XPS) 44

3.4.4 Optical Profilometer 45

3.4.4.1 Stress Measurement........ 45

3.4.5 Scanning Electron Microscope 46

3.4.6 Nano-Indentation 46

3.4.7 Four-Point Probe 47

3.4.8 Spectrophotometer 48

3.4.8.1 Optical Constants 49

4- Results and Discussion 53

4.1 Synthesis of NbO_x Thin Films by Magnetron Sputtering 53

4.1.1 Deposition Characteristics 53

4.1.2 Effect of Deposition Parameters on Structural Property 56

4.1.2.1 Effect of Oxygen Gas Contents 56

4.1.2.2 Effect of Substrate Temperature 61

4.1.2.3 Effect of Total Gas Pressure 63

4.1.3 Effect of Post Annealing 66

4.1.3.1 Annealing Nb Thin Films 66

4.1.3.2 Annealing NbO_2 in Ar Atmosphere 68

4.1.3.3 Annealing Amorphous Nb_2O_5 in Ar Atmosphere 70

4.2 Surface Morphology and Physical Properties of Niobium Oxide s 71

4.2.1 Surface Morphology 71

4.2.2 Mechanical Properties 74

4.2.2.1 Total Stress 74

4.2.2.2 Hardness and Young's Modulus 75

4.2.3 Electrical Properties 76

4.2.4 Optical Properties 77

4.3 V Doped NbO_2 films 82

5 – Summary, Conclusions and Future Works 88

5.1 Summary and Conclusions……………………………………………………………..88

5.2 Future Works………………………………………………………………………...90

References 91

List of Tables

Table 2-1: Physical Properties of Niobium and its Oxides 6

Table 2-2: Formation of Metastable NbO_x $(0<x<1)$ 14

Table 3-1: Deposition Parameters of NbO_x 41

Table 3-2: Deposition Parameters for V Doped NbO_2 42

Table 4-1: FWHM of NbOx 57

Table. 4-2: Crystal Size and Lattice Distortion Calculated from Bragg's Reflection 58

Table 4-3: Evolution of Mechanical Properties of NbO_x. 76

Table 4-4: Influence of Structure and Oxygen Concentration on Optical Properties of Niobium Oxide Films. 78

List of Figures

Figure 1-1:Metal Insulator Transition Temperature of Typical Transition Metal Oxides [4]. 2

Figure 2-1: Cubic Structure of Metallic Niobium[12] 5

Figure 2-2: Crystal Structure of NbO [43] 9

Figure 2-3:Structure of (a) Tetragonal and (b) Rutile NbO_2 [12] 10

Figure 2-4: Monoclinic Structure of (a) H- Nb_2O_5 (b) B- Nb_2O_5 [12].. 13

Figure 2-5: Schematic of Magnetron Sputtering 19

Figure 2-6: Glow discharge and electric circuit 20

Figure 2-7: Structure Zone Model for Energetic Deposition Proposed by Anders[110] 21

Figure 2-8: Rayleigh and Raman Scattering Process [112] 23

Figure 2-9: Principle of Bragg's Law [119].. 25

Figure 2-10: Principle of X-ray Photoelectron Spectroscopy (XPS) [123] 27

Figure 2-11 Schematic of SEM with Electron and X-Ray Optics [125]...................................... 28

Figure 2-12: Schematic of Optical Profilometer based on Interferometry.................................. 30

Figure 2-13: (a) Contact Geometry (b) Load Displacement Curve of Nano-Indentation 32

Figure 2-14. Schematic of Optical System [130] 34

Figure 2-15: Wavelength Range of Different Lights (internet) 35

Figure 2-16: Schematic of Four-Point Probe Configuration 37

Figure 3-1: Overall View of the Sputtering Deposition System 39

Figure 3-2: Nb Metallic Target (a) Before and (b) After Sputtering 40

Figure 3-3: Photograph of Universal Mechanical Tester for Nano-Indentation Investigation 47

Figure 3-4. (a) A sketch of the Exterior of Spectrophotometer[130]. (b) Sample Compartment . 49

Figure 4-1: (a) variation of cathode potential of Nb metallic target and (b) deposition rate as a function of oxygen gas content 54

Figure 4-2: Photograph of the Samples with Thin Films of NbO_2 and Nb_2O_5 on Quartz Substrates (a) Polycrystalline NbO_2, 1.5% O_2 (b) Polycrystalline Nb_2O_5 21% O_2 (c) Amorphous Nb_2O_5 8.5% O_2 Gas Contents 55

Figure 4-3: XRD Patterns of (a) NbO_2 (b) Nb_2O_5 With Different Oxygen Gas Contents 57

Figure 4-4: Raman spectrum of (a) NbO_2 and (b) Nb_2O_5 With Different Oxygen Gas Content .. 58

Figure 4-5: (a) XPS Survey Scan of the NbO_x Thin Films with Inset of Nb 4d and O 2p Peaks and (b) High Resolution XPS of Nb 3d Doublets 59

Figure 4-6: Nb 3d doublet of amorphous (i) Nb_2O_5 and (ii) NbO_2 61

Figure 4-7: GIXRD of NbO_x with Different Oxygen Gas Contents Deposited At 650°C 62

Figure 4-8: Variation of Surface Roughness for Different Temperature with Similar Thickness 62

Figure 4-9: XRD of NbO_x with Different Deposition Pressure 64

Figure 4-10: Effect of Deposition Pressure on Surface Roughness 65

Figure 4-11: Annealed Nb (Thickness~500 nm) at 700°C for (a) 2hrs and (b) 4hrs Respectively, Major Peaks are from O-Nb_2O_5. 66

Figure 4-12: Annealed Nb (thickness~1μm) at 700°C for (a) 2hrs and (b) 20hrs respectively. ... 67

Figure 4-13: Raman Spectra of Annealed Nb Thin Films at 700°C 68

Figure 4-14: XRD of Annealed NbO_2 Thin Films- (a) Annealed at 700°C for 10 min (b) Annealed at 700°C for 2 hr 69

Figure 4-15: Raman Spectra of the Annealed NbO_2 Thin Films at 700°C for 10 min 69

Figure 4-16: Annealed a-Nb_2O_5 thin films (a) for 2hrs (b) for 4 hrs 70

Figure 4-17: Raman Spectra of Annealed a-Nb_2O_5 Thin Films.. 71

Figure 4-18: SEM surface and cross-section micrographs of NbO_2 (a, b, c) and Nb_2O_5 (d, e, f) . 72

Figure 4-19: Surface roughness (Ra) of (a) thick (t > 2 μm) and (b) thin (t < 1μm) samples with two different deposition temperature.. 73

Figure 4-20: SEM Surface Micrograph of Annealed NbO_2. 74

Figure 4-21: Residual Stress for Different Oxygen Gas contents 75

Figure 4-22: Optical Transmittance of Niobium Oxide Films. Points are Experimental Data. Lines are Results of Calculations Using the Model Described in Paper. No Fit could be Achieved for Sample c-NbO_2 (1.5). Explanation of Notation: “c-” Stands for Crystalline and “a-” for Amorphous Samples, Number in Brackets are Oxygen Concentrations (in %). 78

Figure 4-23: Optical Absorption Coefficient in Niobium Oxide Films. (a) Semi logarithmic Presentation, (b) Tauc’s Presentation. Notations are the Same as in Figure 4-22... 79

Figure 4-24: Refractive Index of Niobium Oxide Films. Notations are the same as in Figure 4-22. 80

Figure 4-25: (a) Survey XPS Data (b) Nb 3d Spectra of V Doped NbO_2 Thin Films for (S1) 80W and (S2) 100W Sputtering Power of V. 82

Figure 4-26: X-ray Diffraction of V Doped NbO_2 83

Figure 4-27: Raman Spectra of V Doped NbO_2 Thin Films with Different V Contents 84

Figure 4-28: SEM micrographs of V doped NbO_2 for sample (a) S2 and (b) S4 85

Figure 4-29: Optical Transmittance of sample S2, S3 and NbO_2 deposited on Si substrate 87

Acronyms

Nb	Niobium
V	Vanadium
NbO_x	Niobium Oxides
NbO_2	Niobium di-Oxide
Nb_2O_5	Niobium penta-Oxide
VO_2	Vanadium di-Oxide
TiO_2	Titanium di-Oxide
BCC	Body-Centered Cubic
UV	Ultra Violet
RF	Radio Frequency
DC	Direct Current
PVD	Physical Vapor Deposition
PECVD	Plasma Enhanced Chemical Vapor Deposition
XPS	X-ray Photoelectron Spectroscopy
XRD	X-ray Diffraction
SEM	Secondary Electron Microscope
UPS	Ultra-Violet Photoelectron Spectroscopy
AES	Auger Electron Spectroscopy
EELS	Electron Energy Loss Spectroscopy
MOS	Metal-Oxide-Semiconductor
UV-VIS-NIR	Ultra Violet- Visible- Near Infrared Radiation
H	Hardness
E	Young’s Modulus

1. Introduction

1.1 Motivation

Transition metal oxides epitomise an attractive class of materials with exclusive optical and electronic properties. These diverse electronic, magnetic and optical properties of transition metal oxides find an extensive ground of significant technical applications including electronic (as semiconducting, insulating, superconducting etc.) and photoelectronic devices (e.g. Non-volatile memory, UV photodetectors, solar cell etc) [1–3]. Some transition metal oxides (e.g. VO_2, NbO_2, TiO_2 etc) show reversible phase transformation between metallic state to non-metallic state by applying temperature or electric field. Because of multiple valance electrons of these metallic elements, it is easy to transfer electrons back and forth. This transformation is basically accompanied by crystallographic or structural changes. Figure 1-1 displays some transition metal oxides which exhibit temperature-driven Metal Insulator Transition (MIT). Many potential electrical applications such as ultrafast electrical switches, memristive devices, and thermal sensors of transition metal oxides depend on their metal insulator transition temperature. Niobium Oxide and vanadium oxide are of the prominent transition metal oxides for optical and electrical applications. Vanadium Oxide has got significant research interest in the last few decades because of its appropriate optical and electrical properties. However, the applications of Vanadium di-Oxide (VO_2) as electrical switching become restricted because of low transition temperature of Vanadium di-Oxide (VO_2) at 68 °C. On contrary, Niobium dioxide, having similar optical and electrical properties, shows very high transition temperature that is beneficial for micro electric and circuit applications. Niobium di-Oxide (NbO_2) shows reversible transition from rutile at room temperature to distorted rutile structure at elevated temperature. Before comprehending the mechanism of the metal insulator transition of Niobium Oxide thin films, it is essential to distinguish the structural and chemical properties of Niobium Oxide thin films. Niobium Oxides show three stable oxidation states including Niobium Mono-Oxide (NbO), Niobium di-Oxide (NbO_2) and Niobium penta-Oxide (Nb_2O_5).

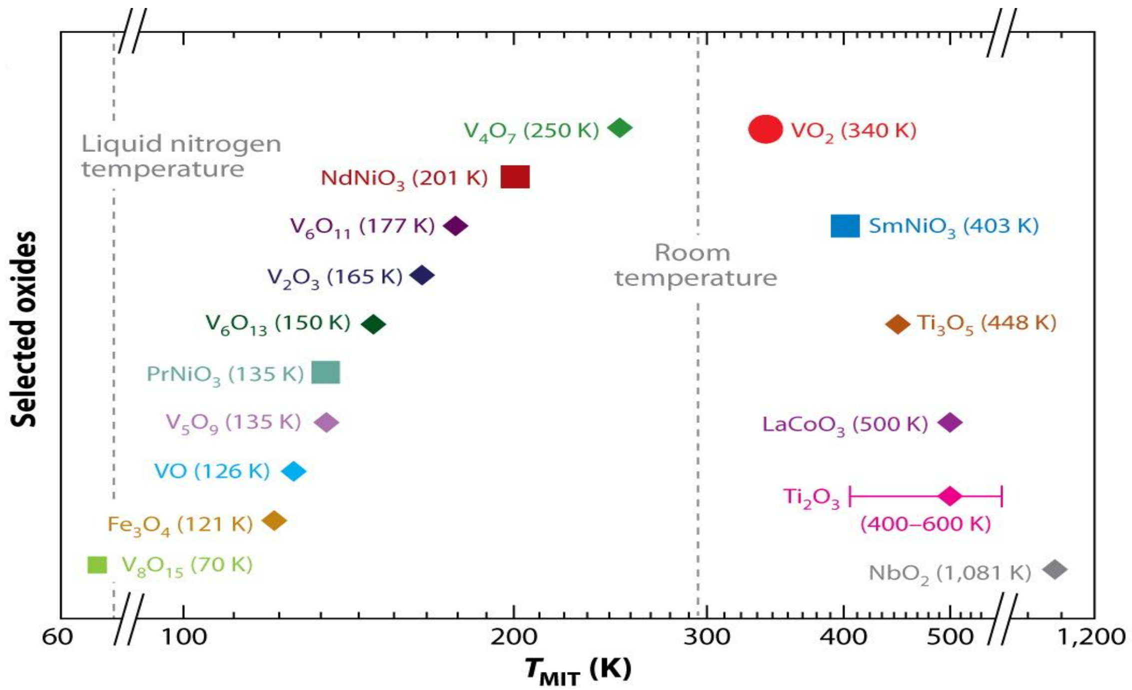

Figure 1-1:Metal Insulator Transition Temperature of Typical Transition Metal Oxides [4].

It is challenging to acquire specific structures of Niobium Oxide thin films due to the complex Niobium oxygen system. The structural change in many cases comprises trivial distortions of core structure which induces a radical deviation of physical properties. Each of the stable and metastable Niobium Oxide s has unique physical properties and corresponding applications. Therefore, precisely controlled synthesis of highly crystalline thin films is crucial for the understanding of their structural and physical properties. In very recent years, synthesizing high quality metal oxide thin films becomes possible due to the progressive development of thin film synthesis techniques. However, optimisation of deposition parameters is essential for acquiring a specific oxide structure. For single layered thin films, metastable phases may appear because of epitaxial stabilization. The use of magnetron sputtering deposition technique for growth of different Niobium Oxide s thin film is under development and some challenges remain to be overcome in order to achieve structural control, reproducibility and precise control of physical properties. Moreover, NbO_2 can be doped with a variety of transition metal oxides and thus doped NbO_2 can be prepared. To date, VO_2 is the most prominent transition metal oxide and convenient to be doped with NbO_2. Substitution of Niobium cation by vanadium cation can modify the basic structural and physical properties. To date, there is no detailed research about the substantial doping of Nb and V oxides. Therefore, further research on structural evolution of V doped NbO_2 is inevitable.

1.2 Objectives

The primary objective of this thesis is to understand the optical and electrical properties of Niobium Oxide thin films with different crystal structures prepared by magnetron sputtering. In order to achieve this key objective, a few sub objectives are to be followed:

1. Synthesis of phase pure amorphous, orthorhombic and tetragonal Niobium Oxide s on Si and SiO_2 substrates.
2. Preparation of V doped NbO_2 and Nb doped VO_2 crystalline thin films.
3. Understanding the chemical structures and morphologies of Niobium Oxide s and doped NbO_2 with different oxygen gas contents.
4. Investigation of the physical properties of the thin films to comprehend the connection between chemical structure and properties of the synthesized films.

1.3 Methodology

Magnetron sputtering was used to deposit Niobium Oxide s with a goal to obtain phase pure tetragonal Niobium di-Oxide (NbO_2) and Vanadium (V) doped Niobium di-Oxide (NbO_2) thin films on p-type Si (100) and Quartz (SiO_2) wafers. X-ray Diffraction (XRD) and Raman Spectroscopy were used to determine their respective phases and crystal structures. The oxidation states and stoichiometry of the thin films were characterized with X-ray Photoelectron Spectroscopy (XPS). Additionally, the morphology and thickness of the films were examined by Scanning Electron Microscopy (SEM) and Optical Profilometer. Spectrophotometer, 4-Point Probe and Nano-Indentation were used to evaluate the transmittance, electrical conductivity and mechanical hardness of the films, respectively.

1.4 Organization of Dissertation

In this dissertation, the structural, chemical, optical, electrical and mechanical properties are measured, analysed, presented and discussed.

In Chapter 1 the motivation, objectives, and methodology of the present research work are presented, and the organization of the dissertation is reported.

The basic features and a comprehensive review of Nb and its oxides are offered in Chapter 2. It also covers the basis of magnetron sputtering techniques followed by a short

description of different characterizations techniques. Additionally, this chapter covers the basics of I-V characteristics of NbO_2 thin films.

In Chapter 3 the deposition parameters and corresponding characterization techniques used in this research for different thin films are illustrated.

Chapter 4 consists of a few sections. In the first section I demonstrate the deposition characteristics of Niobium and its oxide films by magnetron sputtering system. In this section I present the detailed structural analyses of Niobium Oxide thin films preparation and the effect of different influential deposition parameters on them. In the second section I illustrate the corresponding physical properties of different Niobium Oxide thin films followed by their morphological properties. In the third section the structural variations of V doped NbO_2 and Nb doped VO_2 thin films with different doping concentrations will be reported.

In Chapter 5 the results presented in Chapter 4 are concluded, and the possible future works relevant to the thesis are proposed.

2. Literature Review

In this chapter a comprehensive review on Niobium Oxides, doped Niobium Oxides and a description of the deposition and characterization techniques are provided.

2.1 Niobium and Its Oxides

2.1.1 Niobium (Nb)

Niobium belongs to group V in the periodic table with electronic structure of Kr [$4d^4$ $5s^1$] (atomic number of 41). This soft and ductile transition metal was discovered in 1801 by Charles Hatchett. Niobium has a Body-Centered Cubic (BCC) lattice presented in Figure 2-1. It has a valence electron in 4d energy level that leads to multiple stable oxidation states. The highly reactive Niobium can form stable oxides, carbides [5], nitrides [6], borides [7] and silicide [8] which are hard metal alloys. Niobium is more subjected to oxidation as oxygen is easily dissolved in the open BCC lattice of Nb [9] and therefore, inevitable oxide layer is readily formed on the surface [10,11] of these foreign elements affects the mechanical and electrical properties [9].

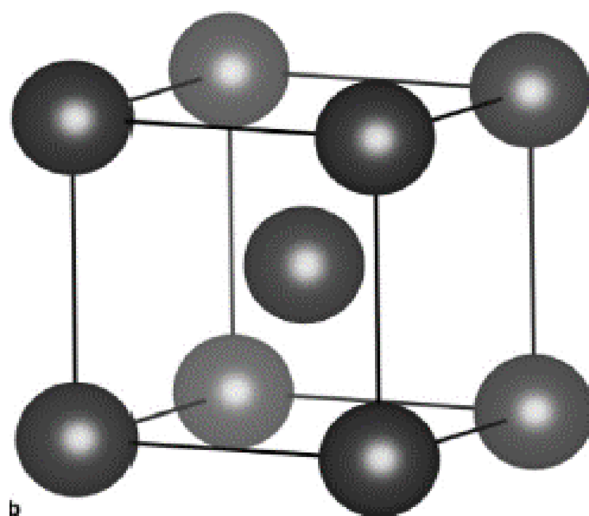

Figure 2-1: Cubic Structure of Metallic Niobium[12]

Niobium is found in nature as columbite or tantalite and the major source of these mineral is Brazil and Canada [11,12]. It is used as a toughening and strengthening alloying element in steel industry [15]. Niobium superalloys are generally used in aircraft industries, nuclear and space industries [16,17]. It has several applications in different industries as pure Niobium or as alloying element because of its admirable corrosion, heat and abrasion resistance behavior [11,18]. Other than these, Niobium has a few electronics applications as electrolytic capacitors, catalysis [13], battery alloys, photonics, Metal Insulator Metal (MIM) tunnel diodes, piezoelectric devices [19] and as surgical implants in medical science [16]. However, the poor oxidation resistance of Niobium at elevated temperatures sometimes limit its applications [20].

Table 2-1: Physical Properties of Niobium and Its Oxides

Properties	**Nb**	**NbO**	**NbO_2**	**Nb_2O_5**
Atomic Density (cm^{-3})of Nb	5.5×10^{22}	4×10^{22}	2.83×10^{22}	2×10^{22}
Atomic Density (cm^{-3}) of O	NA	4×10^{22}	5.67×10^{22}	5×10^{22}
Molar mass, g/mol	--	--	124.91	--
Crystal System	BCC	Cubic [21] [22]	Tetragonal (LT), Rutile (HT)	Several Polymorph
Lattice Parameters (Å)	3.3	4.2 [22]	a=13.7, c=5.9(LT) a=4.8, c=2.9 (HT) [23]	Not specific
Formation Enthalpy ΔH (25°C) ($kJmole^{-1}$)	NA	-408	-800	-1900
Density (gcm^{-3}) at Room Temperature	8.57	7.26 [24]	5.98	Amorphous=4.36 [25] Crystalline= 5.17 [26]
Melting Temperature (± 5°C)	2741 [23]	1940 [24]	1917 [27]	1465 [28]

Gibbs Energy ($Jmol^{-1}$)	--	375.50	741.38	1772.71
Molar Heat Capacity ($Jmol^{-1}K^{-1}$)	0.268	41.25	57.49	--
Electric Conductivity Configuration	Metallic	Metallic	Semiconductor (at LT), Metallic (at HT)	Dielectric
Thermal Conductivity ($Wm^{-1}K^{-1}$)	54.1	--	--	--
Color (Visual)	Gray	--	Blue / bluish black	Blue or Yellowish
Hardness (GPa)		NA	--	4 to 14

2.1.2 Niobium Oxidation

The Niobium-Oxygen system is a bit complex as Nb has different stable and metastable oxides and polymorph. Oxygen can be easily dissolved in the BCC lattice of Niobium, making a Niobium Oxide solid solution and thus, Nb forms different oxides in their suitable conditions. Solubility of oxygen in Niobium increases with temperature [29].

The formation of different Niobium Oxide and their chemical and physical behaviours are still contradictory [30], even though many researchers continued to investigate Niobium Oxide s following by the preliminary work by Brauer et. al. [30]. Before 1960's, many of the literatures were written in German and Russian languages, therefore those were not understandable for most international researchers.

Phase equilibrium diagram of Nb-O system was first proposed by Elliott [29] in 1960 that showed the narrow range of NbO and NbO_2 in the thermodynamic stability. However, some researchers found the inconsistency about the existence range of different Niobium Oxides [31–33]. And thus, there are many unanswered questions on Nb-O system.

The stable oxidation states of Nb-O system are NbO, NbO_2 and Nb_2O_5, whereas there are multiple metastable NbO_x ($0 < x < 1$ and $2.0 < x < 2.5$) in between the stable states.

Also, Nb_2O_5 has nine different polymorphs. Each of the Niobium Oxides has interesting properties and potential applications, and some of them are presented in Table 2-1. A hypothetical study by Ronay et al. [34] on primary formation of oxide layer on Niobium metal surface exhibited that potential barrier for oxygen incorporation on a Niobium surface intensely increased by creation of NbO [34,35].

The theories were supported providentially by the experimental results of Pantel et al. [36] . XPS, UPS, AES and EELS analyses verify that oxygen incorporation in Niobium metal surface became even more competent in H_2O atmosphere showed by Colera et. al.[37,38]. Therefore, an unavoidable NbO layer at the interference between metal Nb and Nb_2O_5 is always present, as proven by many literatures.

This characteristic can be useful for electronic applications like Superconductor–Insulator–Superconductor Tunnel Junction (SIS). Higher oxygen introduction on Niobium surface at elevated temperate may lead to formation of NbO_2 and even Nb_2O_5 for further exposure [9,39]. Under equilibrium condition the Nb-O system likes to form the most stable state of Nb_2O_5, if enough oxygen is present [40].

2.1.2.1 Niobium Monoxide (NbO)

In NbO, Niobium atoms are coordinated to four oxygen atoms in a square planar arrangement. NbO exhibits a characteristic metallic behaviour with a resistivity of about 21 μΩcm at room temperature [41]. In NbO the oxidation state of Nb is +2 and its electronic property are defined by the d-electrons of Nb.

During formation of NbO the original crystal structure of Nb metal breaks and new defective rock-salt structure forms. NbO shows highest number of point defects among all transition metal oxides.

The Nb atoms in the NbO structure form 3D network of octahedral, linking each other by apexes and each of them is coordinated to four O atoms, illustrated in Figure 2-2. In order to stabilize this structure, the strong metal-metal bonding and the metal-oxygen bonding are both important [42].

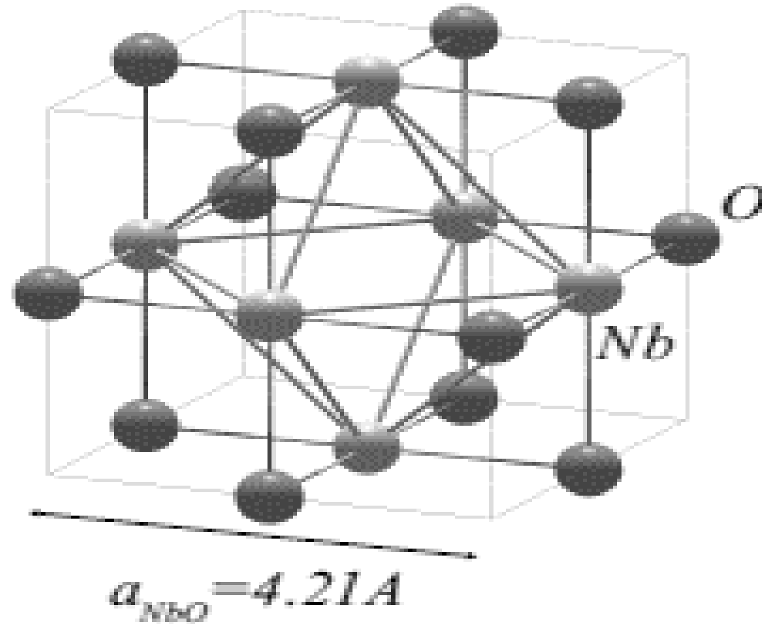

Figure 2-2: Crystal Structure of NbO [43]

The density of NbO is ~ 7.3 g/cm^3, its melting point T_m is 1940°C [24], and its stoichiometry range is very narrow (within very short range this oxide can be formed) [44]. Unlike other transition metal mono oxides (e.g. VO, TiO etc.), NbO does not exist in a large extension of single-phase field. Therefore, a small deviation of its composition leads to stoichiometric variation and mixed phases are produced. At suitable conditions suboxides are formed by oxidisation of Niobium. NbO_x, NbO_y, NbO_z phases can be detected with stoichiometries between Nb and NbO [9,45]. NbO shows metallic behaviour at higher temperature, even at room temperature the electrical resistivity is approximately 21 μΩ·cm [41]. Unlike other stable oxides NbO does not have any major technological applications. However, NbO can be used in electrolytic capacitors replacing metallic Nb as the anode material [46,47].

2.1.2.2 Niobium Di-Oxide (NbO_2)

Oxidation state of NbO_2 is +4 and it offers a stoichiometry between NbO and Nb_2O_5. The structure of NbO_2 is distorted rutile with a space group I41/a at Low Temperature(LT) [48] and tetragonal with a space group of P42/mnm at High Temperature (HT) [49]. The HT tetragonal structure is considered as chains of edge-sharing (along C-axis) NbO_6 octahedrons having 2 formula unit with side lengths a = b=4:85Å and c = 3:03Å [49].

The LT phase is basically the distorted version of High Temperature (HT) phase and the unit cell in the LT phase contains 32 formula units of NbO_2 where the Nb-O bond lengths are in between 1.91 and 2.25Å [50,51]. A reversible second order phase transition from distorted rutile structure to regular rutile structure occurs at ~ 800-810[51,52], shown in Figure *2-3*. NbO_2 can be formed by controlled oxidation of Nb or reduction of Nb_2O_5. Some properties of NbO_2 are summarized in Table 2-1. The tetragonal phase of NbO_2 is considered as n-type semiconductor which has a band gap between 0.5eV to 1.2eV [53] and the electrical resistivity is in the order of 10^4 Ω cm [23,54,55].

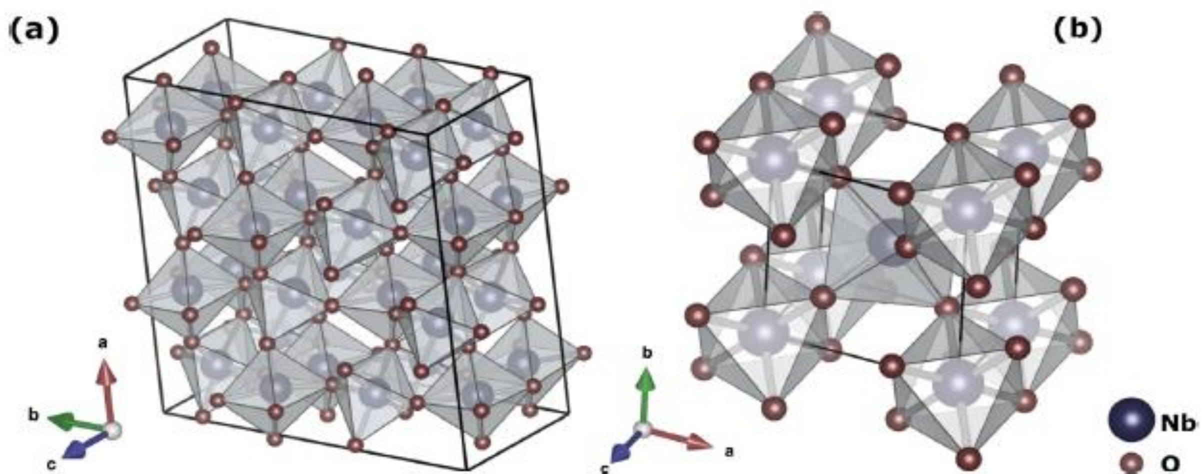

Figure 2-3:Structure of (a) Tetragonal and (b) Rutile NbO_2 [12]

The electrical conduction mechanism in tetragonal NbO_2 was demonstrated using the Efros–Shklovskii variable range hopping model [56] or the Peierls model [57]. NbO_2 has practical applications in diverse areas such as impedimetric immune sensors based on Niobium/Niobium Oxide electrodes [58], electro catalysts [59], MOS devices [60], memristive device [61,62], exchange membrane fuel cells [4]. NbO_2 deviates slightly from stoichiometry at elevated temperatures (at or above 1100°C)[31] and these deviation can significantly influence the electrical property.

The experimental studies on NbO_2 were standstill for few decades. With the advancement of thin film synthesizing techniques, many researchers show interest on synthesizing NbO_2 for optical and electrical applications.

Deposition of crystalline NbO_2 thin films was explored by different deposition techniques, including chemical vapor transport method [63], reactive sputtering [64,65],

molecular beam epitaxy [66], thermally oxidization of Nb [60]. Researchers have also explored the synthesis and applications with different substrates, including (La,Sr)$_2$(Al,Ta)$_2$O$_6$ (LSAT) (111) and $SrTiO_3$ (STO) (111) [66], Al_2O_3 (0001), MgO (111), $MgAl_2O_4$ (111) [65]. Epitaxial films are suitable for many applications because of their high crystal quality and the opportunity of employing anisotropic physical properties due to the single crystalline structure. Since NbO_2 has a narrow stoichiometric range, it is challenging to synthesize crystalline NbO_2 with high purity. The electrical properties of such thin films are highly dependent on the oxygen contents in the thin films and the robust conductivity transformation happens along the dimerization direction (rutile c-axis) [67].

NbO_2 can be a good alternative to VO_2, a closely related binary oxide, because of its high transition temperature and wide bandgap energy [66]. Distorted rutile (tetragonal) to rutile phase transition of NbO_2 can be either triggered by applied voltage, or high temperature, or light irradiation. For thin films, MIT is usually induced by electrical field as very high fields are easily achievable. NbO_2 can be practically used as an electrical switching device [68]. I-V (current-voltage) characteristics of NbO_2 is non-linear and it displays an abrupt jump in the conductivity while applying threshold voltage (switching behavior). However, to date, there is no definite mechanism of the switching behaviors of NbO_2 is established. Metal to Insulator Transition can also be triggered by applying high temperature. At 808 ^oC NbO_2 shows a true rutile structure with lattice constants of a=b=4.8 Å, c=2.9 Å [66]. This higher transition temperature extends the possible range of potential applications.

2.1.2.3 Niobium Penta-Oxide (Nb_2O_5)

With +5 oxidation state Nb_2O_5 is the thermodynamically stable state of the Niobium–oxygen form. This n-type semiconductor has very low electrical conductivity as 4d electrons are bonded to the O 2p electrons [69]. Nb_2O_5 is relatively abundant in nature and exists in several polymorphic forms including amorphous and several different crystalline forms with complex structure [70,71]. The existence of different crystalline polymorph strongly depends on the preparation methods and annealing conditions that can have dissimilar properties [72]. Studies on polymorph of Nb_2O_5 was first initiated in 1940s which gave rise to an encouraging series of structural phases [26].

Later on many phases of Nb_2O_5, including B- Nb_2O_5 (C_{2h}^6, monoclinic), H- Nb_2O_5 (C_{2h}^1, monoclinic), L- Nb_2O_5, M- Nb_2O_5 (D_{4h}^{17}, tetragonal), N- Nb_2O_5 (C_{2h}^3 ,monoclinic), P- Nb_2O_5 (D_4^{10}, tetragonal), R- Nb_2O_5 (C_{2h}^3, monoclinic), T- Nb_2O_5, TT- Nb_2O_5 (pseudo hexagonal or monoclinic), Z (C_2^1, monoclinic), are reported in various literatures since 1966, initiated by Schäfer et al. [40].

The phases are commonly based on volumic arrangement of NbO_6 coordinated octahedral with different configurations. Niobium positions are usually about 3.9Å apart which permits to change in stoichiometry for accommodation [9,73]. At the certain temperature, in between 500°C to 800°C , orthorhombic T- Nb_2O_5 phase appears where Niobium atoms are mostly surrounded by seven or six oxygen atoms that forms pentagonal bipyramids or distorted octahedrons respectively [71]. Other Niobium atoms can be coordinated to nine oxygen atoms in interstitial sites. Many polymorphs show entirely dissimilar structures than T- Nb_2O_5.

At high temperature, above 1100°C, atoms are highly moveable that allow structural rearrangement to form H- Nb_2O_5 phase [40,74]. The structure of H-Nb_2O_5 phase comprises 3×4 and 3×5 ReO_3-type blocks of corner-shared NbO_6 octahedron with the space group of P2 (no. 3) and is categorised as a monoclinic unit cell containing 14 formula units [75]. HT monoclinic phase H- Nb_2O_5 is the thermodynamically stable and most studied oxide [76] in Niobium pentoxide polymorph. It can be obtained easily by heating Nb or its oxides at higher temperature in air or oxygen atmosphere.

Harald-schäfer et al [40] describes the mode of formation, structures, and thermal properties of different Nb_2O_5 polymorph. Recently Valencia-Balvín et al. [77] have explored the phase stability of numerous phases of Nb_2O_5 under pressures up to 100 Kbar, in which the first-principle density functional theory was used to calculate the isothermal bulk moduli and equilibrium crystal structures.

The oxidation of metallic Niobium or Niobium Oxide s in air is the most common method to form different Nb_2O_5 polymorph. Other prevalent techniques include hydrolyzing of alkali niobates or Niobium alkoxides [78], sol–gel [79], pulsed laser deposition [80], reactive RF magnetron sputtering [81], atomic layer deposition [82].

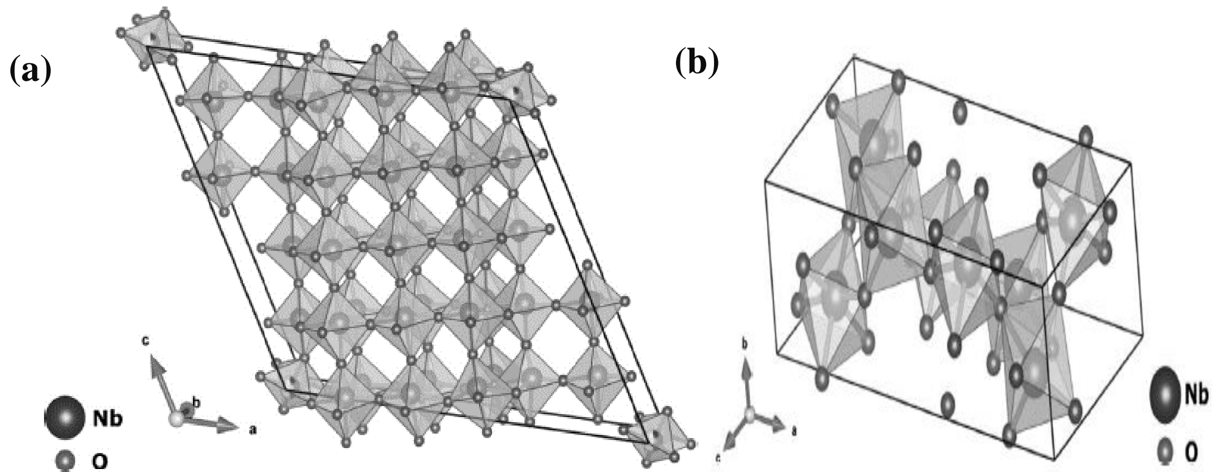

Figure 2-4: Monoclinic Structure of (a) H- Nb_2O_5 (b) B- Nb_2O_5 [12]

Nb_2O_5 is a semiconductor (insulator like) with a wide band gap [69]. It has high refractive index [83], good corrosion resistance [84], high dielectric permittivity [85], and good chemical and thermal stability [13]. Being the most stable oxidation state of the Niobium–oxygen system Nb_2O_5 has a wide range of technical applications including optical (intelligent windows, solar cells etc.) and microelectronic devices, biomedical implants, catalysis [86], sensors, capacitors, non-volatile memories based on resistive switching (memristors) [87].

Currently an extensive research is being conducted on memristors (memory resistors) which are essentially a fourth class of electrical circuit (connecting resistor, capacitor and inductor) that exhibit exceptional properties mostly at nanoscale. Nb_2O_5 is one of the promising candidates for this application [88]. It can also be used as oxygen sensors as its resistivity changes with the oxygen dissolved in it [89]. A recent paper by Rani et al. reviews the synthesis methods, the structures (including nanorods, nanobelts, nanospheres etc.), the essential properties, and the applications of Nb_2O_5 and explicates the forthcoming research guidelines on Nb_2O_5 [70] .

2.1.2.4 Metastable Niobium Oxides

A few papers on metastable Niobium Oxide s were published in early 1980s and 1990s [90–92]. However, there are no significant research reported for metastable Niobium Oxide s for long time after 1990’s.

As mentioned earlier oxygen can be easily dissolved into the BCC lattice of Niobium within its solubility limit. Solubility limit usually increases with the rise of temperature and supersaturation is possible under special conditions. Supersaturation may lead to form suboxide phases [93]. Three suboxides, namely NbO_x, NbO_y, and NbO_z, have been found so far [22, 37]. They are metastable [9] and have metallic characters as their superlattice structures are correlated to the original Niobium metal [27]. Their formation temperatures and the chemical formulas are presented in Table 2-2.

Table 2-2: Formation of Metastable NbO_x (0< x <1)

	NbO_x	**NbO_y**	**NbO_z**
Formation Temperature	270-500 °C	330-500 °C	400-700 °C
Formula	Nb_6O	Nb_4O	Unknown
O_2 gas content	2.6 to 3.6 wt %	----	---

Hibst et al. [94] and McNeil et al. [95] detected fifteen metastable Nb_2O_5 modifications by exploring the oxidation of NbO_x (value of x in between 2.4 to 2.5) where many polymorph were related to ReO_3 structure containing of 4 × 4 blocks of corner-shared NbO_6 octahedrons. There are some other Niobium suboxides, (e.g. Nb_2O, Nb_2O_3, etc), reported in open literatures[91,93]. Nb_2O with lattice parameters a = 3.38Å and c = 3.27 Å were studied by Norman in 1960's [91]. Nb_2O can also be annotated as Nb_6O or Nb_5O by measuring the weight of the oxygen contents in the substance [43]. However, the reported preparation conditions were contradictory, and the conclusions were lack of evidences and unjustified. Nevertheless, the formation of Nb_2O sub oxide was further confirmed by X-ray photoemission spectroscopy [96] where the chemical shift of the binding energy due to of the formation of NbO_2 was reported to be as 1 ±0.2ev.

Heat treatment of metallic Niobium in oxygen atmosphere or heat treatment of Niobium Oxide s in vacuum can lead to form different kinds of Niobium sub oxides, which is highly dependent on the atmosphere and treating conditions, including temperature, heating rate, and the duration of heating. Terao et al. [25] showed the transformation of NbO_x phase to Nb_2O_5 by heating the samples in air but when Nb_2O_5 was heated in a vacuum chamber, NbO_z appeared first and then NbO formed successively [25].

Further research on these metastable Niobium Oxide s are essential in order to understand their structures and their preparation conditions, which will be very useful for their applications.

2.1.3 Doping Niobium Oxides

NbO_2 can be mixed with a variety of transition metal oxides. Substitution of Niobium cation can modify the structure and thus the physical properties including optical and electrical transport properties [97]. Particular doping gas content may enhance the properties of the thin films [98] and can change the MIT of NbO_2 [99]. Being the oxides of the same group transition metals, NbO_2 and VO_2 have lots of similarities in their lattice structures and chemical and physical properties. Both NbO_2 and VO_2 undergo a phase transition at certain temperatures that changes their transport properties. Moreover, VO_2 has more desirable transition properties for optical electrical applications: single crystal VO_2 shows much larger jump in electrical conductivity (10^5 times) comparing with single crystal NbO_2 (10^1 times) at MIT. Vanadium is therefore of particular interest as a doping element for NbO_2. Substitution of Nb by V can dissociate the Nb-Nb bonding that lowers the phase transition temperature of NbO_2 [99]. This kind of solid solutions between NbO_2 and VO_2 is possible owing to their similarity in both chemical characteristics and atomic radii [97]**.** However, few researches have been done on doping with a wide range of gas contents.

One of the drawbacks of NbO_2 is its very high transition temperature (808 °C). On the contrary, the low transition temperature (67 °C) of VO_2 limits its applications in micro-electric devices. It is suggested by Rao et al. in 1975 that the incorporation of certain gas content of Nb or Mo into VO_2 thin films may increase the MIT of VO_2 [100]. Therefore, study of V doped NbO_2 and Nb doped VO_2 may create a new material to solve the drawbacks of NbO_2 or VO_2 for optical and electrical applications. That encourages to do further research on these two most potential transition metals di oxides.

NbO_2 can mix with a variety of transition metal oxides. Substitution of Niobium cation by vanadium cation can modify the basic structural properties. when V is merged into NbO_2 there is a possibility of happening following reaction that is estimated for bulk polycrystalline samples [101,102].

$$Nb^{4+} + V^{4+} = Nb^{5+} + V^{3+} \quad (2\text{-}1)$$

Sizes of Nb^{5+} and V^{3+} ions are similar that leads to smaller local lattice distortion, therefore, it is convenient to form Nb^{5+} and V^{3+} if we contemplate the size effects only [101]. Moreover, 4d electron of Nb is more unbalanced comparing with 3d electron of V. However, other forms can also be formed as a solid solution or compound form. There is no in details research about the mixture of Nb and V oxides. Therefore, further research on structural evolution of V doped NbO_2 is inevitable.

2.2 Deposition Techniques

There are several deposition techniques for transition metal oxide (e.g. NbO_x, VO_x, etc) thin film preparation. Each technique has its own unique principle. Principles for the common techniques are described shortly in this section.

Sol-Gel Deposition: this process is based on chemical reactions where films are produced from a colloidal solution ("sol") with an aqueous or nonaqueous solvent. In this process, Gel is formed by partial evaporation of the solvent or addition of an initiator that polymerises the particles in the sol. To get the final solid product gel can be heated at high temperature. Sol is deposited on a substrate by spinning, dipping or transferring to a mould and It takes time for sedimentation. Even though there are several steps for forming the desired thin films this method is very straightforward.

Electro Deposition: This technique is based on the reversed galvanic cell.

Cathodic Arc Evaporation: in this process, high current melts the small spots of the target surface (cathodic spots) and the film forms from the evaporated atoms. Such deposited films exhibit high density and good adhesion. However, macro particles or droplets can be found in the films because of the micro explosion at the cathodic spots.

Physical Vapor Deposition (PVD): in this process, thin film forms from the vaporization of solid/liquid surfaces by ion bombardment (sputtering) or by laser ablation or by electron beam evaporation or by thermal evaporation. Sputtering is highly relied on plasmas I which ions are formed in the plasma and accelerated, and then bombard the metallic target, and the atoms in the targets are sputtered off from the target surface.

Chemical Vapor Deposition (CVD): in this process, thin films form from a vapor through a chemical reaction in a mixture of gaseous precursors. The exceptional throwing power of this method allows the films of uniform thickness and low porosity on substrates of complicated shapes.

Atomic Layer Deposition (**ALD**): the concept of this this process is similar to that of CVD but the deposition process is based on layer-by-layer. Layers forms during the reaction cycle through alternating gaseous species (precursors). Unlike CVD in which precursors are not typically present in the reactor, the precursors in ALD are injected as a sequence of consecutive non-overlapping pulses and these precursors react with the depositing surface to form films.

Thermal Evaporation: This is a PVD technique where the material to be deposited is heated to its sublime point to make it evaporate and then deposit onto the substrate.

2.2.1 Fundamentals of Sputtering Deposition

Among the numerous deposition techniques plasma enhanced chemical vapor deposition (PECVD) and physical vapor deposition (PVD) techniques are the most common used ones in industry.

Sputtering (DC or RF) is a widely used flexible PVD technique for thin film deposition because of its high process control and higher homogeneity on large area deposition [103]. By using this technique, both conductive and non-conductive metals, metal alloys, and even dielectrics can be easily deposited by choosing appropriate target and power source. Because of a collisional cascade initiated at the target surface by incident energetic projectile ion's impacting, the atoms are discharged from the target (metal or metal alloy) surface. In certain ion energy range, higher impacting ion energy creates higher volume of dislocated and sputtered atoms. Ions can be produced and accelerated using an ion source (e.g. Ion Beam Sputtering - IBS) or directly from a plasma (e.g. magnetron sputtering - MS). Ion beam sputtering is not suitable for large scale industrial applications as external source of ions are used (e.g. Dual Ion Beam Sputtering - DIBS) [104]. A high negative voltage is applied to the target when ions are directly from plasma, in which positive ions gain enough energy in the electrical field toward to the target. And sputtering is initiated by the bombardment of ions onto the target. Target works as the driving cathode and the substrate holder faces to the target, while the surrounding walls of the vacuum chamber act as the anode. In this process, the vacuum chamber is pumped

down to a base pressure in the order of x10^{-4} Pa or lower by a combination of turbo and rotary mechanical pumps. Reactive (e.g. O_2, N_2) gases and inert gas (usually Ar) are introduced into the chamber that rise the pressure inside the chamber.

Deposition pressure can be controlled by a throttle valve and usually the deposition pressure is in between 0.5 Pa to 10 Pa. Magnetrons can be powered by a variety of power sources including radio frequency (rf), direct current (dc), pulsed dc, and high-power impulse (HIPI) sources. RF source is suitable for non-conducting targets while DC source is suitable for conducting targets. Arcing often occurs during reactive sputtering due to a low voltage and high current discharge as a result of target poisoning. Arcing can damage the target by local melting and may eventually destroy the power supply. In this case, film quality is lowered due to the presence of particulates and pinholes. Arcing can be avoided by applying pulse voltage (Pulsed DC) where discharge voltage is in between a high negative voltage and a low positive voltage and the frequency is lower than the rf power.

High Power Impulse Magnetron Sputtering (HIPIMS) that uses a huge energetic impulse to the cathode over a very short time period (~ 100 μs) can produce thin films with high quality and compatible adhesion [105–107]. In this thesis project, a direct current (DC) power supply is used. The schematic of the magnetron sputtering system is depicted in Figure 2-5. It shows the principle of magnetron sputtering using planar magnetron. In the planer magnetron, secondary electrons are stuck in the magnetic field which enhance the possibility of ionization of argon atoms and can be analyzed by Lorentz force:

$$F = \mathrm{e}(V \times B) \tag{2-2}$$

where B, V and e represents magnetic field, velocity of the electron, and e electron charge, respectively. Unbalanced magnetron is used to overcome the stress and defects of coatings by strengthening the magnet poles and allowing the electrons to be escaped.

When the power is applied to the target, a glow discharge is ignited between the cathode and the anode. Reactive gas ions are accelerated towards the cathode (metallic target) and bombard the target that initiates the sputtering.

Glow discharge is maintained by the Secondary electrons emitted from the target. Sputtered particles move towards the substrate and react with the working gas to form the desired films.

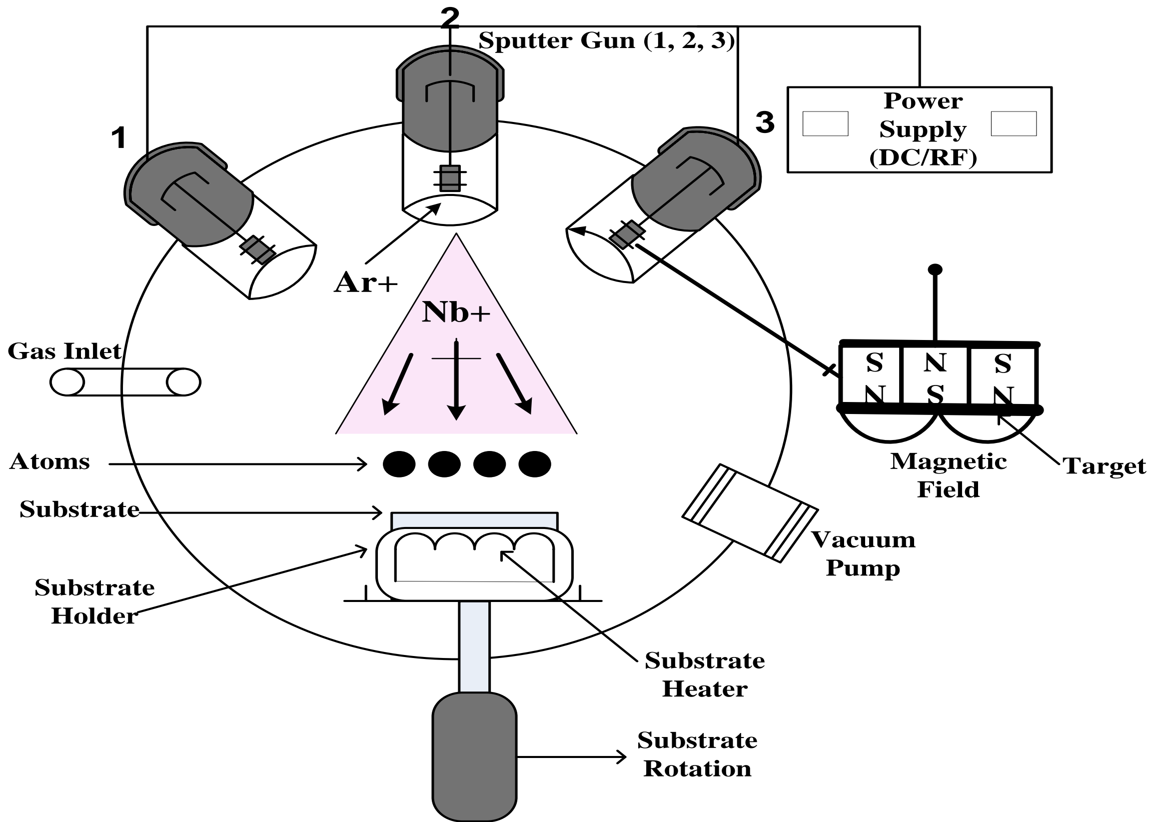

Figure 2-5: Schematic of Magnetron Sputtering

Most of the reactions happen on the exposed surface to form a compound. Compounds may also form on the cathode surface due to the enormous ion bombardment. This compound formation degrades the sputtering rate and the quality of the coatings. Target is denoted as poisoned if the compound layer formation rate exceeds the sputtering rate.

A schematic of glow discharge and the electric circuit of the deposition system is presented in Figure 2-6, where V_c indicates the high voltage applied to the target (cathode). In the glow discharge, ions, electrons, neutrals, and excited neutrals are shown. How the Ar atoms intrude the metal targets and initiates the deposition are explained in that figure.

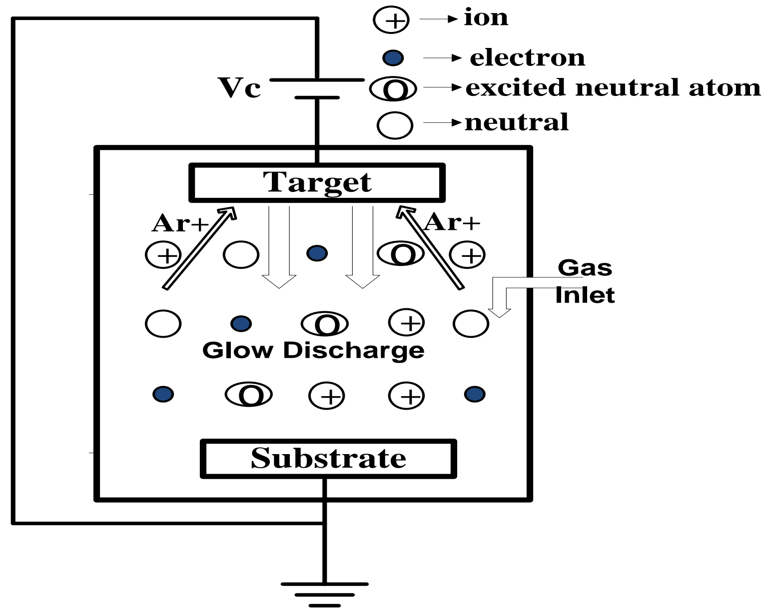

Figure 2-6: Glow discharge and electric circuit

The energy distribution of the sputtered atoms can be calculated by Thompson formula:

$$\mathrm{F} = \frac{E_\mathrm{b}}{(\varepsilon + E_\mathrm{b})^3} \tag{2-3}$$

where E_b is the binding energy of target atoms and ε is the sputtered atom energy.

Efficiency of sputtering can be identified by sputtering yield, Y that depends on the elemental composition of the target: mass, density, and lattice and surface binding energy. Y is basically a ratio of the number of ejected atoms to the number of incident projectiles. If the target surface is covered by non-metallic compounds: oxides or nitrides, Y reaches expressively low values.

Y can be explained by the following formula, given by Sigmund [108]

$$Y = \frac{3}{4\pi^2}\alpha\frac{4m_1m_2}{(m_1+m_2)^2}\frac{E_\mathrm{p}}{U_\mathrm{s}} \tag{2-4}$$

where m_1 is mass of the projectile (in amu), and m_2 is the mass of the target atom (in amu), α is constant, E_p is the energy of the projectile, U_s is the surface binding energy of the target.

The sputtering yield for different metallic target is explained by Depla et al. [109]. To sputter an atom from the target, momentum allocation from the ion-induced collision must overcome the surface barrier. Other phenomena such as surface structure modification and target heating may affect the sputtering. Overheating of the target can damage the target and therefore, the sputtered target should be effectively cooled. Sputtered particles leaving the target may have collisions with the gas atoms/molecules in the chamber before arriving to the substrate depending on the operation pressure. These collisions may change the particle energy, path, and momentum, and therefore morphology and microstructure of the growing films changes. Film microstructure and morphology can be explained by "Structure Zone Models" (SZMs) which is widely used to categorize the morphology of PVD deposited thin films.

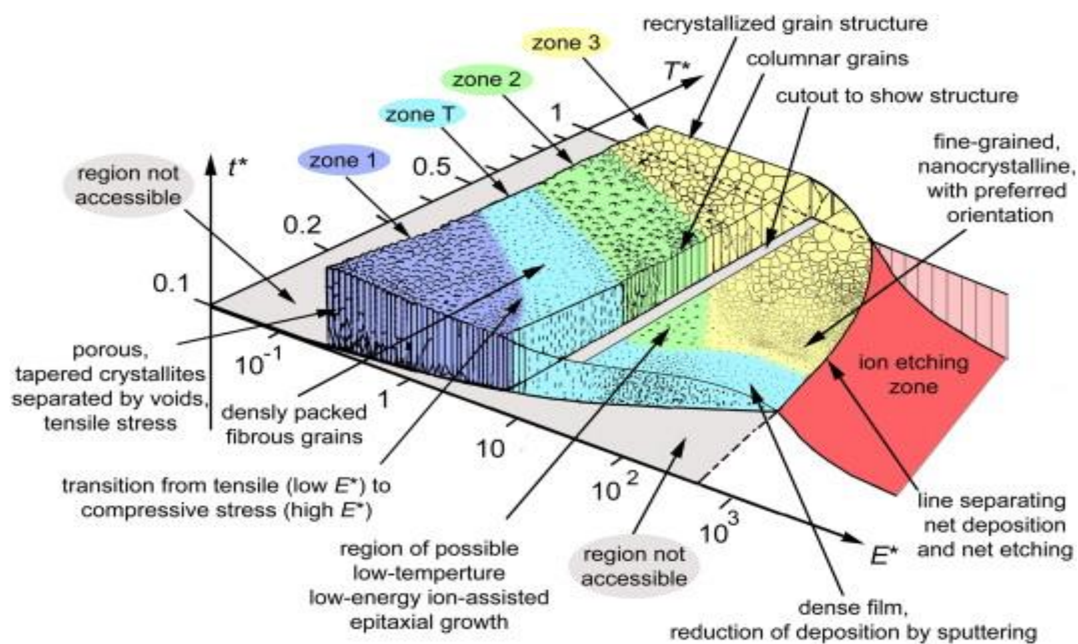

Figure 2-7: Structure Zone Model for Energetic Deposition Proposed by Anders[110]

The Structure Zone Model have been illustrated in Figure 2-7. Where, *E represents the normalized energy flux, *t represents net thickness and *T represents generalized temperature. The values on the axes are approximate and the actual values of the numbers depend on the specific material and other deposition conditions. This proposed model explains the uncertainty of film growth at very low *T and high *E, that is indicated as "region not accessible" in Figure 2-7. Another "not accessible region" is found at very low * E. Similarly, the proposed zones (zone 1, zone T, zone 2 and zone 3) are explained for the specific *E, *T and *t values.

Most of the surface morphologies of sputtered thin films can be explained by these zone models.

PVD deposition technique has advantages over other techniques, like higher kinetic energy of the vaporized species which can result in higher packing density of the deposited films at a relatively low temperature. It is appropriate for temperature sensitive films as the substrate temperature does not increase much during depositions. High deposition rate can be achieved by this technique for adjusting deposition parameters. Nevertheless, deposition rate decreases at deposition pressure increases because of the random collisions and the scattering of gases [103]. Moreover, the complicated equipment (vacuum chamber, pumps etc) and sophisticated power supplies make the technique expensive.

2.3 Structural Characterization

2.3.1 Raman Spectroscopy

Raman spectroscopy is an influential instrument for characterizing molecular structures. This vital non-destructive characterization technique is based on the inelastic scattering of light by the considered sample [111]. In this technique the sample is irradiated by a laser with monochromatic radiation and the studied sample absorbs photon from the source. While releasing the photons, frequencies are shifted up or down compared to the original frequencies [111]. This shift of frequencies provides the structural information of the sample. The resultant Raman spectrum is basically the plot of intensity of the dispersed light VS shift of frequencies (wavelength^{-1}).

The basic Raman scattering processes is demonstrated in Figure 2-8. Figure 2-8 shows how the photon induces a transition from ground vibrational state to a virtual state for one vibration [112].

The virtual states are not the real states of molecule and it is defined by the energy of the incoming laser. Prior to interaction with the light usually most molecules are likely to be in the ground vibrational state (marked m).

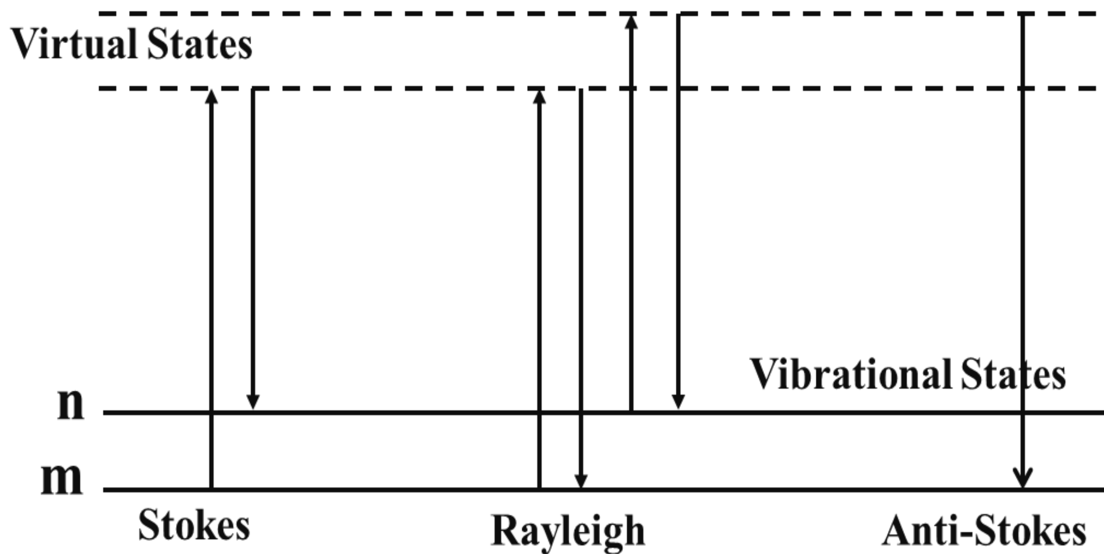

Figure 2-8: Rayleigh and Raman Scattering Process [112]

An elastic scattering process (e.g. Rayleigh scattering) occurs when light quantum $h\nu_0$ hits the molecule. Raman lines are denoted as Stokes lines and anti-Stokes lines determined by the initial and final vibrational states. Stokes lines are produced by quanta of lower energy and their intensities are higher than anti-Stokes lines [113]. Upward arrows in the Figure 2-8 indicate the low energy whereas downward arrows indicate scattered energy, however, both of them have considerable larger energies than energy of vibration. Raman spectrum is basically a fingerprint of the sample. It provides the information of interatomic and intermolecular bonding, the mechanical strain prevailing in a solid, the composition of multicomponent substance and the crystallinity degree of a solid [111]. To date, studies on Raman spectra of NbO_x thin films have been limited.

The Raman shifts below 100 cm^{-1} are vibrational modes of the crystalline lattice and the 100–200 cm^{-1} regions are contributions from selected molecular vibrations [114]. Active mode of Raman spectrum for the Niobium Oxide s are usually in between 100 cm^{-1} to 1000 cm^{-1} and each of Niobium Oxide s have their identical Raman shifts.

For the NbO_2 thin films 12 active modes Raman spectrum were reported in the 139, 170, 247, 333, 343, 405, 436, 463, 580, 631, 699 and 815 cm^{-1} positions by Zhao et al [60] in 2004 for the first time. Following their work four more researchers confirms the Raman spectrum of crystalline NbO_2 thin films prepared by different methods [55,62, 63, 109].

Raman spectrum of different crystalline Nb_2O_5 polymorphs [69,116,117] and amorphous [118] phases were reported by different researchers as well. Graça,et al. [116] described Raman shifts for different crystalline Nb_2O_5 polymorph in details. The main vibration mode at ~690 cm^{-1} is assigned for low distorted NbO_6 octahedral and other modes at ~220 cm^{-1} and ~310 cm^{-1} are assigned for the T-Nb_2O_5 phase [116]. For monoclinic H-Nb_2O_5 structure the active mode is at ~990 cm^{-1}. Therefore, Raman spectroscopy is widely used to identify the specific structures of the Niobium Oxide thin films. However,_Raman spectra of other Niobium suboxides have not been reported yet.

2.3.2 X-ray Diffraction (XRD)

X-ray Diffraction (XRD) is one of the most popular technique for characterizing crystal structures. This non-destructive technique is basically the scattering of a coherent wave by the atoms in a crystal. It reveals several information of the crystal including crystal structure and size, crystal orientation(texture), residual stress, lattice structure, phase identifications etc. X-ray source in the XRD tool can be generated by bombarding specific metal target e.g. Cu, Co or Fe with high energy electrons. When a monochromatic X-Ray source with wavelength λ and on the order of lattice spacing d, hits the sample at an angle θ, the incident X-ray is dispersed by the oscillating electrons surrounded the atoms. These dispersed X-Rays from each set of regular lattice planes forms a constructive interference and thus produce X-Ray Diffraction peaks. Constructive interference occurs if the wavelength of the X-ray and the lattice spacing follows the Bragg's law:

$$2\,d\sin\theta = n\lambda \tag{2-5}$$

where n is certain integer.

Figure 2-9 explains the bragg's law.

Peak position of the XRD is determined by the size and shape of unit cell. Whereas Peak intensities are determined by the atomic number and position of various atoms within the unit cell.

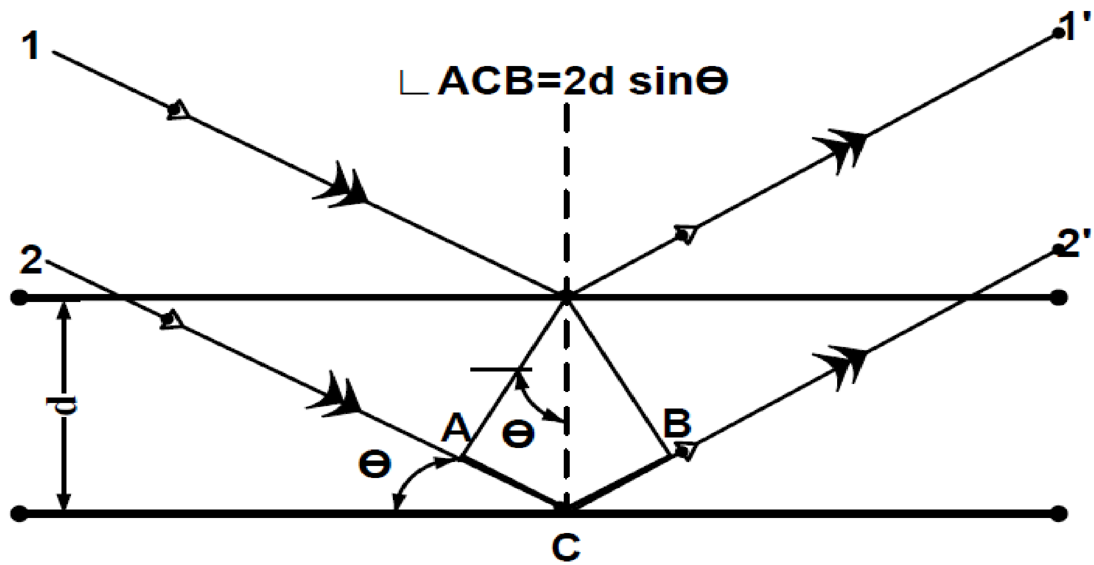

Figure 2-9: Principle of Bragg's Law [119].

Besides the characteristic phase study, the XRD measurement can also be used to calculate Grain size, *D* in polycrystalline samples by using the Scherrer's formula [120] :

$$D = \frac{K\lambda}{\beta \cos\theta} \quad (2\text{-}6)$$

where λ is the X-Ray wavelength, β is the full width at half maximum of the Bragg peak, θ is the Bragg angle, *K* is a dimensionless shape factor (=0.89).

The usual X-Ray Diffraction results of the bulk materials are very accurate and specific as the X-ray can penetrate deeply into the sample. However, the deep penetration is not suitable for the thin film samples as it acquires more data from the substrates other than the films. Therefore, Grazing Incident X-Ray Diffraction (GIXRD) is more suitable for thin film samples as GIXRD can avoid the strong scattering from the substrate.

In this case the penetration depth can be adjusted by changing the incident angle, θ. Depth profile of the thin films and the stress distribution can be detected by using GIXRD. Both XRD and GIXRD can be used for characterizing thin films depending on the film thickness. In this dissertation, this technique will be used to identify different phases of Niobium Oxide thin films. From the XRD data crystalline size will also be determined.

2.3.3 X-Ray Photoelectron Spectroscopy (XPS)

The X-Ray Photoelectron Spectroscopy (XPS) is another important non-destructive characterization tool which illustrates the elemental composition, empirical formula, chemical and electronic state of the elements inside the sample materials. In the XPS measurement X-ray beam irradiate the surface of the material and the core electrons inside the atoms are ejected by a photon. Remaining kinetic energy inside the emitted electron is the function of electron binding energy. Both the kinetic energy and the number of electrons can be analyzed by the combination of the electron energy analyzer and electron detector. The XPS spectrum is constructed by binding energy ($E_{binding}$) as it is not dependent on X ray energy.

The energy relation can be explained by Einstein formula:

$$E_{kinetic} = E_{photon} - \Phi_{XPS} - E_{binding} \quad (2\text{-}7)$$

where Φ_{XPS} is the work function of the instrument, E corresponds to different energies.

The basic phenomenon is described in Figure 2-10. The spectrum is obtained by plotting photoelectron intensity versus the binding energy. XPS is surface sensitive technique that can only detect the emitted electrons within 1 ~ 10 nm of the surface [121]. There is no photoelectron intensity loss as the penetration depth of X-rays is in the order of a few microns.

XPS measurements are conducted in Ultra High Vacuum environment to avoid collusion among the ejected photoelectron and gas particles that could be detrimental for losing few kinetic energies. To get the data inside the material sputtering (usually by Ar^+) is implied which removes the surface atomic layers in well controlled manner and helps to get the depth-profiling XPS spectrum.

XPS is widely used for analyzing Transition Metal Oxide (TMO) thin films [122]. One of the vital problems in calculating the XPS spectra of transition metal is dealing with the background signal. Commonly used subtraction routines for removing backgrounds are linear routine, Shirley routine and Tougaard routine.

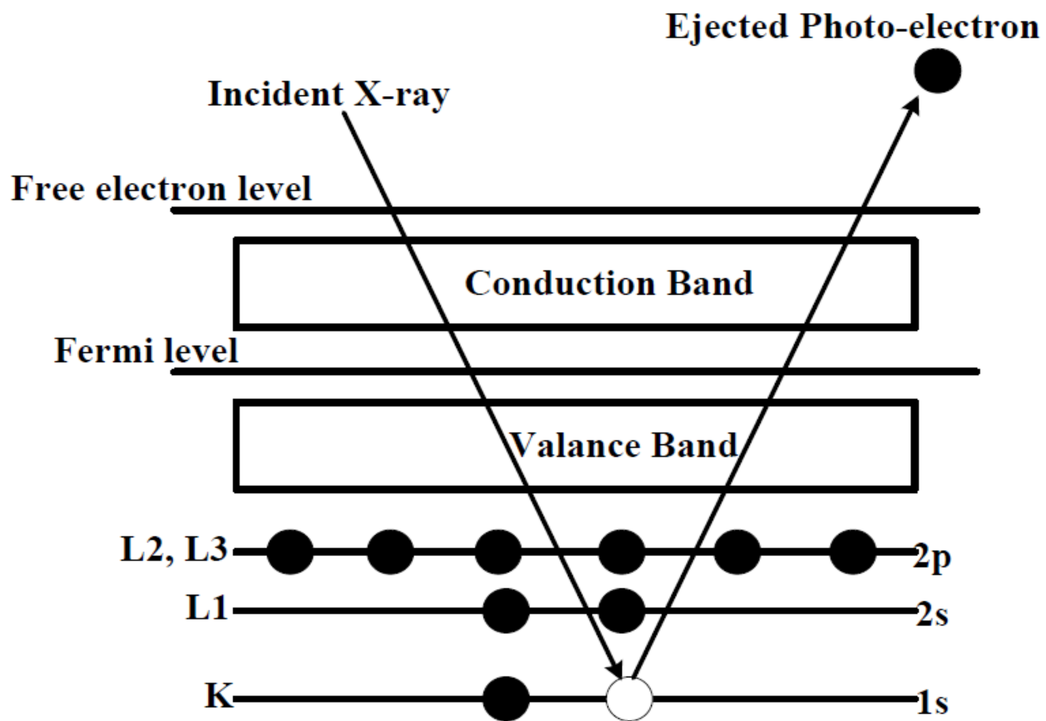

Figure 2-10: Principle of X-ray Photoelectron Spectroscopy (XPS) [123]

Chemical shifts due to different oxidation states (Nb^{2+}, Nb^{4+} and Nb^{5+}) in the Nb 3d core level can be observed by XPS. Deconvolution of Nb^{4+} and Nb^{5+} seems devious as an apparent irregularity prevails in the line shape. Specific line shape is chosen for fitting Nb 3d spectra which is the characteristic orbital for XPS analyses of Niobium and its compounds. Therefore, by using XPS analyses the chemical composition and Nb 3d core level structures of different Niobium Oxide s and V doped NbO_2 will be determined.

2.4 Surface Morphology

2.4.1 Scanning Electron Microscopy (SEM)

Scanning Electron Microscope (SEM) is an imaging tool that produces images of micro and nanoscale objects by scanning the surface with the use of focused beam of high energy electrons. The electrons are emitted from the tungsten or LaB_6 cathode filament source. The electron beam then passes through condenser lens and scanning or deflector coils that cause the beam to raster so that it can scan the sample.

Scanning can be done in the areas ranging from approximately 1 cm to 5 microns in width using conventional SEM techniques. Analyses can be performed in any preferable point

locations of the specimen. The coils at the objective lens deflect the electron beam linearly along x or y direction over the sample surface. The interactions between the electrons and the sample helps to release energy in the form of secondary signals that contains rich amount of Information reliant on the type of detector. Variety of signals are generated at the surface of solid specimen. A secondary electron detector forms a map of the surface topography by detecting the electrons reflected from the surface.

Secondary Electrons can create image with best spatial resolution as the Secondary Electrons (SE) have low energy below 50 eV [124]. It gives the information about the crystal morphology, particle size, surface defects etc. In the micro and nano scale a wide range of magnification can be attained. Back-Scattered Electron (BSE), generated by the elastic scattering of electrons, have higher energy than SE. Back-Scattered Electron (BSE) signal deliberates the chemical composition of the sample. From the contrast of the image the elements can be detected, for examples: elements with higher atomic mass shows brighter contrast in BSE images. Schematic of basic SEM is depicted in Figure 2-11.

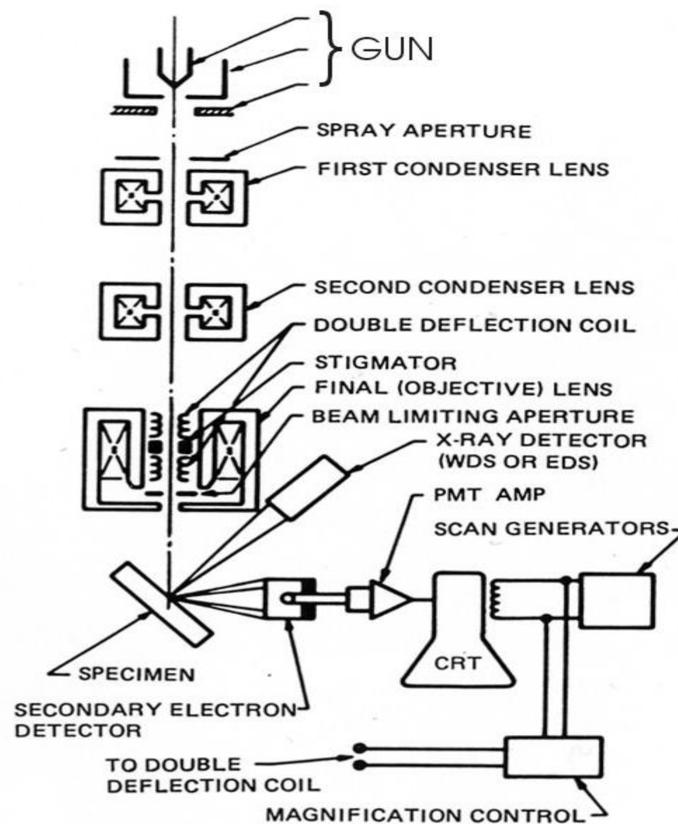

Figure 2-11 Schematic of SEM with Electron and X-Ray Optics [125]

Details atomic gas contents of each element or elemental mapping can also be analysed by the SEM with Energy Dispersive (EDS) facilities. This kind of instruments are based on the X-ray signal and X-ray is emitted from the atoms. Atoms can be identified by measuring the energy of x-ray whereas number of x-ray refers the gas content of atom [126]. When the detector analyses the wavelength of the X-ray it is called X-Ray Wavelength Dispersive (WDS) analysis. In short, SEM is especially convenient for qualitative determination of phases, chemical compositions (by EDS), crystal structures and orientations (by EBSD). Higher magnification images (up to 1,000,000X) can be acquired by this non-destructive testing. Thus, it is possible to measure preciously very small structures and objects down to 50nm in size. Samples can be focused in wide area of rough surface as SEM has larger depth of the field and therefore details 2-dimensional high-quality images are acquired. Specimen should be electrically conductive or semi conductive unless the instrument is capable of operation in a low vacuum mode. Therefore, a conductive layer of coating (e.g. gold, copper, carbon or some other material or alloy) may be required for electrically insulating samples. Since Nb_2O_5 is not conductive enough a carbon tape would be used before being put into the sample stage for SEM observation. The microstructures of different NbO_x thin films can be observed by this technique.

2.4.2 Optical Profilometer

Measuring the surface topography, film thickness and residual stress with high accuracy are vital for deposited coatings. Stylus profilometer, the most common and straightforward way, can be employed to measure the surface roughness, film thickness and stress of films where Stylus moves mechanically in vertical direction to measure the height difference in surface and moves horizontally to scan the surface. This movement of the stylus can scratch the film surface. Moreover, the accuracy of the stylus profilometer is limited to the dimensions of the stylus that is additionally affected by the step geometry, surface roughness etc. Therefore, the non-contact optical profilometer based on interferometry is of more interest because of its higher accuracy and reliability.

The precision of this well-established technique can be as high as 1 nm [126]. Figure 2-12 shows the basic structure of such kind of optical profilometer.

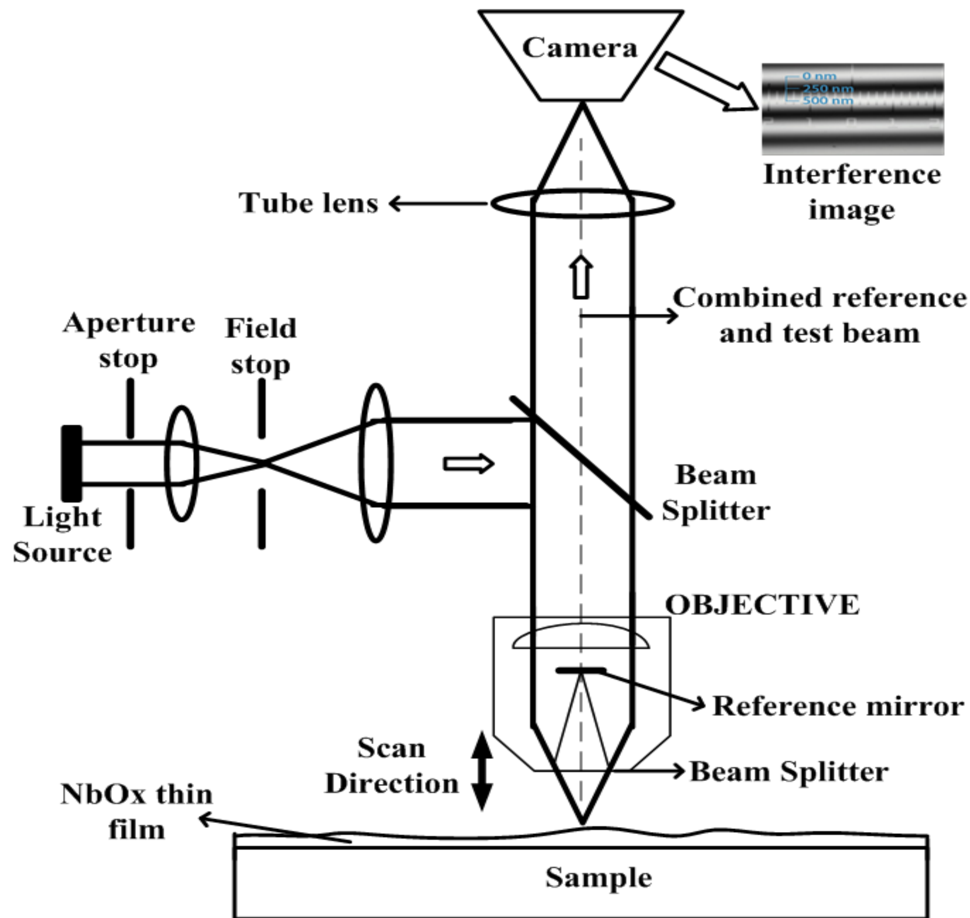

Figure 2-12: Schematic of Optical Profilometer based on Interferometry

(Modified from Zygo Co.)

No prior surface preparation is required for using this non-destructive technique. It works based on the light splitting and height variance: source beam light split into two beams. One beam is reflected from the reference mirror inside the objective and another beam is reflected from the specimen. These two beams create constructive and destructive interferences resulting in the bright and shady bands in the fringe on the sample surface. When the path difference of reflected light between the reference mirror and specimen equals the integral number of the wavelength constructive interference is created. Destructive interference happens whenever the length of the light beams fluctuates. These interference beams are focused into the digital camera. Reference mirror is close to seamless flat surface. Therefore, optical path variance generates from the height difference of the specimen surface. Wave properties of light is used to compare the optical path difference. Height difference can be calculated if the wavelength is known.

A surface measurement (3D surface map) can be conducted from this height differences. This device can be used in many industries for many circumstances where micro measurement of surface differences is essential. By considering the surface height variance roughness is calculated whereas film thickness is measured directly from the step height difference with bare substrate. The radius of curvature is measured before and after film deposition that can be used to calculate the residual stress with the help of Stoney's equation. Other specific properties of the substrate is also needed for stress measurement, such as thickness, Young's Modulus and poisson's ratio.

Precision of stress measurement by this method is usually related to systematic radius of curvature measurement errors, film uniformity, sample shape etc. Typical measurement uncertainty can be as high as ±50MPa. This surface sensitive technique will be used to measure the roughness of the deposited thin films. Curvature of any surface can also be measured by using this technique. Residual stress of the thin films can then be calculated by measuring the curvatures before and after thin film depositions.

2.5 Mechanical Characterizations

2.5.1 Nano Indentation

Mechanical properties like Hardness and Young's Modulus can be measured by using depth-sensing Nano-indentation. This dynamic testing is based on the measurement of the vertical position of the indenting stylus throughout its movement during measurements. Oliver-Pharr method helps to calculate the hardness and Young's Modulus analytically from the obtained load vs displacement curve [127]. The size of the indenter and penetration depth affects the obtained values [128]. It should be taken into consideration that the device is perfectly calibrated before the measurements. For soft thin films it is difficult to avoid the substrate effects on the measurement values. Therefore, the film thickness should be several times larger (ten times) than the penetration depth of the indenter [127].

For thicker coatings hardness can be measured directly at a fixed indentation size and the Indentation Size Effect (ISE) index. For thin films a typical model is followed to determine the actual hardness of thin films and ISE index to overcome the substrate effect on the measurement [129].

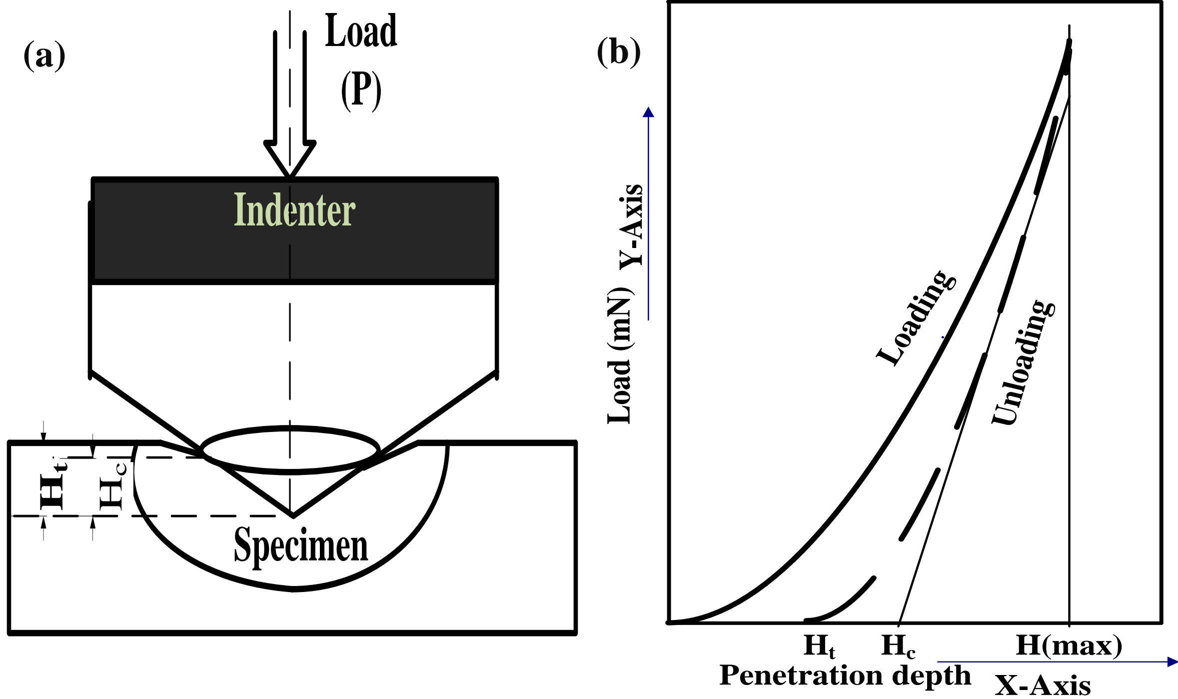

Figure 2-13: (a) Contact Geometry (b) Load Displacement Curve of Nano-Indentation

Therefore, for using the Nano-Indentation multiple load is applied to observe the penetration depth and finally load is selected in such a way to overlook the effect of substrate and roughness of thin films. Nano-Indenter can uninterruptedly monitor the load and displacement while penetrating the film. Projected area of indentation is determined from the load and displacement information. Elastic deformation is of less interest; therefore, those elastic deformation values are disregarded. Plastic depth is accountable for determining the area using the geometry of the indenter. Figure 2-13 shows the contact geometry of the indenter and Figure 2-13illustrates the typical load-displacement curve. in the unloading curve, from maximum load point to the X-axis a tangent line is drawn. Young's Modulus is associated with the gradient of the tangent line.

Hardness, *H* can be calculated by using the formula:

$$H = 0.378\frac{P_{\max}}{H_c^2} \tag{2-8}$$

where, P_{max}, H_c^2 indicates the maximum load and plastic deformation respectively. Elastic deformation is determined from the difference between maximum indent, H_{max} and plastic deformation, H_c.

Young's modulus can further be calculated by using the following equation:

$$E = 0.179\,\frac{(1-\upsilon^2)P_{\max}}{(H_{\max}-H_c)H_c} \tag{2-9}$$

As this technique is very sensitive to vibrations and sample roughness. The measurements should be taken in stable noiseless place and the surface roughness should be abolished by excluding the lower depth values. This technique will be used to measure the hardness and Young's Modulus of the deposited thin films.

2.6 Optical Characterization

2.6.1 Optical Spectrophotometer

Spectrophotometer displays the optical transmittance or reflectance properties of a material as a function of wavelength. The device basically measures the intensity of light when a beam of light passes through the specimen. The beam of light contains a stream of photons. When the light falls on the substance the light can be reflected or transmitted or can be absorbed. In spectrophotometry reflection of light is of minimal interest, therefore the absorbance and transmittance are considered mainly. Each substance absorbs or transmits light within a certain array of wavelength. Absorption basically decreases the number of photons in the beam of light and thus the intensity of the light beam reduces.

Spectrophotometer is comprised of two devices- a spectrometer and a photometer. Spectrometer initially generates desired range of wavelength of light. The beam of light is dispersed into several component of wavelength while passing through a monochromator and the slit then transmits only the desirable wavelength through it. The photometer helps to measure the intensity of light by detecting the number of absorbed photons.

It is one of the most beneficial procedures of quantitative study in different scientific laboratories as well as in production industries. Spectrophotometer with Ultra Violet- Visible-Near Infrared Radiation (UV-VIS-NIR) range is more suitable for wide range of practical applications as it can be used for any kind of samples. Spectrophotometers may also be used for the estimation of number of cells in suspension.

A basic mechanism of the spectrophotometers can be explained by the Figure 2-14. There are several mirrors in the system marked as M1, M2, M3, M4, M5, M6, M7, M8, M9,

M10, M11, M12, M13, M14 and two monochromators (G1 and G2) for functioning in different mode.

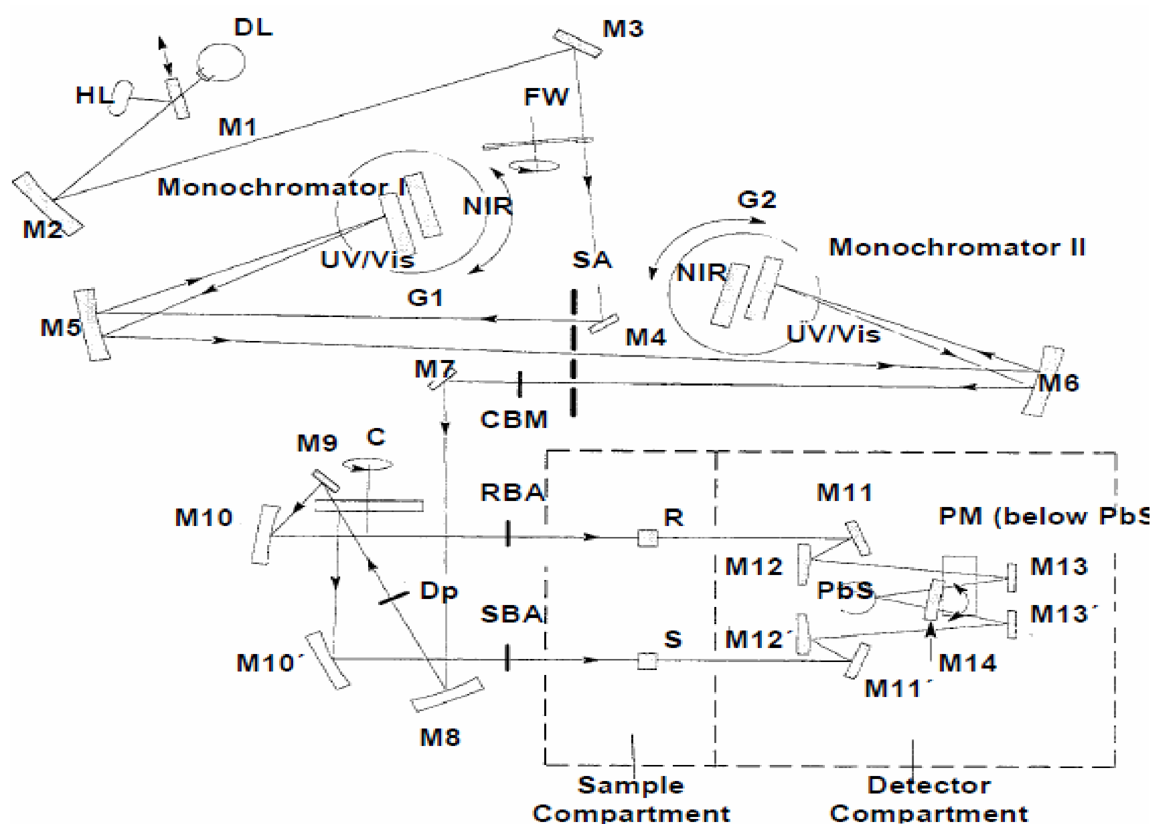

Figure 2-14. Schematic of Optical System [130]

Mirror M1 basically helps to choose the source lights. When the spectrometer operates in the VIS/NIR range halogen lamp is functional and deuterium lamp is blocked by mirror M1. At that time mirror M1 reflects the radiation from the halogen lamp on mirror M2. Radiation from deuterium lamp hits the mirror M2 while operating in UV range. Mirror M1, M2, M3, M4, M5, M6 direct the light from source to monochromators. Slit Assembly (SA) and optical Filter Wheel assembly (FW) helps the monochromators for choosing the specific filter for certain wavelength. Light then passes through the mirror M7, M8 and CBM-common beam mask and the C-chopper. If the C- chopper is inactive light passes through the RBA- Reference Beam Attenuator into the compartment after reflection from the mirror M9 and M10. Reference beam is thus created inside the sample compartment and the beam intensity is measured by PM-Photo Multiplier for light in the UV/VIS range or by Peltier-cooled lead sulfide detector for the NIR range. If the C -chopper is active the light passes through the Sample Beam Attenuator (SBA) into the compartment after reflecting by mirror M10 that creates sample beam.

Consequently, light then passes through the sample and are detected by the detectors. The radiation width can be varied and depends on the slit width, for example at a slit width of 5nm each radiation beam width can be 4.5 mm. The radiation beam height can be reduced from the maximum height of 11.7 mm to 0.0mm in 50 steps. The UV WinLab L800/L900 software is used to control the scan settings and the measurements are taken for every wavelength.

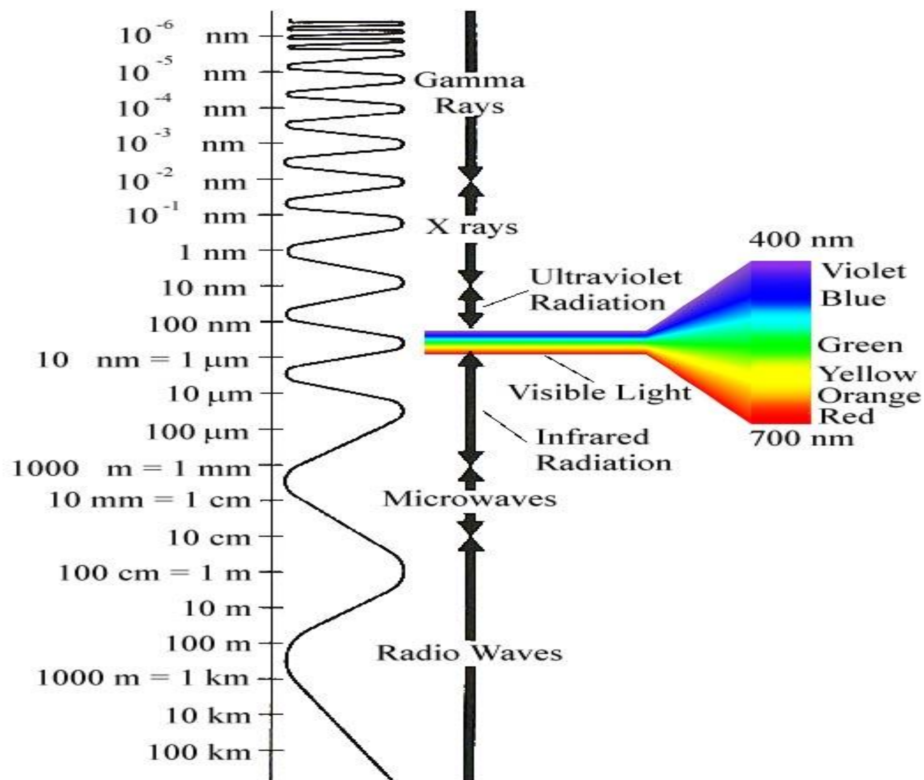

Figure 2-15: Wavelength Range of Different Lights (internet)

This measurement can also be utilised to quantify the amount of a known chemical elements. In this dissertation optical spectrophotometer will be used to measure the transmittance of the thin films. Optical constants will be extracted thereafter from the transmittance and absorbance data.

2.7 Electrical Characterizations

2.7.1 Four Point Probe

Four-Point Probe method is the simplest and widely used technique for resistivity measurement of thin films. Unlike the Two-Point Probe method no calibration is necessary for this technique.

There is sperate probe for current and voltage measurement which helps to eliminate the lead and contact resistance. Current is applied from constant current source and it has a voltmeter to measure the voltage. Appropriate Currents can be applied by pressing the buttons in nA, μA or mA scale. High currents are required for highly conducive samples. Usually, current should not be applied higher than 10mA to avoid excessive localized heating of the sample. Current is supplied by the two outer probes and the two inner probes measure the induced voltage.

From the applied current value and the induced voltage reading the resistance can be calculated (using equation) and thus the sheet resistance and bulk resistivity of the material is calculated by multiplying with the sample thickness.

$$\rho_s = \frac{\pi}{\ln 2}\frac{V}{I} \tag{2-10}$$

where, V is the voltage reading of the inner probes, I is the current readings of the outer probes, ρ_s is the resistivity of the sample.

Film thickness is multiplied with the sheet resistivity to measure the bulk resistivity of the material. Therefore, bulk resistivity of the sample ρ is:

$$\rho_s = \frac{\pi}{\ln 2}\frac{V}{I}\times t \tag{2-11}$$

where, t is the film thickness.

When the film thickness is more than half of the probe space the equation becomes:

$$\rho_s = \frac{V}{I}\frac{\pi t}{\ln\left(\dfrac{\sin h(\frac{t}{a})}{\sin h(\frac{t}{2a})}\right)} \tag{2-12}$$

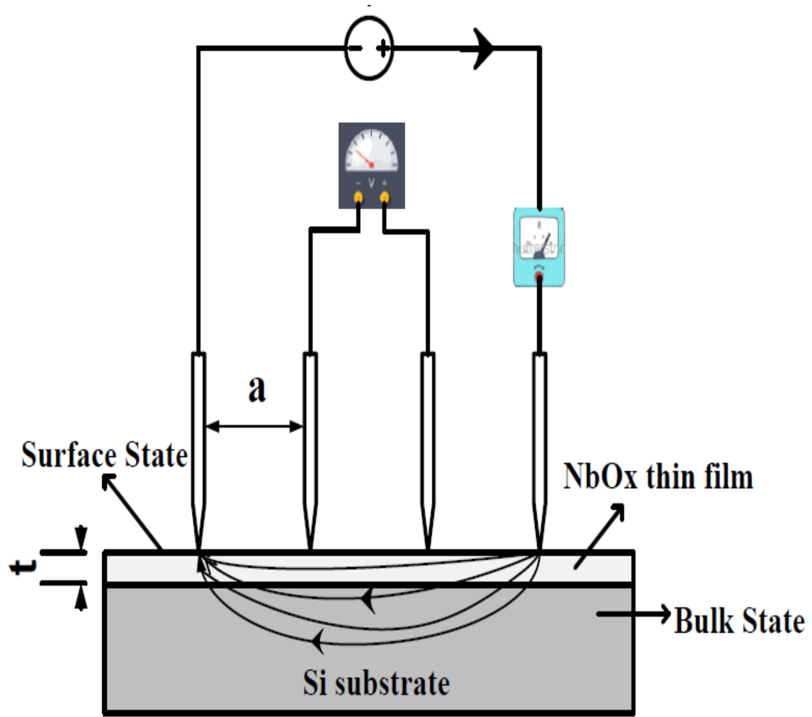

Figure 2-16: Schematic of Four-Point Probe Configuration

3. Experimental Methods

3.1 Thin Film Deposition

In the present research, Magnetron Sputtering Deposition System (Model: SPT320 - PLASMIONIQUE) was employed to deposit the thin films. The system is equipped with three magnetron sputtering guns, shield chimney and shutter, substrate holder (allow D=4” substrates), remote Inductively-Coupled Plasma (ICP) source (PLUME series) etc. that offer substantial development of PVD, PECVD, multilayer films and opportunity for advance material synthesis application. Substrate can be heated up to 850 °C and substrate RF biasing may be applied. The overall view of the system is presented in Figure 3-1.

3.1.1 DC/RF Sputtering

Formation of Plasma is the first step of DC sputtering. Metallic Nb target here acts as cathode and substrate as anode. The sputtering chamber, made with stainless steel, is occupied by Argon as sputtering gas. While DC power is applied to the electrode’s plasma will be created. The color of the plasma depends on the pressure and gases inside the chamber. High energy electrons and gas molecules collide with each other and the gas molecules become ionised. These ions intrude the surface of the target and Nb atoms are displaced from the target surface. These displaced Nb atoms forms the thin films after reacting with oxygen in chamber.

There are several parameters for thin film preparation by sputtering method. Tuning the exact process parameters to form specific thin film and to control the properties of deposited NbO_x thin film is difficult. Most important parameter for optimising the chemistry of NbO_x films is to vary the Oxygen flow rate during deposition and keeping all else constant. However, the formation of specific NbO_x also depends on the surface state of the Nb target, power density and vacuum pressure.

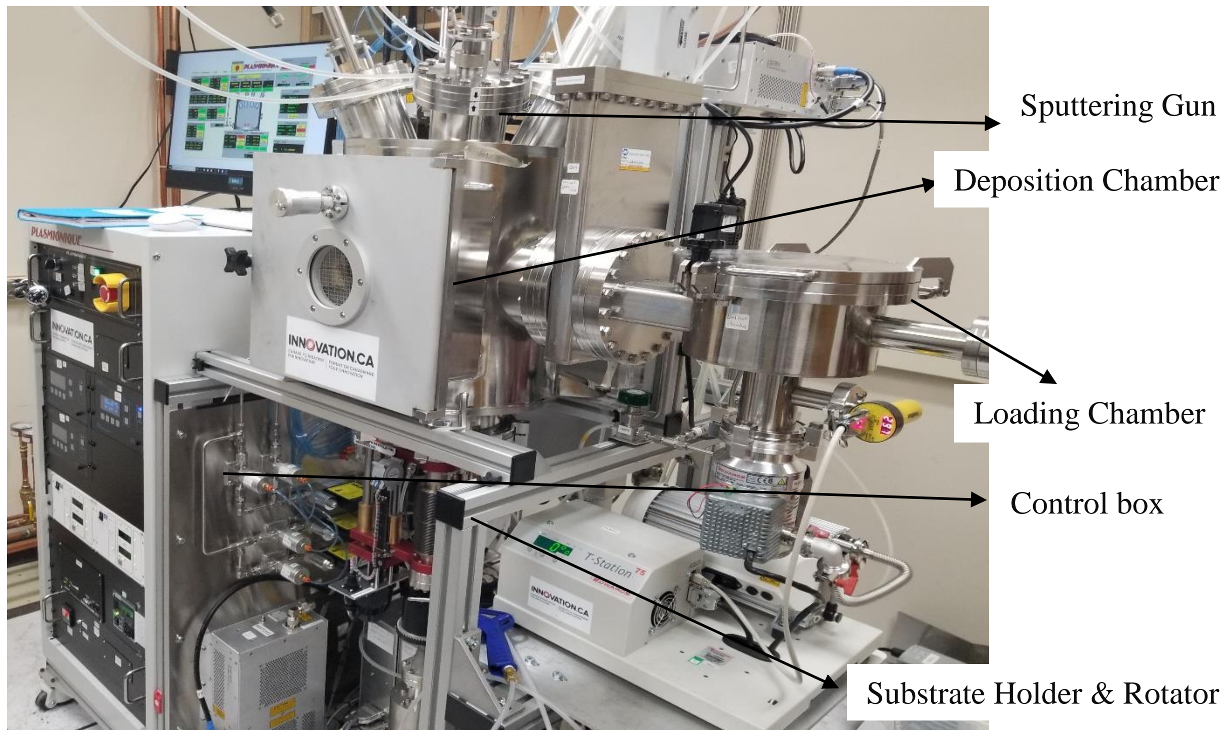

Figure 3-1: Overall View of the Sputtering Deposition System

3.2 Experimental Design

In this work, Niobium Oxide thin films with different oxygen gas contents were deposited on Si (001), Quartz and amorphous glass substrates by DC and RF magnetron sputtering. Effects of the deposition parameters on the structures of Niobium Oxide s were investigated systematically. Nb-O system is very complex and therefore synthesis of specific stoichiometric Niobium Oxide without any secondary phase is very challenging. Small stoichiometric variations may modify the structural properties. For Niobium Oxide s formation, the first challenge is adjusting Ar and O_2 flow rate in the deposition chamber. The straightforward way is tuning the flow ratio between oxygen and argon.

Target material for sputtering is typically compound or elemental type based on the deposition conditions in the reactive gas environment. Miscellaneous compounds (e.g. oxide, nitride, carbides etc.) can be deposited using reactive sputtering in an environment containing O_2, N_2, or hydrocarbon gases. Reactive gas reacts with the sputtered Nb and forms the desired compound coatings. At the same time, a compound layer can also be formed on the target surface.

The target can be denoted as poisoned if the compound layer formation surpasses the sputtering rate. Niobium is highly reactive with oxygen and a Niobium Oxide compound is formed on the metallic target surface during deposition that reduces the deposition rate. Moreover, this dielectric oxide layer may cause arcing due to positive charge accumulation by impacting ions. Therefore, droplets can be formed, and quality of the coatings subsequently declines.

Target poisoning and arcing can be minimised by lowering the reactive gas content and adjusting the partial pressures of Ar and O_2. Compound layer is more prominent on the centre of the surface and the sides of the target than the racetrack areas that is illustrated in Figure 3-2. Significant erosion occurs on the racetrack areas due to more ion bombardment on these areas, whereas other portions are seen as undamaged. Erosions on these specific areas also lowers the deposition rates.

Therefore, after several depositions the Niobium target should be changed or polished to make a plain surface in order to overcome the unusual variation in the growth rate. Also, to eliminate the surface defects or impairment formed by thermal shock the target requires to be changed or polished after several depositions.

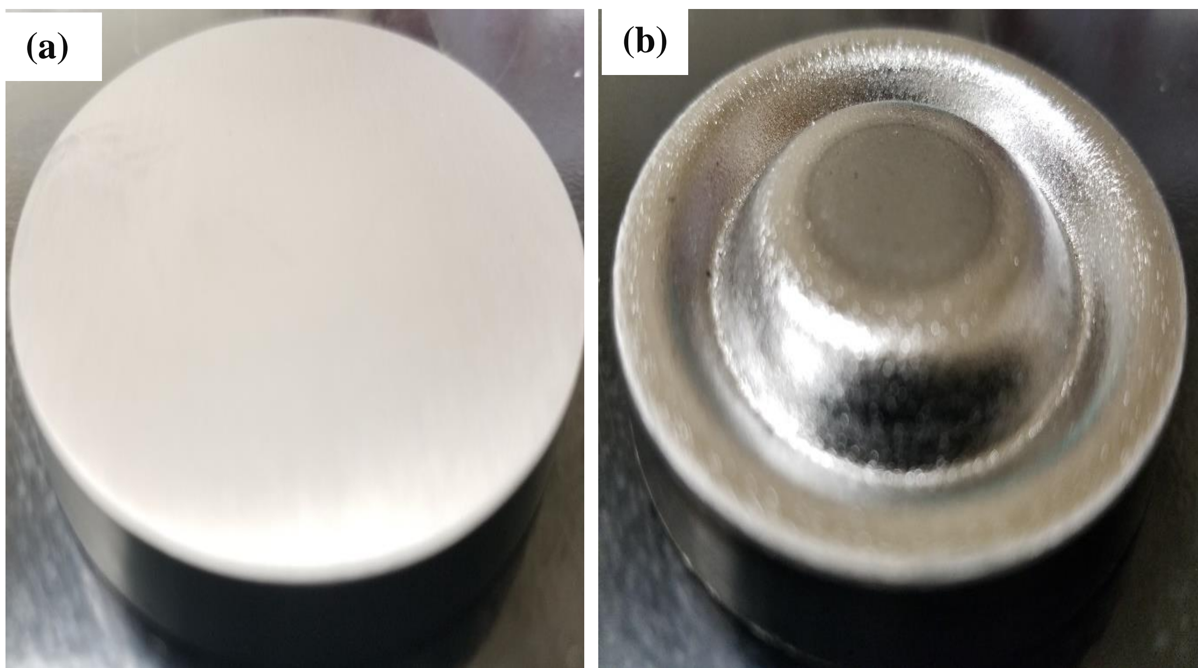

Figure 3-2: Nb Metallic Target (a) Before and (b) After Sputtering

During magnetron sputtering depositions, there are several deposition parameters that can affect the qualities or properties of the thin films. For Niobium Oxide formation, the first challenge is adjusting Ar and O_2 flow rate in the deposition chamber. The straightforward way is tuning the oxygen flow ratio with respect to Ar flow rate. By changing these two-gas ratios we can manipulate the oxygen gas contents during deposition which is the most significant parameter for film formation. Other parameters including deposition temperature, working pressure, and the power source for sputtering have also effects on the properties and qualities of thin films. Niobium Oxides exhibit several different structures and phases depending on the deposition temperature, pressure and oxygen gas content. Therefore, following deposition parameters shown in Table 3-1 were chosen to deposit the thin films samples.

Table 3-1: Deposition Parameters of NbO_x

Power: Nb (W)	**Ar (sccm)**	**O_2 (sccm)**	**% of O_2 (%)**	**Pressure (mT)**	**Temperature (° C)**	**Remark**
DC 200	50	0	0%	8 mT	720 °C	Effect of O_2 gas contents
DC 200	100	1.4	1.5%	8 mT	720 °C	
DC 200	95	3.5	3.5%	8 mT	720 °C	
DC 200	50	2.7	5%	8 mT	720 °C	
DC 200	50	3.5	6.5%	8 mT	720 °C	
DC 200	50	4.7	8.5%	8 mT	720 °C	
DC 200	50	10.6	17.5%	8 mT	720 °C	
DC 200	50	13.8	21.5%	8 mT	720 °C	
DC 200	96	1.4	1.5%	8 mT	30 °C	Effect of Substrate Temp
DC 200	60	2.5	4%	8 mT	650 °C	
DC 200	50	4.7	8.5%	8 mT	30° C	
DC 200	50	10.6	17.5%	8 mT	650° C	
DC 200	100	1.5	1.5%	16 mT	720 ° C	Effect of deposition Pressure
DC 200	96	1.4	17.5%	16 mT	720 °C	
RF 150	100	1.5	1.4%	8 mT	720 °C	Effect of Power source
DC 200	96	1.4	1.5%	8 mT	720 °C	
RF 150	50	2.7	5%	8 mT	720 °C	
DC 200	50	3.5	6.5%	8 mT	710° C	

Higher oxygen flow rates and pressure are linked with lower sputtering yield and leads to form thinner films. Lower power density associates lower amount of Nb in the coating thus over stoichiometric NbO_x is formed. Therefore, to optimise and improve the NbO_x thin films quality it is necessary to know the fundamentals of sputtering.

The dislodged Nb atoms are flown in the chamber and deposited on the substrate placed in the bottom of the chamber, make the desired thin film.

Quality of thin film depends on specific deposition parameters. Substrates are kept on a substrate holder that is placed on ceramic substrate heater and heating is done by applying current through the heater. A thermocouple is placed beneath the substrate heater to measure the deposition temperature. A set of Niobium Oxide s were deposited under different temperatures with other growth c parameters remaining constant as listed in Table 3-1. The deposition temperature and oxygen gas content are the most important experimental parameters for the formation of particular phases.

Based on the conditions for deposition of NbO_2 thin films with high purity, doped NbO_2 thin films can be deposited by co-sputtering Nb and V targets simultaneously. In order to obtain NbO_2 thin films doped with different amount of vanadium, the powers for sputtering two targets were changed as shown in Table 3-2 by keeping other parameters similar for NbO_2 deposition. Based on the deposition parameters for NbO_2, the sputtering power of Nb target was fixed to 200W and sputtering power of V target was changed consequently. Detailed deposition parameters are presented in Table 3-2.

Table 3-2: Deposition parameters for V doped NbO_2

Sample #	**Power: Nb (W)**	**Power: V (W)**	**O_2 (sccm)**	**Ar (sccm)**	**% Of O_2**	**Temperature (°C)**	**Pressure (mT)**
S01	DC 200	DC 90	1.8	96	1.46	720	8 mT
S02	DC 200	DC 100	1.4	95	1.4	720	9 mT
S03	DC 200	DC 130	1.6	96	1.5	720	8 mT
S04	DC 200	DC 150	1.4	95	1.4	720	10 mT
S05	DC 150	DC 150	1.4	95	1.4	720	10 mT
S06	DC 100	DC 150	1.4	100	1.4	720	8 mT

3.3 Effect of Annealing

Another simple method of preparing NbO_x thin film is to anneal the metallic Nb thin films at different temperature for different durations. The advantage of this process is the oxide film thickness can be controlled by the initial thickness of the Nb film. Moreover, there is no need of oxygen plasma during deposition and oxide film can be continuous. Thin metallic Nb coating are deposited on Si (100) substrate by magnetron sputtering method. The as deposited films were annealed for different temperatures ranging from 500°C to 900°C.

3.3.1 Post-deposition annealing

Annealing of NbO_2 and Nb_2O_5 thin films deposited by sputtering was carried out in Ar and/or Air atmosphere at different temperatures for few hours in order to determine the thermal stability of the structure.

NbO_2 thin films deposited with different oxygen gas contents were annealed in Ar atmosphere. Annealing was done in a tube furnace with a heating rate of 15°C/min in Ar atmosphere. Ar pressure was kept at 8 MPa. This Ar environment usually works as a reducing atmosphere to form different phases of Nb oxide.

Sputtered amorphous Niobium pentoxide thin films were also annealed in Ar atmosphere at different temperatures with the aim to produce NbO_2. It was found that Nb_2O_5 transformed into NbO_2 at high annealing temperatures of above 500°C. The required temperature and duration of annealing to form NbO_2 depend on the as-deposited film thickness and properties.

3.4 Characterization Techniques

3.4.1 X-Ray Diffraction (XRD)

The crystallinity of the films was evaluated by X-ray Diffraction. The measured XRD patterns were matched with the Joint Committee on Joint-Committee Powder Diffraction Standards (JCPDS) database, using X'Pert High Score Plus software to identify the Niobium Oxide peaks. The peak positions and width of highest intensity first order Bragg diffraction peak were used to estimate the crystalline size using the Scherrer formula (discussed below). Most of the XRD analyses were done in plasma physics lab using a Co K_α (λ = 1.78 Å) radiation source operating at 30 kV and 20 mA and a few analyses were done by the grazing XRD in SSSC using Cu K_α(λ = 1.54 Å).

XRD peaks are fitted by a Gaussian equation to calculate the FWHM. It should be noted that the instrumental peak broadening is negligible as the FWHM of the diffraction peaks of single crystal silicon is close to zero. Considering the Bragg diffraction peak of the highest intensity, the average crystallite size (*D*) is assessed by the Scherrer equation [131],

$$D = \frac{K\lambda}{\beta \cos\theta} \quad (3\text{-}1)$$

In Equation (3-1), D is the average grain size, K is the Scherrer constant, λ is the x-ray wavelength and β is the width of the diffraction peak. A more accurate way to estimate the grain size is to use the Williamson-Hall-Isotropic Strain Model (WH-ISM) involving a series of diffraction peaks [131,132].

$$\beta\cos\theta = \frac{K\lambda}{D} + 4\varepsilon\sin\theta \tag{3-2}$$

where, ε is the strain in the film. A plot can be drawn by taking $4\sin\theta$ as X-axis and $\beta\cos\theta$ as Y-axis and the lattice strain values and the crystallite size values can then be extracted from the slope and the intercept of the respective linear fit, respectively [131].

3.4.2 Raman Spectroscopy

The Renishaw Invia Reflex Raman microscope (Renishaw, Gloucestershire, UK) equipped with an IlluminatIRII FTIR microscope accessory (Smith's Detection, Danbury, CT), located in Saskatchewan Structural Science Center (SSSC), University of Saskatchewan, was used to determine the structure of the coatings. The measurements were taken at 514.5 nm (Modulaser StellarPro-50) wavelength with Ar ion laser in a spot size of 1.5 μm approximately. Before performing test, internal calibration was done with standard silicon which has peak position at 520 cm^{-1} or 521cm^{-1}. For higher credibility of the data, three different spots were analyzed for each sample with exposure time of 10 s. Accumulation of the data was 3 times or 5 times to minimize the background noise. Cosmic ray removal mode was enabled to avoid any effect from cosmic rays. The Wire3.3 software package was used to analyse the Raman spectrum results. As Raman spectra are based on laser light scattering, the transparency of the thin film has effect on the peak intensity. When the thin film is more transparent, the substrate peak is more intense. The substrate peaks are subtracted using the software for clarity.

3.4.3 X-ray Photoelectron Spectroscopy (XPS)

XPS analyses help to identify the core level lines of Niobium and oxygen, relative atomic percentages of existing elements and oxidation state of Nb from the Nb 3d doublet. All X-ray Photoelectron Spectroscopy (XPS) measurements were collected using a Kratos (Manchester, UK) AXIS Supra system at the Saskatchewan Structural Sciences Centre (SSSC).

This system is equipped with a 500 mm Rowland circle monochromatic Al K-α (1486.6 eV) source and combined Hemi-Spherical Analyzer (HSA) and Spherical Mirror Analyzer (SMA). A spot size of hybrid slot (300 X 700) microns was used. All survey scan spectra were collected in the -5-1200-binding energy range in 1 eV steps with a pass energy of 160 eV. High resolution scans of 2 regions were also conducted using 0.05 eV steps with a pass energy of 20 eV. An accelerating voltage of 15 keV and an emission current of 15 mA was used for the analysis. Argon sputtering was done on each spot using a 4 keV source for 1 minute to remove the surface layer.

3.4.4 Optical Profilometer

Zygo New View 8000 optical profilometer located in room OC19, Engineering building, at University of Saskatchewan was used to observe the surface topography (roughness), to measure the film thickness and radius of curvature of the substrate before and after thin film deposition. This device offers powerful flexibility in non-contact optical surface profiling measurement with higher speed. All kind of surfaces including smooth, rough, fast, stepped etc can be measured accurately by this highly automated device. All data points are observed to regulate most detailed focal point that result in very details and sensitive surface measurement. By using the radius of curvature values residual stress of thin films were calculated with the help of Stoney's equation.

3.4.4.1 Stress Measurement

Stress can be measured in several ways. In our case, we have used a straightforward technique to measure the surface curvature by an optical profilometer. The total stress in the thin films was assessed using the Stoney formula by measuring the sample curvature (R) before and after film deposition in an optical profilometer [133]. The total stress was then calculated using the following formula [133]

$$\sigma = \frac{1}{6R} \frac{E_S d_S^2}{(1 - \nu_S) d_f} \quad (3\text{-}3)$$

where E_s is Young's Modulus and ν_s is the Poison ratio of the substrate (Si), d_s and d_f are the thickness of the substrate and film, respectively, R is the net change of curvature of the substrate before and after deposition [133].

The curvature measurement was done multiple times along two perpendicular directions (parallel to the substrate edges) on the surface, and the average values were used to estimate the residual stress in the samples. More specifically, the curvature measurements were taken on the samples horizontally and vertically before and after the thin film's deposition. Each sample was scanned using the stitching mode of the profilometer to determine the curvature of the sample before and after deposition. Particularly, the measurements were taken on the same spots for the same sample before and after deposition to reduce errors. Two differently shaped substrates (6 mm × 4 mm) and (4 mm × 40 mm) were used for each of the NbO_2 and Nb_2O_5 thin films. As slight substrate offsets in the substrate positions can create a large error, substrate positions and focusing were done very carefully.

3.4.5 Scanning Electron Microscope

The Joel JSM-6010LV Scanning Electron Microscope (SEM) located in room 2C25 at Engineering building was used to perceive the surface morphology and cross sections of the deposited films. For higher quality imaging a few samples were also analyzed by Field-Emission Scanning Electron Microscope (FE-SEM) in WCVM Imaging Centre, Western College of Veterinary Medicine, U of S. Carbon and Copper tap were used to increase the conductivity of some samples. As the configurations of these two SEMs were different, operating conditions were also different for analysing samples. Joel JSM-6010LV was operated at 12 keV energy whereas FE-SEM were used at 3 keV energy. Best possible images were acquired using secondarily electrons.

3.4.6 Nano-Indentation

Nano Hardness and Young's modulus were determined by nano-indentation tests by a Universal Mechanical Tester (UMT) placed at Room 1B22, Engineering Building of U of S. A 100 nm Berkovich Indenter tip was positioned perpendicularly on the sample surface that penetrated the sample surface while increasing the load. Each loading was done for 60s to avoid possible creeping. A matrix of 5 × 3 spots was set for each sample to confirm the reproducibility of the hardness data. Specifically, the measurements were done using low loads ranging from 3 mN to 6 mN to avoid the influence of the substrate. During the measurements, the penetration depth was usually between 15% and 20% of the thickness, even though widely used rule of thumb restricts the penetration depth to less than 10% of film thickness for soft films [145].

After choosing the proper load to get reliable data, the hardness and Young Modulus values were calculated from the loading and unloading curves using a software based on Oliver and Pharr method.

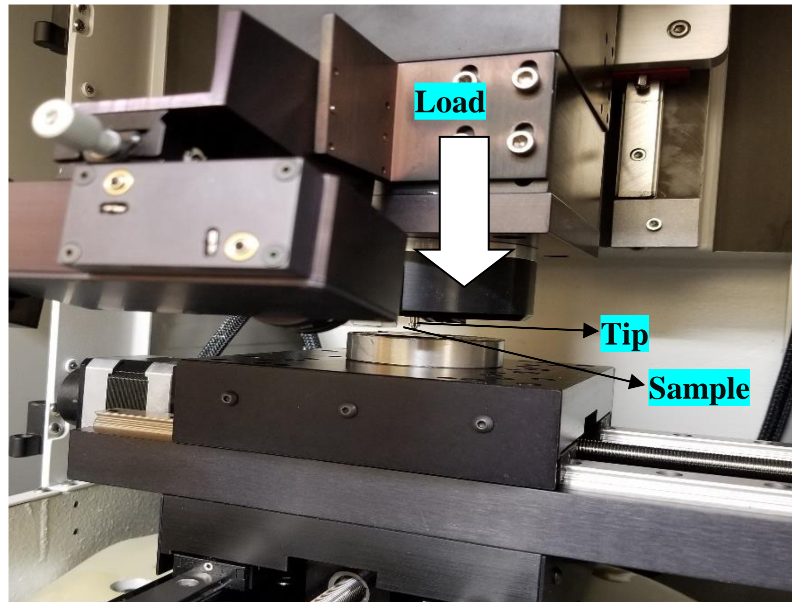

Figure 3-3: Photograph of Universal Mechanical Tester for Nano-Indentation Investigation

3.4.7 Four-Point Probe

Jandel Four -Probe was used for measuring the electrical resistivity/conductivity of the thin films. Spacing between two adjacent probes of this device is typically 1mm which is higher than the film thickness. Sample size was greater than 25 × 25mm to minimise the measurement errors. During measurement probes should gently touch the surface of thin films; however, it should be carefully observed that the probes are not excessively forced to the surface. If the voltage reading shows “out of range” or “contact limit error” the probe should be lifted, and further reading should be taken for reduced current values. However, there is a limitation for measuring highly insulated materials. Conductivity can also be measured directly from the 4-point probe in ohms/square scale:

$$\text{Conductivity (S/m)} = 1/(R \times t) \tag{3-4}$$

Where, R = resistance in ohm/area, t = thin film thickness.

Electrical conductivity is a property showing large variation among various material systems. It depends on the concentration of carriers and their mobility. Four-point probe technique was used to measure the film conductivity, which needs the thickness *t* of the film as well as the sheet resistance R_s. The thickness was measured by SEM, and the lateral resistance through a thin square of the sample was measured directly from the four-point probe, considering the geometry of electrical contacts that are positioned over surface.

Four-Point Probe technique was used to measure the film conductivity, which needs the thickness t of the film as well as the sheet resistance R_s. The thickness was measured by an SEM, and the lateral resistance through a thin square of the sample was measured directly from the four-point probe, considering the geometry of electrical contacts that are positioned over the surface.

The electrical conductivity (σ) can be measured from

$$\sigma = \frac{1}{R_s t} \tag{3-5}$$

Where, R_s is sheet resistance (Ω/area) and t is the film thickness (nm).

3.4.8 Spectrophotometer

Transmittance (%) were measured for wide range of wavelength by using PerkinElmer Lambda 900 spectrophotometer. This versatile spectrometer can be operated in the Ultra-Violet, Visible and Near Infrared (UV/VIS/NIR) spectral ranges. Deuterium Lamp (DL) produces the ultraviolet (UV) light and a Halogen Lamp (HL) produces the Visible (Vis) and Near Infrared (NIR) light. The lamps are turned on few minutes before starting the experiments for stabilizing the spectrum.

A schematic diagram of the spectrometer is depicted in Figure 3-4.

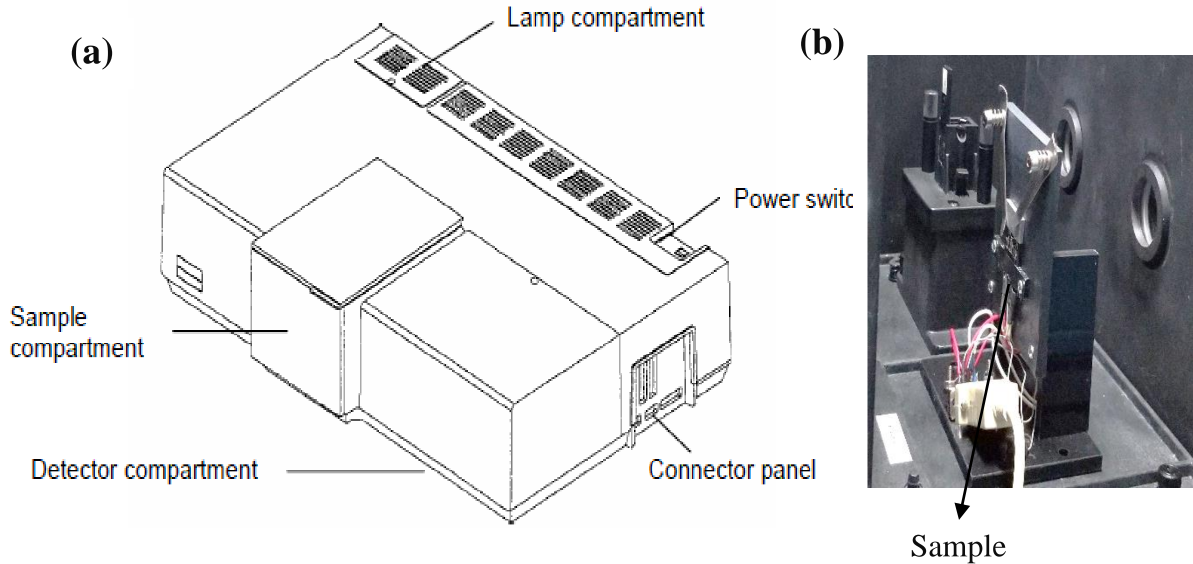

Figure 3-4. (a) A sketch of the Exterior of Spectrophotometer[130]. (b) Sample Compartment

For this project the typical scan from 2500nm to 1000nm for Si (100) substrate and 2500nm to 260nm for SiO2 substrate was being collected in every nanometer. Detection speed was 500nm/min. Several spots of the samples were measured for the higher reliability of the transmittance values. There is also heating facilities with the system that can heat up the samples up to 150 °C.

There are several methods to identify the optical constants based on refractometry and spectrophotometric measurements of T and R, polarimetry and spectrophotometric ellipsometry. By using specific model and curve fitting the optical absorbance is determined and other optical constants are segregated from the graphs.

3.4.8.1 Optical Constants

Refractive index and absorption coefficient as well as the light scattering coefficient of Niobium Oxide thin films were determined by fitting model calculations to the experimental transmission spectrum data obtained on thin films deposited on quartz substrates. In this calculation, the modified Swanepoel method has been used [134]. The following description is the core of the method and modifications required in this particular case.

According to Swanepoel technique, the spectral dependence of optical transmittance $T(\lambda)$ of a non-uniform thin film with average thickness d and thickness variation over the field of illumination Δd may be expressed as

$$T(\lambda) = \int_{\varphi_1}^{\varphi_2} \frac{A(\lambda)X(\lambda)}{B(\lambda) - C(\lambda)X(\lambda)\cos(\varphi) + D(\lambda)X(\lambda)^2} d\varphi \qquad (3\text{-}6)$$

where λ is a light wavelength, $\varphi = 4\pi nd/\lambda$, $\varphi_1 = 4\pi n(d-\Delta d)/\lambda$ and $\varphi_2 = 4\pi n(d + \Delta d)/\lambda$, where $n(\lambda)$ is wavelength dependent refractive index. The functions $A(\lambda)$, $B(\lambda)$, $C(\lambda)$ and $D(\lambda)$ are defined as

$$A(\lambda) = 16n(\lambda)^2 s, \qquad (3\text{-}7)$$

$$B(\lambda) = [n(\lambda) + 1]^3[n(\lambda) + s^2], \qquad (3\text{-}8)$$

$$C(\lambda) = 2[n(\lambda)^2 - 1][n(\lambda)^2 - s^2] \text{ and} \qquad (3\text{-}9)$$

$$D(\lambda) = [n(\lambda) - 1]^3[n(\lambda) - s^2] \qquad (3\text{-}10)$$

where s is the refractive index of substrate, which is assumed to be independent of λ. Finally, the function

$$X(\lambda) = \exp[-\alpha(\lambda)d] \qquad (3\text{-}11)$$

where in the original Swanepoel papers, $\alpha(\lambda)$ is simply an optical absorption coefficient. Unfortunately, some Niobium Oxide films have been found to be structurally non-uniform that leads to substantial light scattering. Formally, this effect may be taken into account by an extinction coefficient that includes both absorption and scattering of light, i.e. $\alpha_{ext} = \alpha_{abs} + \alpha_{scat}$ and thus modifying $X(\lambda)$ as

$$X(\lambda) = X_{abs}(\lambda)X_{scat}(\lambda) = \exp[-\alpha_{abs}(\lambda)d] \exp[-\alpha_{scat}(\lambda)d] \qquad (3\text{-}12)$$

To fit Equation (3.6) to experimental data, we need to choose the appropriate values of d and Δd as well as appropriate functions $n(\lambda)$, $\alpha_{abs}(\lambda)$ and $\alpha_{scat}(\lambda)$ for the refractive index,

absorption and scattering coefficient, respectively. Figure 4-22 shows that in most cases this problem is solvable within reasonable approximations that are discussed below.

There are many possible approximations for $n(\lambda)$. Among them Sellmeier or Cauchy dispersion equations are most popular [135,136]. The latter worked the best in our case in a truncated form as

$$n(\lambda) = n_0 + \frac{C_2}{\lambda^2} + \frac{C_4}{\lambda^4} \quad (3\text{-}13)$$

where n_0, C_2 and C_4 re numerical adjustable parameters. Obviously, n_0 is the limiting refractive index as the $\lambda \rightarrow \infty$.

The general theory of light scattering on spherical particles with size L was developed by Mie [137]. For small particles with $L < \lambda$, the scattering is reduced to the Rayleigh λ^{-4} law i.e. $\alpha_{\text{scat}}(\lambda) \sim \lambda^{-4}$ [138]. In the opposite case $L >> \lambda$, the approximation of geometrical optics is valid and scattering does not depend on wavelength, i.e. $\alpha_{\text{scat}}(\lambda) \sim \lambda^0$. Based on this extreme case, in present paper, we use a generalized approximation

$$\alpha_{\text{scat}}(\lambda) = \alpha_s \lambda^{-\text{m}} \quad (3\text{–}14)$$

with a_s and m being formal adjustable parameters. Parameter m varies from 0 to 4 pointing on the size of structural deformities in Niobium Oxide films that are scattering the light.

The final choice is the function $X_{\text{abs}}(\lambda) = \exp\left[-\alpha_{\text{abs}}(\lambda)d\right]$, which is made to be as flexible as possible. First, we notice that $X_{\text{abs}}(\lambda) = 0$ at small λ corresponding to strong absorption. Oppositely, $X_{\text{abs}}(\lambda) = 1$ at large λ, manifesting the absence of absorption. In the present approach we try $X_{\text{abs}}(\lambda)$ as a smooth function with smooth derivatives passing through four nodes with coordinates $(\lambda_0, 1)$, (λ_1, x_1) , (λ_2, x_2) and $(\lambda_3, 0)$. The parameters x_1 and x_2 are chosen manually around 0.8 and 0.2, respectively. The wavelengths λ_0 and λ_4 are chosen manually to guarantee the absence of optical absorption above λ_0 and strong absorption below λ_4. Overall, the model has 9 adjustable parameters d, Δd, n_0, C_2, C_4, α_s, n, λ_2, and λ_4 which in most cases (with

moderate light scattering) allow a good fit to experimental data as illustrated in chapter 4 of Figure 4-22.

The values of so-called optical bandgap for amorphous materials may substantially vary depending on methods of definition. The most popular method is Tauc rule [139] which relates optical absorption (α) and photon energy ($h\nu$) as

$$\alpha(h\nu) = B_{\text{Tauc}}(h\nu - E_{\text{Tauc}})^2 \tag{3-15}$$

where B_{Tauc} is a constant, independent of the photon energy, and E_{Tauc} is a constant called T_{auc} bandgap.

Other expressions α vs. $h\nu$ are known as Cody and Sokolov [140] relationships

$$\alpha(h\nu)^{-1} = B_{\text{Cody}}(h\nu - E_{\text{Cody}})^2 \tag{3-16}$$

$$\alpha(h\nu) = B_{\text{Sokolov}}(h\nu - E_{\text{Sokolov}})^3 \tag{3-17}$$

4. Results and Discussion

The present chapter is divided into three sections. In section 4.1 the formation of Niobium Oxide thin films by magnetron sputtering is reported. The respective thin films are characterized by XRD, Raman Spectroscopy and XPS for their structural and chemical states analyses. The surface morphology is analyzed by SEM and optical profilometer. Effect of annealing on structural properties is also analysed in this section. In Section 4.2 the physical properties including mechanical, electrical and optical properties of the deposited films is illustrated. In section 4.3 effect of V doping on structural and chemical properties of NbO_2 is presented.

4.1 Synthesis of NbO_x Thin Films by Magnetron Sputtering

4.1.1 Deposition Characteristics

As Niobium is highly reactive with oxygen and a Niobium Oxide compound is usually formed on the metallic target surface during deposition, which reduces the deposition rate. To avoid target "poisoning", a mixture of Ar and O_2 gases with a suitably designed ratio is required. Moreover, the identification of elemental and compound mode sputtering region is also required to prepare a stoichiometric or fully oxidized Niobium Oxide phases.

Figure 4-1 (a) shows the effect of oxygen gas content on the cathode (target) voltage under the conditions of constant power density of 9.87 Wcm^{-2} and total pressure of 1.08 Pa. Figure 4-1 (b) shows the dependence of the overall rate of deposition on the oxygen gas content under the same conditions.

The overall deposition rate is taken as the film thickness divided by the duration of deposition. As can be seen from Figure 4-1 (a) there is a slight hysteresis in the cathode potential vs. O_2 gas content behavior for increasing and decreasing oxygen gas

content, which is the biggest challenge for compound Niobium Oxide deposition by sputtering.

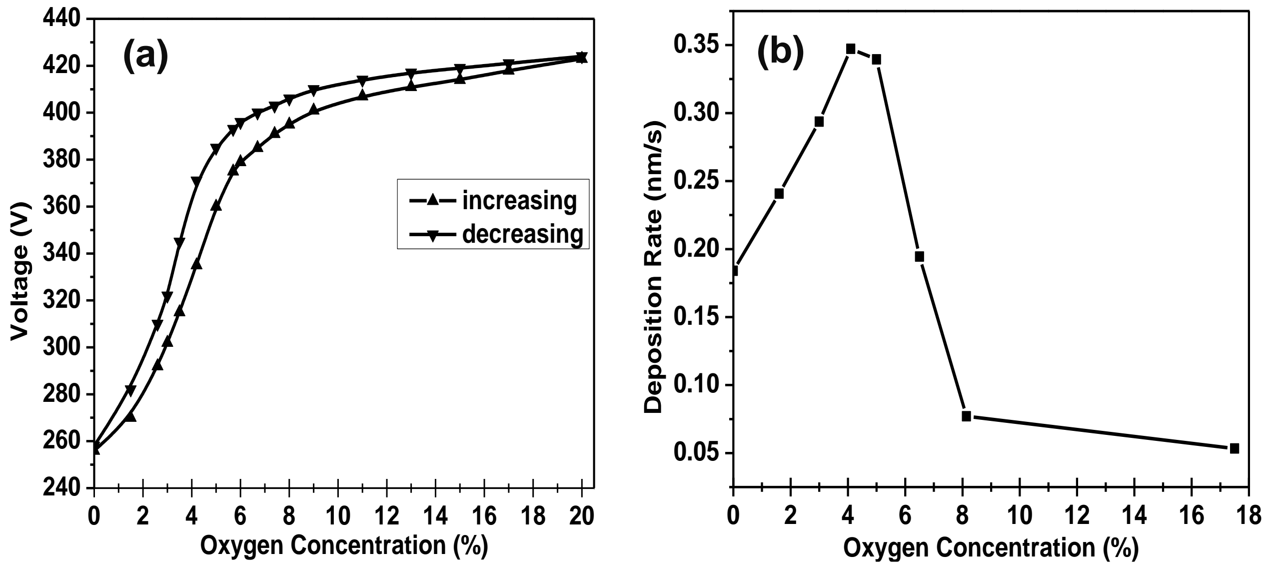

Figure 4-1: (a) variation of cathode potential of Nb metallic target and (b) deposition rate as a function of oxygen gas content

It is clear that the cathode potential increases rapidly up to 5% of oxygen gas content, which corresponds to the oxidation of the target. For oxygen gas content ratios greater than 10%, there is only a slight increase in the cathode potential with oxygen gas content. This regime represents the slow oxidization of the Nb target. For 20% oxygen gas content (not shown in Figure 4-1 (a)), there is no change in the cathode voltage, indicating that the target is fully oxidised, and the deposition is in full oxidic mode.

Thus, an oxide layer is formed on the surface of the Nb target that leads to a decrease in the sputtering yield and therefore the deposition rate decreases. The target converts to the metallic state again at lower oxygen gas content that shows the hysteresis in Figure 4-1 (a).

Figure 4-1(b) illustrates the variation of the overall deposition rate as a function of oxygen gas content inside the chamber under identical deposition conditions (The film thicknesses was measured by cross-section SEM images). The dependence of the overall deposition rate on the O_2 gas content, as expected, correlates well with rate of change (the slope) of the cathode potential vs. O_2 gas content behavior in Figure 4-1 (a).

The deposition rate increases and reaches a maximum at around 5% O_2 gas content which is the "knee" region in the cathode potential vs O_2 gas content curve in Figure 4-1 (a); and then decreases sharply. When the O_2 gas content was above 8 %, the change becomes insignificant, indicating that the samples are close to oxidized fully at 8% O_2, which is also in agreement with the cathode potential curve in Figure 4-1 (a). Higher oxygen concentrations are linked with lower sputtering yield and leads to form thinner films.

Among various deposition parameters, the oxygen gas content is the most important factor controlling the growth and morphology of sputtered films during magnetron sputtering. Nevertheless, the formation of specific NbO_x also depends on the surface condition of Nb target, power density and vacuum pressure during deposition. Depending on the oxygen gas contents, the visual color of the thin film changes, and this change can be distinguished by the naked eyes.

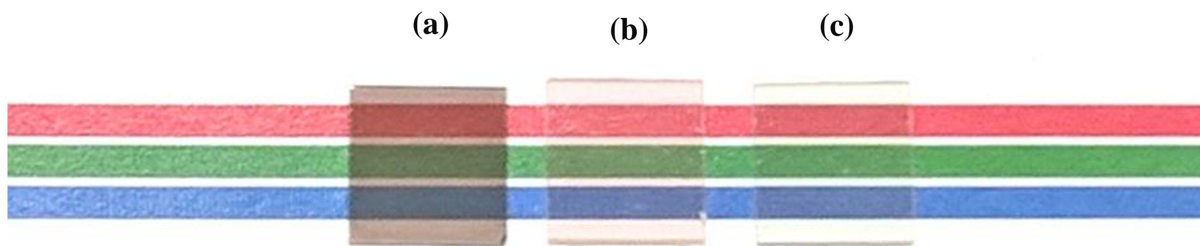

Figure 4-2: Photograph of the Samples with Thin Films of NbO_2 and Nb_2O_5 on Quartz Substrates (a) Polycrystalline NbO_2, 1.5% O_2 (b) Polycrystalline Nb_2O_5 21% O_2 (c) Amorphous Nb_2O_5 8.5% O_2 Gas Contents

The transparency and visual color of the thin films on Quartz substrate deposited under different oxygen gas contents are observed and shown in Figure 4-2 . Samples were put on a set of primary color stripes (red, green and blue) to observe the transparency. Higher oxygen gas contents show better transmittance (Figure 4-2 (b)) comparing with lower oxygen gas contents (Figure 4-2 (a)) in visible lights. It was also observed that when the oxygen gas content is 21% or above, the thin film is pink (on Quartz substrate) or yellowish (on Si substrate), and the color becomes light green for 8.5% or above oxygen gas contents.

However, when further decreasing oxygen gas contents to below 8.5% NbO_2 thin films forms and the color turns to bluish-black and black as shown in Figure 4-2(a). Actual optical

properties will be described in Section 4.2.4. The amorphous Nb_2O_5 film has very good transmittance due to large bandgap and negligible scattering. The NbO_2 and Nb_2O_5 films are not as transparent to the naked eye as the amorphous film, due to the presence of some scattering.

4.1.2 Effect of Deposition Parameters on Structural Property

4.1.2.1 Effect of Oxygen Gas contents

The Niobium Oxide exhibit several different polymorphs depending on the deposition temperature, pressure and oxygen gas content during sputtering. In our case, all deposited NbO_2 and Nb_2O_5 films show tetragonal and orthorhombic structures, respectively, as confirmed by X-ray Diffraction (XRD) results shown in Figure 4-3(a) and (b). Figure 4-3 (a) illustrates the XRD pattern of the phase-pure Body Centered Tetragonal (BCT) NbO_2 (PDF: 00-009-0235) with space group I41/a and Figure 4-3 (b) gives the XRD pattern of the orthorhombic phase of Nb_2O_5 (PDF: 01-071-0336).

The peaks with the highest intensity for the tetragonal NbO_2 and orthorhombic Nb_2O_5 are in agreement with XRD Powder Diffraction Data and those published in the literature [56,63,64,69,116,141]. Mismatch of a few lower intensity peaks might be due to the preferred orientation.

XRD results point out that the variation of oxygen concentration does not significantly affect the crystal structures when the oxygen concentrations are in the formation range of NbO_2 or Nb_2O_5. As can be seen from Figure 4-3 (a) BCT NbO_2 of high purity was formed when the oxygen gas content is from 1.5 % to 5 %.

Figure 4-3 (b) shows that films grown with 8.5% oxygen gas content and higher exhibit the orthorhombic Nb_2O_5 phase. The film grown under 6.5% oxygen gas content is primarily Nb_2O_5 but also has other phases such as NbO_2, orthorhombic $Nb_{12}O_{29}$ and monoclinicNb_2O_5.

XRD results of the samples deposited at different temperatures are explained in next section in Figure 4-7. The samples deposited below 700°C shows only one very broad peak at 25 (=2θ), indicating amorphous structure within the detection limit of XRD.

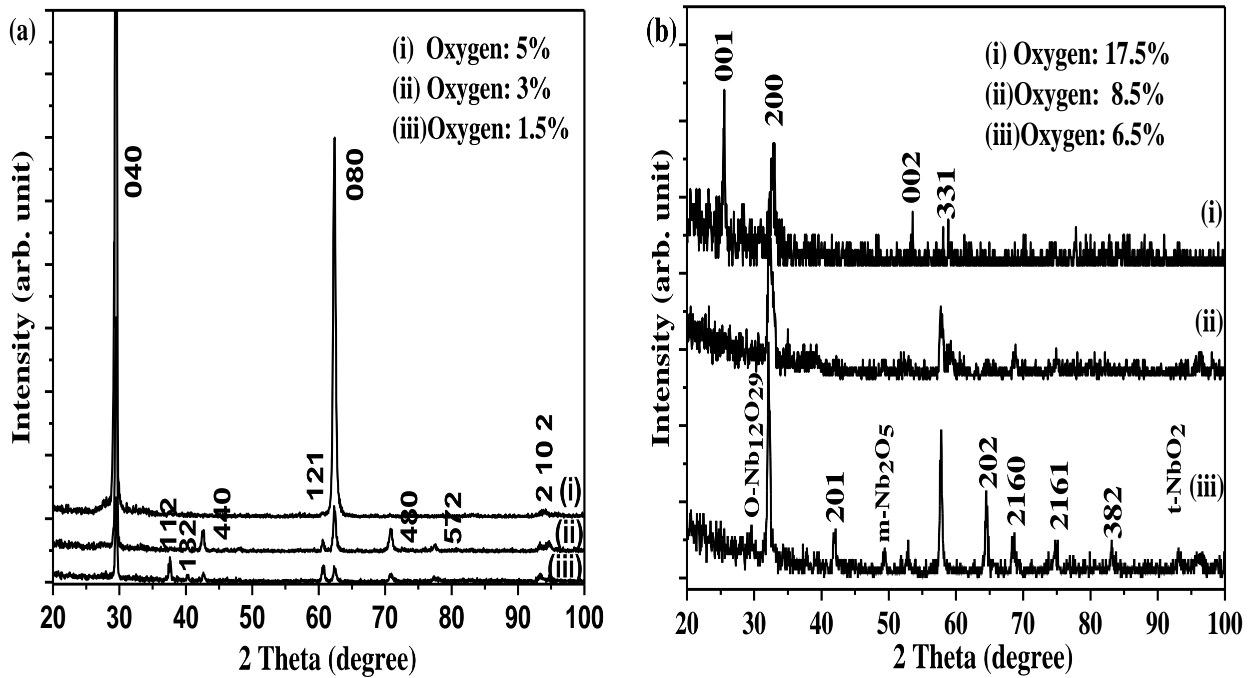

Figure 4-3: XRD Patterns of (a) NbO_2 (b) Nb_2O_5 With Different Oxygen Gas Contents

It is also observed that XRD peaks appear for samples deposited at 700°C or above but the peaks are broadened, indicating nano scale size of the grains. The peak width (FWHM) of the samples is summarized in Table 4-1.

Table 4-1: Full Width Half Maxima (FWHM) of NbO_x

XRD Peak Position (2θ)	FWHM	Sample with O_2 gas contents
29.53	0.36	NbO_2 with 1.5% O_2
37.62	0.3778	
36.77	0.001	
60.68	0.439	
62	0.45	
25.496	0.5394	Nb_2O_5 with 17.5% O_2
32.78	0.7097	

The grain sizes of the samples are estimated based on the peak width using Equation 3-1 (Scherrer equation described in section 3.4.1 assuming no stress) and the results are summarized in Table 4-2 (Note that *K*, the empirical constant, was taken as 0.89), λ is wavelength of Co source (1.78 Å), θ is the Bragg angle (diffraction angle/2) in radians and β is the full width at half maximum (FWHM) in radians. XRD peaks are fitted by a Gaussian equation to calculate the FWHM).

Table. 4-2. Crystal Size and Lattice Distortion Calculated from Bragg's Reflection

Oxygen Gas Contents	Structure	Estimate of Crystal Size (nm) [Scherrer Equation]	Estimate of Crystal Size (nm) [W-H-Ism]	Lattice Distortion (ε)
1.5%	Tetragonal NbO_2	26	31	6.1×10^{-4}
5%		23	--	--
6.5%	Orthorhombic Nb_2O_5	21	15	--
8.5%		12	--	--
17.5%		16	14	2.6×10^{-3}

However, the films are actually stressed, and we can assume that the strain present in NbO_2 and Nb_2O_5 is isotropic. In this case we can use the Williamson-Hall-Isotropic Strain Model (WH-ISM) shown in Equation 3-2 [123,124], to estimate the grain size of the samples. The estimated results are also summarized in Table 4-2. Crystalline calculated by these two methods are very close and the W-H analyses results are probably more accurate for crystalline size estimation. Nevertheless, both methods are not appropriate to be used to estimate the size of the grains with anisotropic shape. It should be noted that the obtained grain size can be equal or smaller than the actual grain size as the stacking faults, dislocations and instrumental errors were not considered while calculating the FWHM.

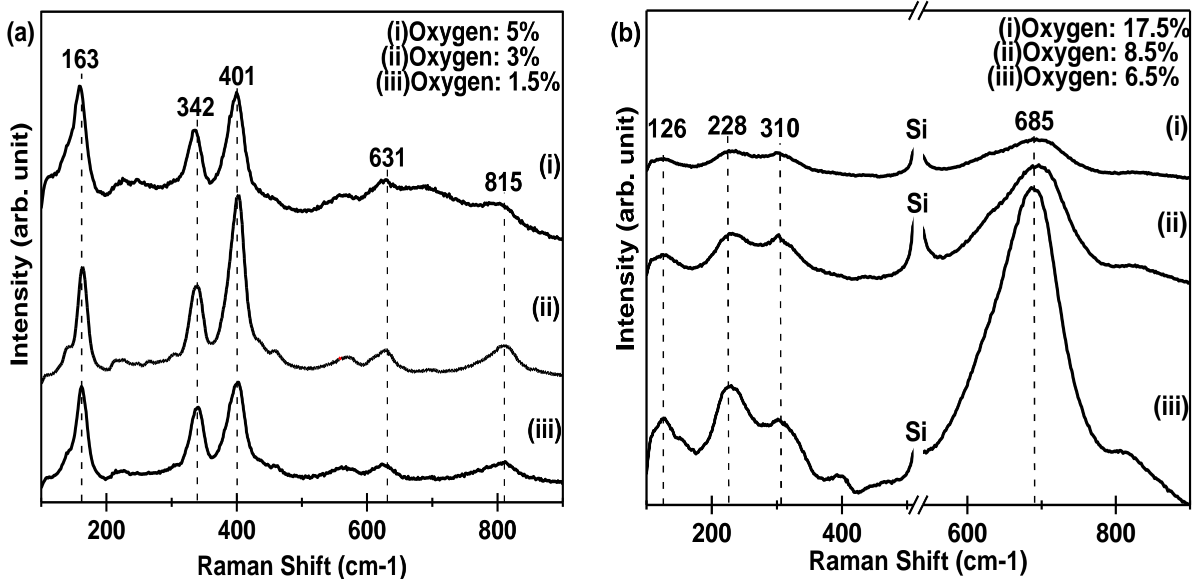

Figure 4-4: Raman spectrum of (a) NbO_2 and (b) Nb_2O_5 With Different Oxygen Gas Content

The XRD results reveal the nanostructure of the thin films. Raman spectroscopic studies have been carried out to complement with the XRD results. Typical Raman spectra of these nanostructured NbO_2 and Nb_2O_5 thin films are illustrated in Figure 4-4. The Raman shift at 163 cm^{-1}, 247 cm^{-1} , 342 cm^{-1}, 401 cm^{-1}, 631 cm^{-1} and 815 cm^{-1} are for tetragonal NbO_2 [56,63,64]. And, the Raman shift at 126 cm^{-1}, 228 cm^{-1}, 310 cm^{-1}, 685cm^{-1} are for Nb_2O_5 [69,116,141], whereas ~228 cm^{-1} and ~310 cm^{-1} are for tetragonal Nb_2O_5 phase [116] and ~685 cm^{-1} can also be assigned for low distorted NbO_6 octahedral coordination [116]. These Raman results are in good agreement with the XRD data for the phase identifications. At about 5% oxygen gas content, there is a small and broad peak emerging at ~685 cm^{-1} that probably corresponds to Nb_2O_5. No notable shifts in the Raman spectrum are observed for Nb_2O_5, while the intensity difference is attributed to different film thickness.

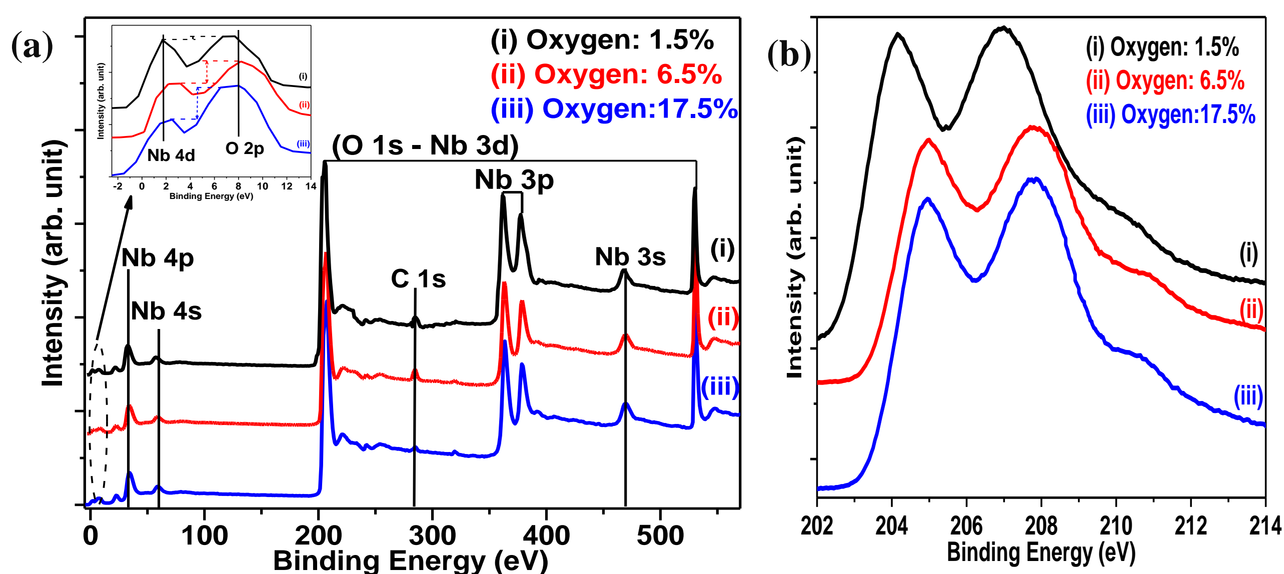

Figure 4-5: (a) XPS Survey Scan of the NbO_x Thin Films with Inset of Nb 4d and O 2p Peaks and (b) High Resolution XPS of Nb 3d Doublets

Oxidation state and stoichiometric composition of the Niobium Oxides are further corroborated by XPS measurements. Survey scans with a wide range of binding energy was taken in multiple points before and after impurities removal by Ar sputtering. Typical survey scans of Niobium Oxide s after Ar sputtering and the high resolution Nb 3d spectrum for 17.5%, 6.5% and 1.5% oxygen gas contents are presented in Figure 4-5(a) and Figure 4-5(b) respectively. Inset of Figure 4-5 (a) presents the relative altitudes of Nb 4d and O 2p peaks. Binding energy in the range of -3eV to 580eV is presented and the characteristic peaks are denoted as O 1s, C 1s, Nb 3s, Nb 3p, Nb 3d, Nb 4s and Nb 4p. Atomic gas contents can be

calculated from the area and sensitivity factor of Nb 3d (Relative Sensitivity Factor, RSF= 2.92) and O 1s (RSF= 0.78) peaks. The highly surface sensitive survey scan shows the O/Nb ratio over 2.8 before Ar sputtering that indicates the surface as over oxidised. After Ar cleaning, the O/Nb ratio displays 1.85, 2.25 and 2.32 for 1.5%, 6.5% and 17.5% oxygen gas contents respectively.

Relative peak positions of Nb 3d line shape for these oxygen gas contents are shown in Figure 4-5 (b). Even though there are not any significant discrepancies among the line shapes of these 3 samples, relative peak positions and intensities have slight differences. Peak position of the Nb 3d doublets can ascribe the thin films as NbO_2 and Nb_2O_5 according to reference standards [61,142,143]. Slight shift of binding energies are due to Ar sputtering in surface which is consistent with M. Kang et.al [143]. For the same reason the 3d doublets show comparable shapes for different oxygen gas contents. Negligible shoulder in Figure 4-5 (b) (ii) and Figure 4-5 (b) (iii) can be attributed as Nb_2O_5, however, standard Nb 3d core level peak shape for NbO_2 is still unresolved in literatures.

Difference of Δ(O─ Nb) is a more stable parameter for describing the electrical properties of Niobium Oxides as the variations of Δ(O─Nb) depend on O─Nb bonding [142]. Oxidation of Niobium leads to alteration of Nb 3d binding energy to higher energy level and O 1s binding energy to lower energy level. Therefore, less difference in Δ (O─Nb) B.E attributes to more oxidation of Niobium. Energy differences of Δ (O 1s − Nb 3d) observed in Figure 4-5 (i), (ii) and (iii) are 325 eV, 323.3 eV and 323 eV that can be assigned as NbO_2, Nb_2O_5 and Nb_2O_5 respectively [142].

In addition, the valance band ratio, ratio of maximum height of Nb 4d to maximum height of O 2p, can also be utilised for determination of Nb oxidation state. Fully oxidised Nb has typically broader O 2p peak with very insignificant Nb 4d peak whereas the metallic Nb show sharp Nb 4d peak. Relative differences of valance band ratio in inset of Figure 4-5 (a) signify the oxidation states of the thin films.

Similarly, the XPS survey scan of amorphous samples, deposited at room temperature, show the NbO_2 and Nb_2O_5 chemical structures for similar oxygen gas contents. High Resolution Nb3d doublet in Figure 4-6 (after Ar cleaning) also confirms the same.

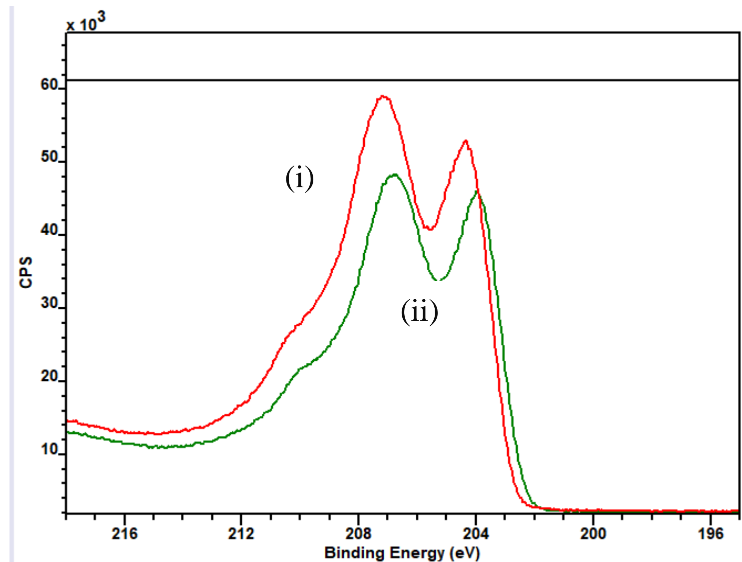

Figure 4-6: Nb 3d doublet of amorphous (i) Nb_2O_5 and (ii) NbO_2

4.1.2.2 Effect of Substrate Temperature

Effect of substrate temperatures on the structural properties are investigated systematically and the XRD results are presented in Figure 4-7.

The deposition temperature is very crucial for forming amorphous or crystal structures. It was found that below 700°C (XRD with Cu source), the as deposited films on Si (100) were amorphous (illustrated in Figure 4-7). The XRD and Raman spectra showed the amorphous structures of Niobium Oxide thin films for deposition temperatures from 25 °C up to 650 °C.

XPS results confirmed the NbO_2 or Nb_2O_5 structures depending on the oxygen gas content (shown in Figure 4-6). Deposition temperature also affects the surface morphology of the thin films. The surface of the thin films prepared at lower deposition temperature was smoother whereas the films deposited at higher temperatures were rougher. For the Si (100) substrate, a very high temperature is required for the films to be crystalized.

Figure 4-8 shows the effects of deposition temperature and oxygen concentration (film thickness) on the surface roughness of Niobium Oxide films measured by optical profilometer.

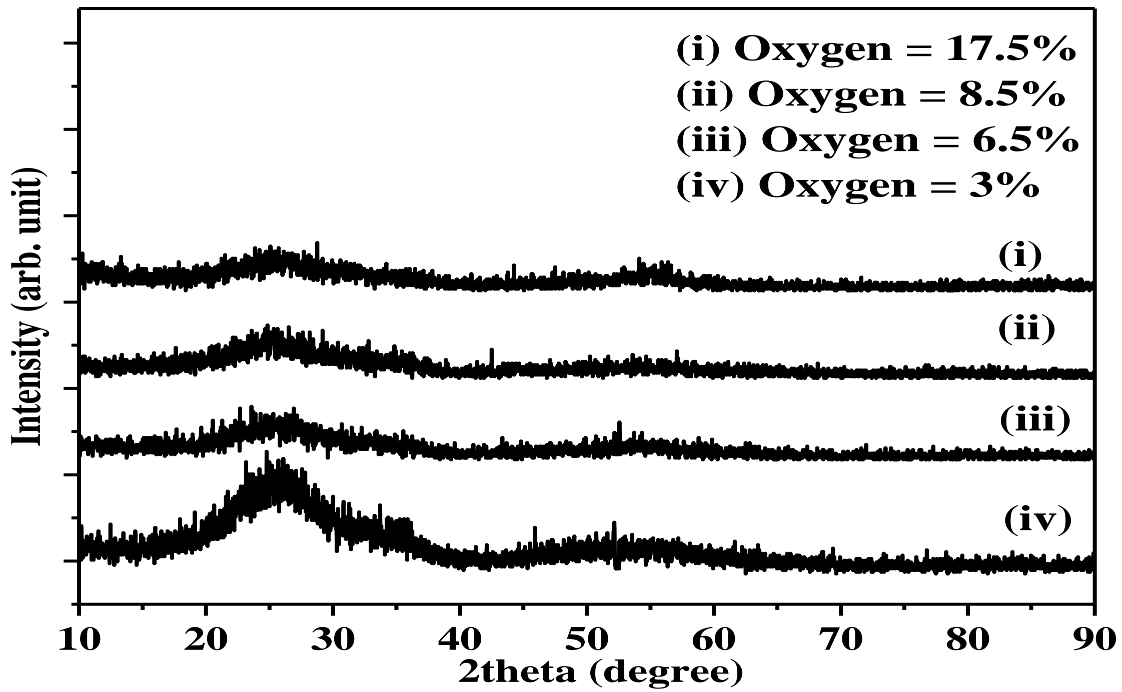

Figure 4-7: GIXRD of NbO_x with Different Oxygen Gas Contents Deposited At 650°C

It is visible that the films are smooth with a roughness less than 1.4 nm at deposition temperature of 650°C or bellow. Crystal growth at higher temperature leads to increased surface roughness.

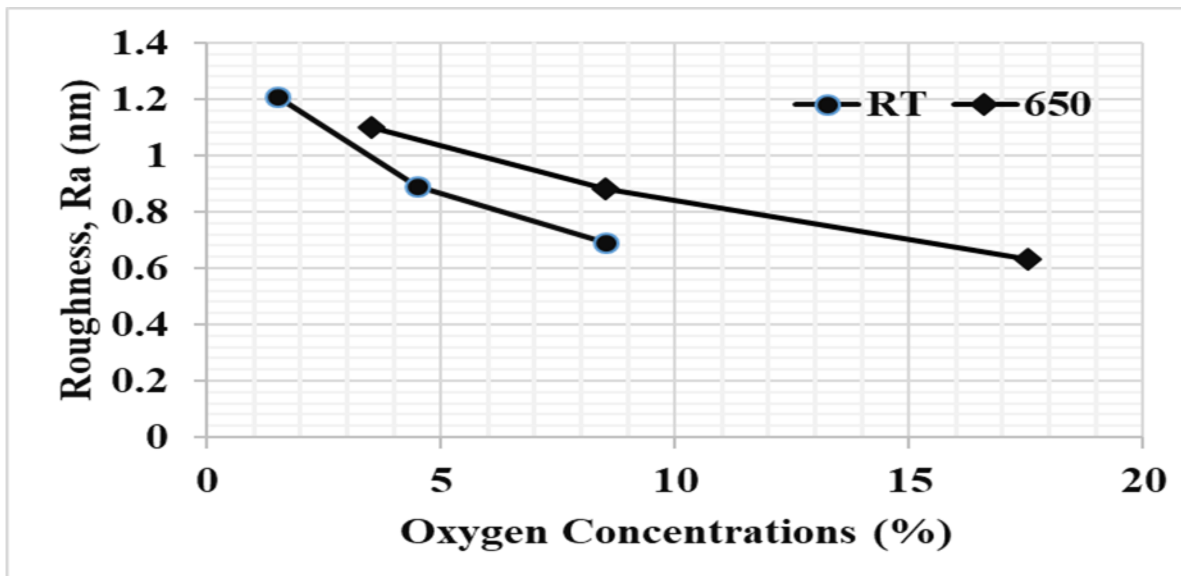

Figure 4-8: Variation of Surface Roughness for Different Temperature with Similar Thickness

Diffusion of oxygen in Niobium can be explained by the diffusion coefficient D,

$$D = \text{f}\ \mathbf{exp}\ (-\frac{26910}{\text{R}T}) \quad (4\text{-}1)$$

where, f is frequency factor and the value are fixed (0.0212 cm^2s^{-1}); T is the temperature in kelvin, R is ideal gas constant (1.987 $calK^{-1}mol^{-1}$).

Diffusion length of oxygen in Niobium increases for increasing temperature and time. For fixed 2hrs deposition time the deposition length is equal to 0.33Å and 270 μm respectively for room temperature and 720 °C deposition temperature. Substrate temperature affects the diffusion rate as well as the nuclei size that eventually distresses the microstructure of films. Higher deposition temperature and lower deposition rate help to form single crystal or large grained polycrystalline films.

Effect of temperature on the grain size can be explained by the following Arrhenius relationship presented in Equation (4-2)

$$K = ln(k_0) + (-\frac{Q}{RT}) \quad (4\text{-}2)$$

where, Q is the activation energy for grain growth, and it can be estimated by measuring the grain growth rate k of the average grain size at different temperatures. The term k_0 is a constant, R is the universal gas constant and T is the Temperature in Kelvin.

4.1.2.3 Effect of Total Gas Pressure

In order to assess the possible effect of total gas pressure during deposition on film structures, Raman Spectroscopy and X-ray Diffraction were performed on the Nb_2O_5 and NbO_2 samples with constant Oxygen gas contents. The results presented on Figure 4-9 confirm that film structures and composition were affected by deposition pressure for NbO_2 samples.

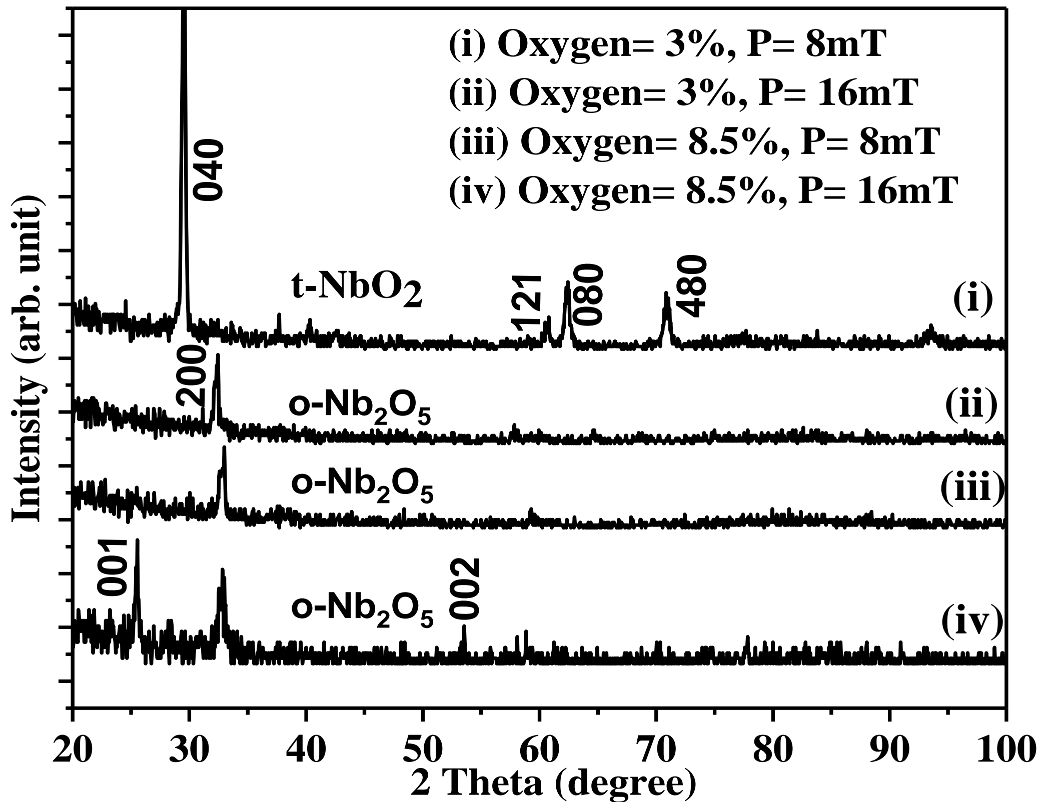

Figure 4-9: XRD of NbO_x with Different Deposition Pressure

A change in deposition pressure, from 8 mtorr to 16 mtorr, had a big difference in composition. Increase of deposition pressure basically increases the partial pressure of oxygen (ratio of oxygen pressure to total pressure in deposition chamber), leading to the formation of Nb_2O_5 instead of NbO_2 at 3% oxygen content. Whereas at 8.5% oxygen concentration, Nb_2O_5 forms at 8 mtorr. As Nb_2O_5 is a stable phase, increasing pressure to 16 mT does not change the phase composition of the thin film.

Nevertheless, the surface roughness increases with the increase of deposition pressure, as shown in Figure 4-10.

As is revealed by the Figure 4-9 and Figure 4-10, NbO_x films prove variation in structures and surface roughness within the investigated pressure range. The investigations were carried out for the pressure variations from 7 mtorr to 16 mtorr. Nb_2O_5 forms instead of NbO_2 while increasing the total deposition pressure. At 16mtorr, NbO_2 disappears and pure Nb_2O_5 forms.

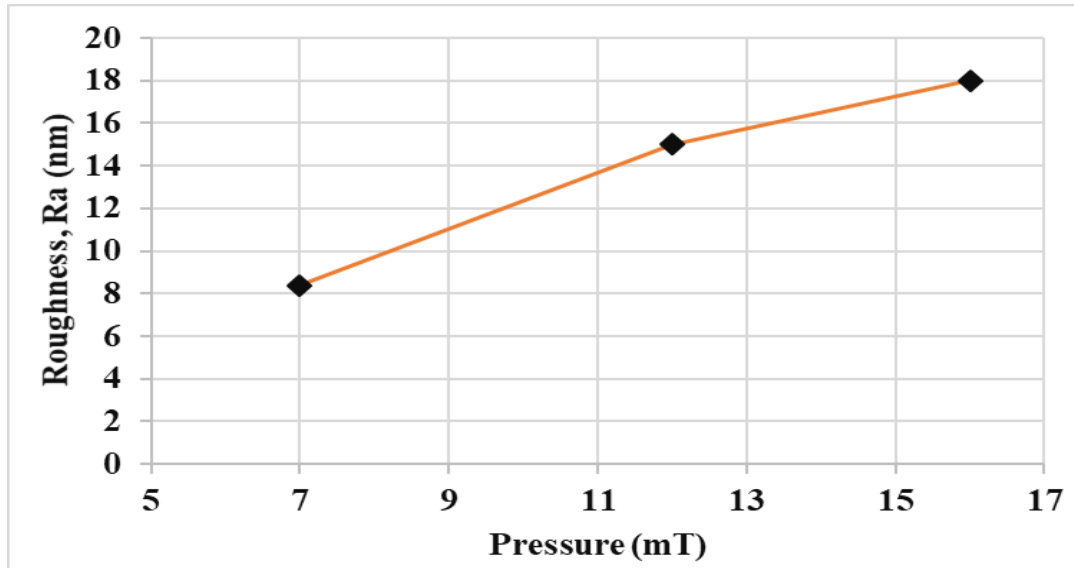

Figure 4-10: Effect of Deposition Pressure on Surface Roughness

The mean free path $\boldsymbol{\lambda}$ of gas atoms is affected by the deposition pressure which can be expressed by the following equations:

$$\lambda = \frac{K_{\mathrm{b}}T}{\sqrt{2}\ \pi d^{2}P} \tag{4-3}$$

where, K_{b}, T, d, P denotes Boltzmann constant, deposition temperature (fixed at 720°C), diameter of gas atoms, deposition pressure respectively.

The distance between substrate and target was kept constant (45mm) which was higher than the mean free path value. When the pressure was increased the mean free path, value decreased and therefore there were collisions between the oxygen and Niobium atoms. Eventually, there was less unreacted Niobium atoms when the pressure was higher.

Surface roughness usually depends on many factors. When keeping all other deposition parameters, the same but increasing the gas pressure from 7 mtorr (0.933 Pa) to 16 mtorr (2.13 Pa), film roughness (Ra) increases from 8.4 nm to 18 nm.

This can be explained by the mean free path. At lower deposition pressure the mean free path is supposed to be extended and a lesser amount of collisions occur among particles drifting from target to substrate.

Therefore, target atoms lose less energy and thus reach at the substrate with higher kinetic energy that helps to form smoother and denser films. On contrary, at higher deposition pressure rough films are produced because of the lower energy of the depositing atoms.

4.1.3 Effect of Post Annealing

Metallic Niobium and as deposited Niobium Oxide s are being annealed at different temperatures and their structural properties are evaluated consequently.

4.1.3.1 Annealing Nb Thin Films

The XRD results of the samples annealed at high temperatures are shown in Fig. 4-11 and Fig. 4-12.

For lower temperature annealing, the film consists of a mixture of different phases of Niobium Oxide. At 700°C or above, the Nb_2O_5 phase is dominated and the thickness of Nb thin films affects the preferred orientation of the resulted Nb_2O_5 phase.

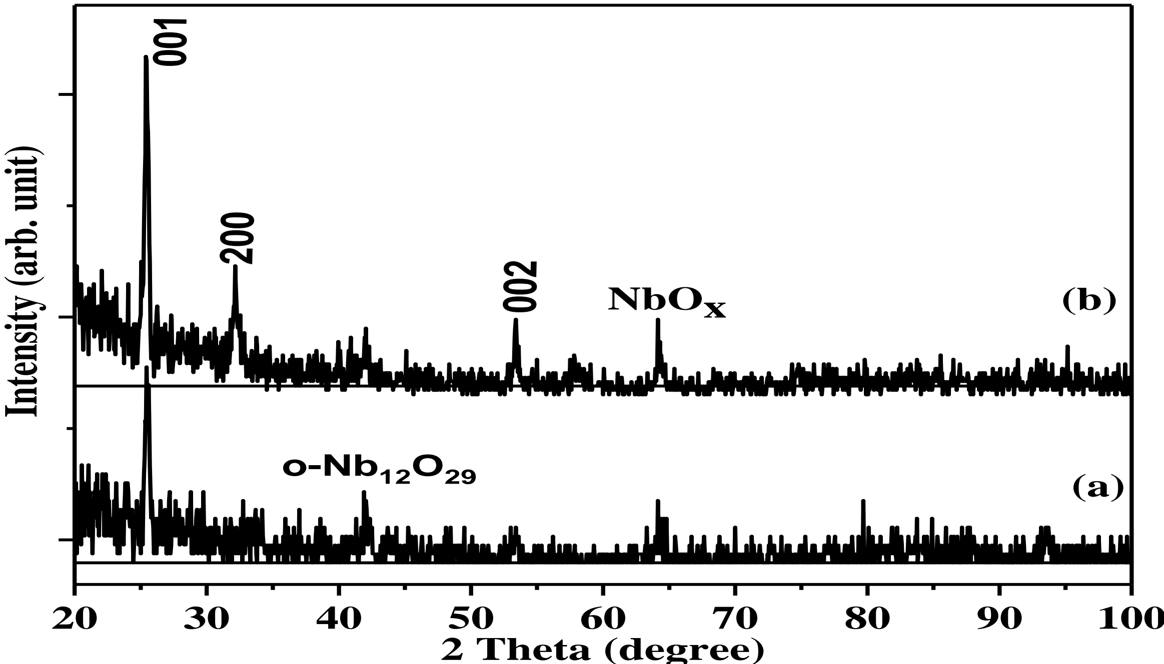

Figure 4-11: Annealed Nb (Thickness~500 nm) at 700°C for (a) 2hrs and (b) 4hrs Respectively, Major Peaks are from O-Nb_2O_5.

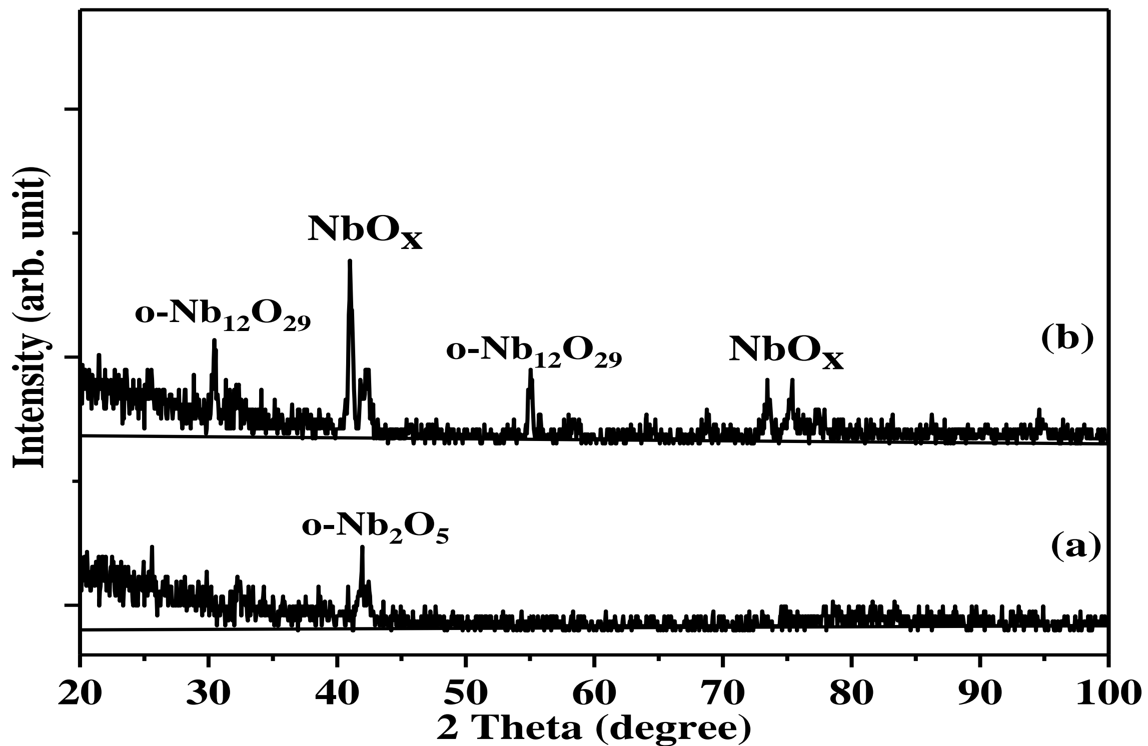

Figure 4-12: Annealed Nb (thickness~1µm) at 700°C for (a) 2hrs and (b) 20hrs respectively.

Nevertheless, the Nb_2O_5 thin films formed by this process are not phase pure, they consist of a small amount of a few other oxide phases, as revealed by the Raman spectra shown in Figure 4-13.

It can be clearly seen that in addition to the peaks for Nb_2O_5, there are a few peaks appeared, which cannot be identified as known phases of NbO_x. Further research needs to be done in order to understand the structure and properties of those new metastable phases.

The Raman spectra for annealed sample are shown in Figure 4-13. It can be seen clearly that a mixture of different phases is presented in the annealed thin films, in which a few peaks cannot be identified based on the known phases of NbO_x. Metastable new phases might form and further research needs to be done to understand the structure and properties of the new phases.

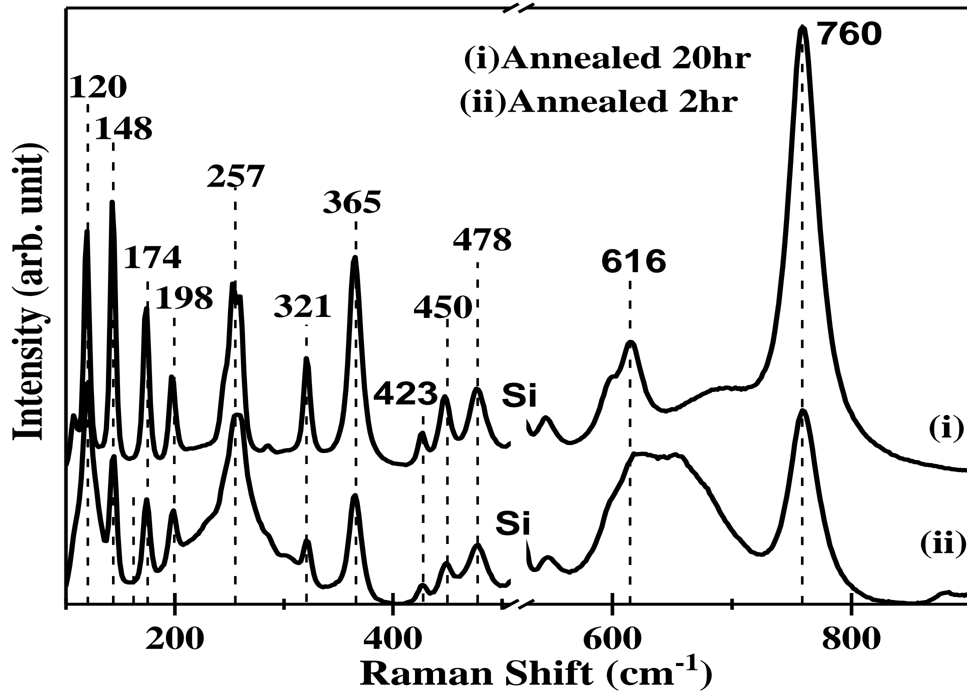

Figure 4-13: Raman Spectra of Annealed Nb Thin Films at 700°C

4.1.3.2 Annealing NbO_2 in Ar Atmosphere

The XRD results of the treated NbO_2 samples in Ar atmosphere are shown in Fig 4-13. The samples were annealed for different durations from 10 mins to 2 hrs. Two of the samples are presented here. It is observed in the Fig 4-14 (a) and Fig 4-14 (b) that structure of the films is similar regardless of the annealing duration. It should be noted that many peaks cannot be identified based on the known phases of NbO_x. Further research needs to be done in order to understand the structure and properties of the new phases. Moreover, there are so many XRD peaks for each of the NbO_x and few of them overlaps with different structures.

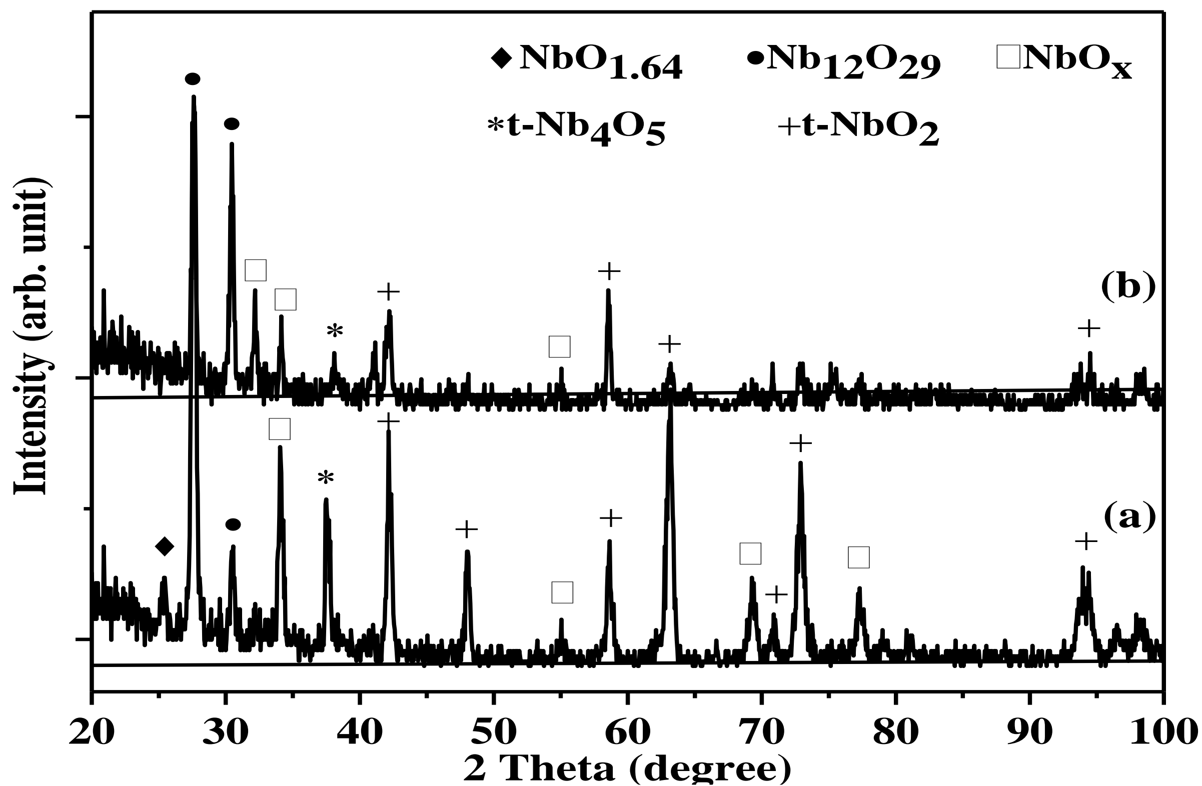

Figure 4-14: XRD of Annealed NbO_2 Thin Films- (a) Annealed at 700°C for 10 min (b) Annealed at 700°C for 2 hr

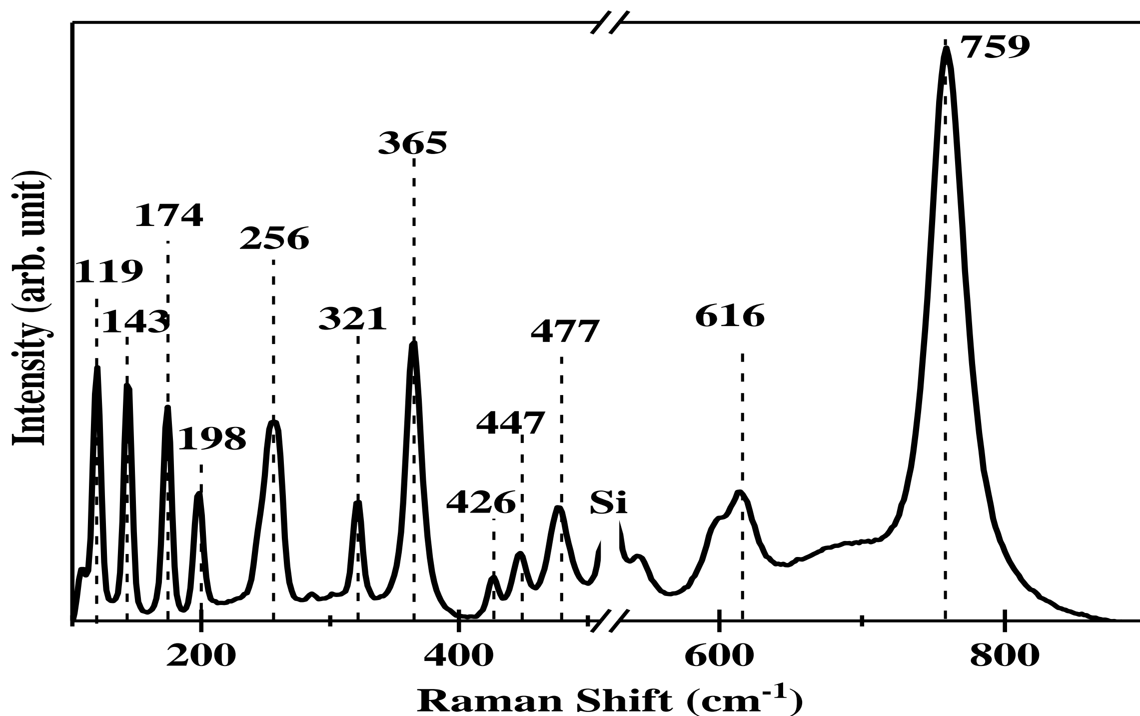

Figure 4-15: Raman Spectra of the Annealed NbO_2 Thin Films at 700°C for 10 min

Raman spectra of one of the annealed NbO_2 samples are shown in Figure 4-15. A few of the peaks signifies NbO_2 structure (174 cm^{-1} and 612 cm^{-1}) and a few of them signifies Nb_2O_5 structures (119 cm^{-1}, 321 cm^{-1}, 447 cm^{-1}) as shown in the figure (shifted few orders). However, most of them (143cm^{-1}, 198 cm^{-1}, 256 cm^{-1}, 365 cm^{-1}, 477 cm^{-1}, 759 cm^{-1}) are yet to identify since the Raman shifts of NbO_x phases are not well studied yet. Therefore, further research is inevitable on the structural properties of different Niobium Oxides.

4.1.3.3 Annealing Amorphous Nb_2O_5 in Ar Atmosphere

Figure 4-16 shows that the XRD patterns of phase pure tetragonal NbO_2 has been achieved by annealing Nb_2O_5 at Ar pressure in the range of 4 MPa to 8 MPa. The Grazing Incidence X-ray Diffraction (GIXRD) results (with Cu target) of the treated samples are illustrated in Figure 4-16.

The results confirm the tetragonal NbO_2 structure of the thin film. However, there is a slight difference in the preferred orientation of the thin film comparing with the as-deposited NbO_2. The Nb_2O_5 samples used to for annealing were deposited Si (100) substrate using RF 150W and 15% oxygen gas contents and confirmed to be amorphous using XRD.

It starts to crystallize after annealing at 550°C. Nucleation starts on the surface because of higher oxygen contents and higher density of defects on the surface.

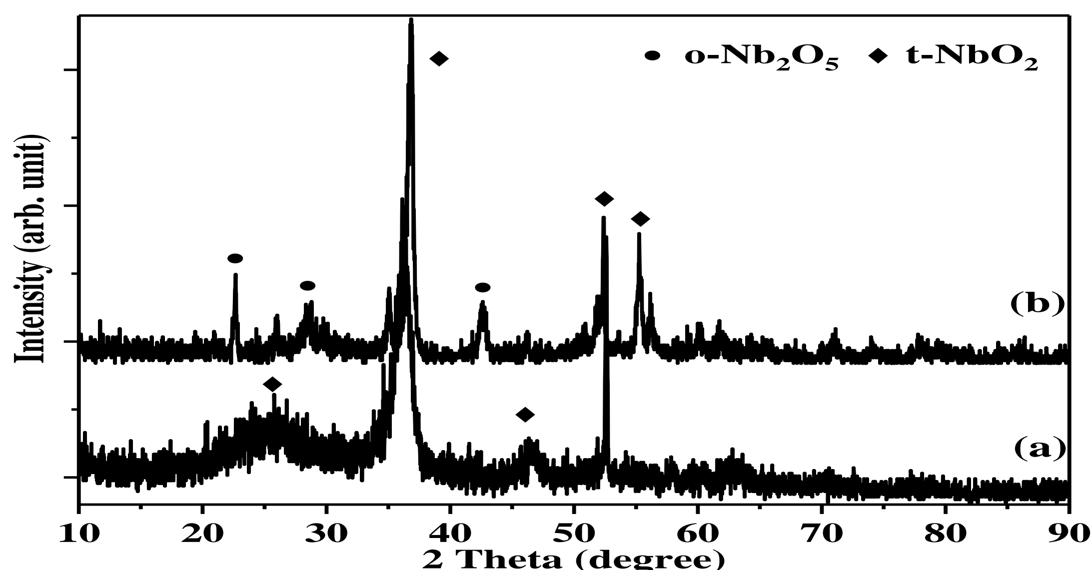

Figure 4-16: Annealed a-Nb_2O_5 thin films (a) for 2hrs (b) for 4 hrs

After 2 hr annealing, the diffraction peaks are broadened (nano crystal) as shown in Figure 4-16(a) and the average grain size is in nanoscale. When increasing annealing duration to 4 hrs, the samples show good crystallinity with increased grain size (sharp beak) as shown in Figure 4-16 (b).

Raman spectra of these samples are presented in Figure 4-17. These spectra confirm the films are of pure tetragonal NbO_2 structure. Both of the samples have similar tetragonal structures, however, annealing with longer durations shifts the Raman peaks to lower values.

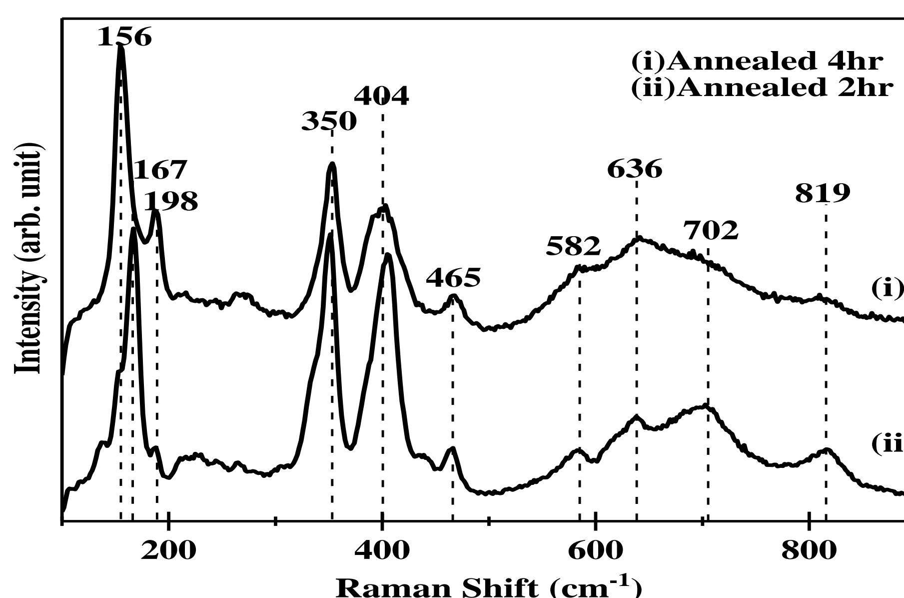

Figure 4-17: Raman Spectra of Annealed a-Nb_2O_5 Thin Films

4.2 Surface Morphology and Physical Properties of Niobium Oxides

4.2.1 Surface Morphology

Figure 4-18 illustrates typical SEM images of crystalline NbO_2 and Nb_2O_5, respectively. The top-view images are show in Figure 4-18(a-d) and the cross-sectional images are shown in Figure 4-18 (b) &(e)). NbO_2 shows nano slice structure while Nb_2O_5 shows two different kinds spongy structures (Figure 4-18(d) and (f)).

NbO_2 with 1.5% oxygen gas content shows multiple orientations whereas NbO_2 with 5% oxygen gas contents have roughly two orientations which are in agreement with XRD peaks. The Nb_2O_5 samples show different structures for 17.5% and 6.5% oxygen gas contents, respectively. For 17.5% oxygen gas contents the growth of crystals is visible as like flower blooming whereas for 6.5% oxygen gas contents flakes are fully-fledged in different directions.

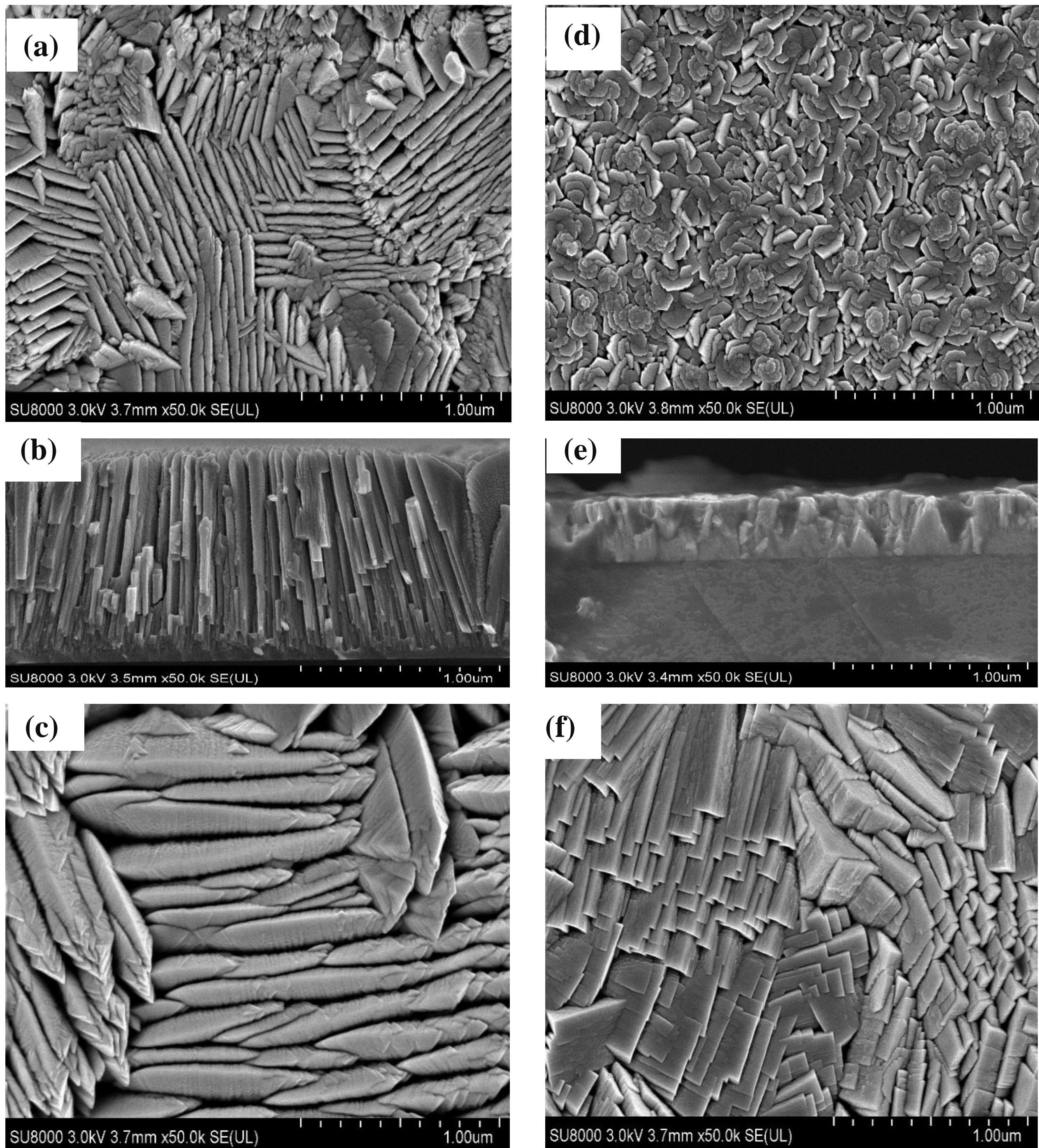

Figure 4-18: SEM surface and cross-section micrographs of NbO_2 (a, b, c) and Nb_2O_5 (d, e, f)

The nano slice structure of the NbO_2 with an approximate length of 100nm-1000nm were reported previously [60,144]. These nano slices could be aligned or randomly (thermally grown) accumulated [60]. These two alignments may be due to surface diffusion during sputtering caused by disproportionate kinetic energies. On the contrary, the Nb_2O_5 films show flakelike surface morphology which ascribes to crystallization at high temperature. It also refers to a brittle structure having high elastic modulus as expected for metal oxides. Its structure is different from that previous reported structures [134–138] . SEM analyses of these thin films are done at different spots and it is found that the structure of the films is uniform throughout the sample surface.

Figure 4-19 shows the effects of deposition temperature and film thickness on the surface roughness of Niobium Oxide films measured by optical profilometer. It is obvious that the films are smooth with a roughness of ~ 1 nm while deposited at 650 °C.

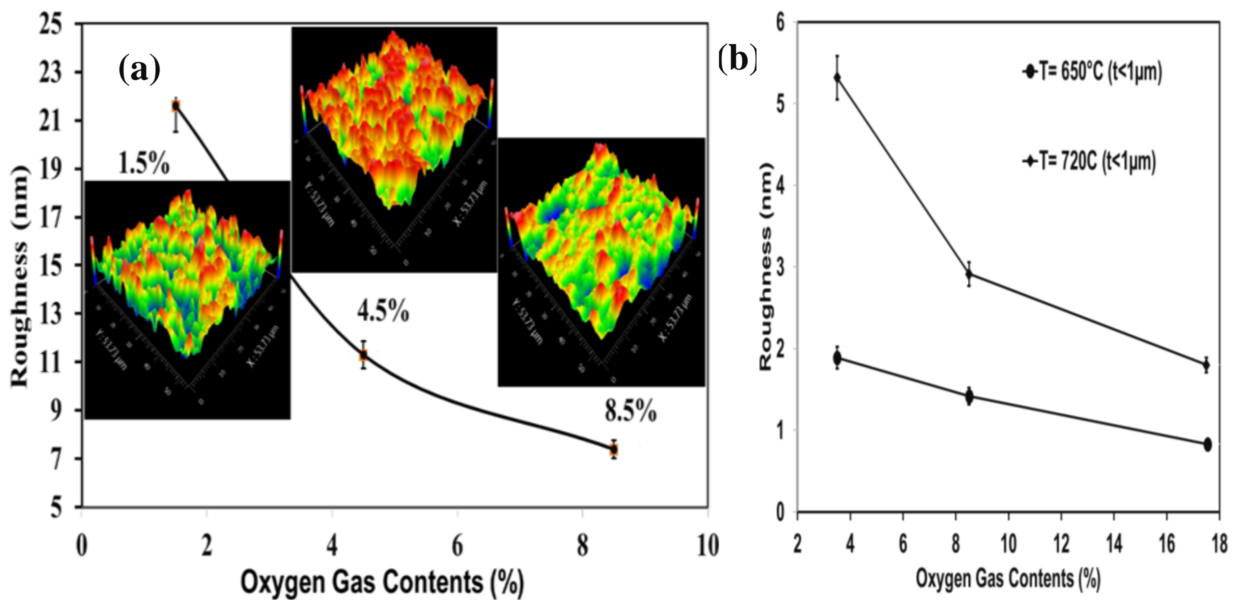

Figure 4-19: Surface roughness (Ra) of (a) thick (t > 2 μm) and (b) thin (t < 1μm) samples with two different deposition temperature.

Oxygen gas content has negligible effect for amorphous thin films which is consistent with the results reported by Ali Foroughi et al. [147]. However, oxygen gas content for crystal samples with higher thickness (above 2 μm) have impact on the surface roughness. It can be concluded that higher deposition rate, higher deposition pressure, higher thickness and higher crystallinity leads to increased surface roughness.

The surface morphology of the NbO_2 thin films, observed by SEM, changes after annealing at 700°C for 2 hours in Ar atmosphere. The structure becomes denser as illustrated in Figure 4-20. The Nano slice structure is disappeared, and mixture of different phases appear.

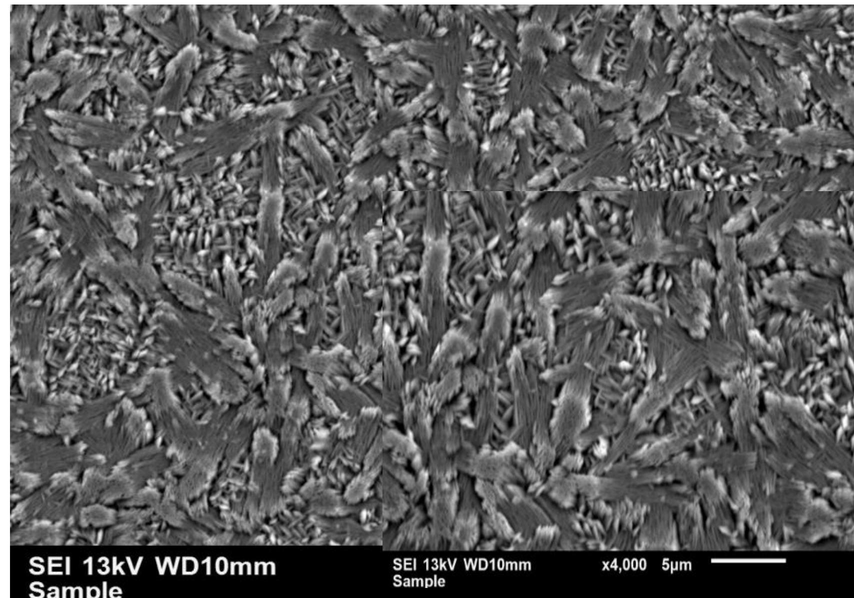

Figure 4-20: SEM Surface Micrograph of Annealed NbO_2.

4.2.2 Mechanical Properties

4.2.2.1 Total Stress

Residual stress of the films are presented in Figure 4-21. Stress is generated in a thin film during the deposition; the substrate is thick and has negligible stress. Excessive stress can cause cracking, deformation and delamination of film that makes the device practically unusable.

The total stress of thin films determined by the Stony Equation (3-3) is shown Figure 4-20. The residual stress for both NbO_2 and Nb_2O_5 are compressive, and the values are 107 ± 15 MPa to 375 ± 20 MPa, respectively, where the stated errors have been determined from multiple measurements. At higher deposition temperatures, the residual stress becomes lower. Nix et al [148] have shown that the average stress decreases with increasing grain size which is supportive in our case, comparing the grain sizes of NbO_2 and Nb_2O_5 films.

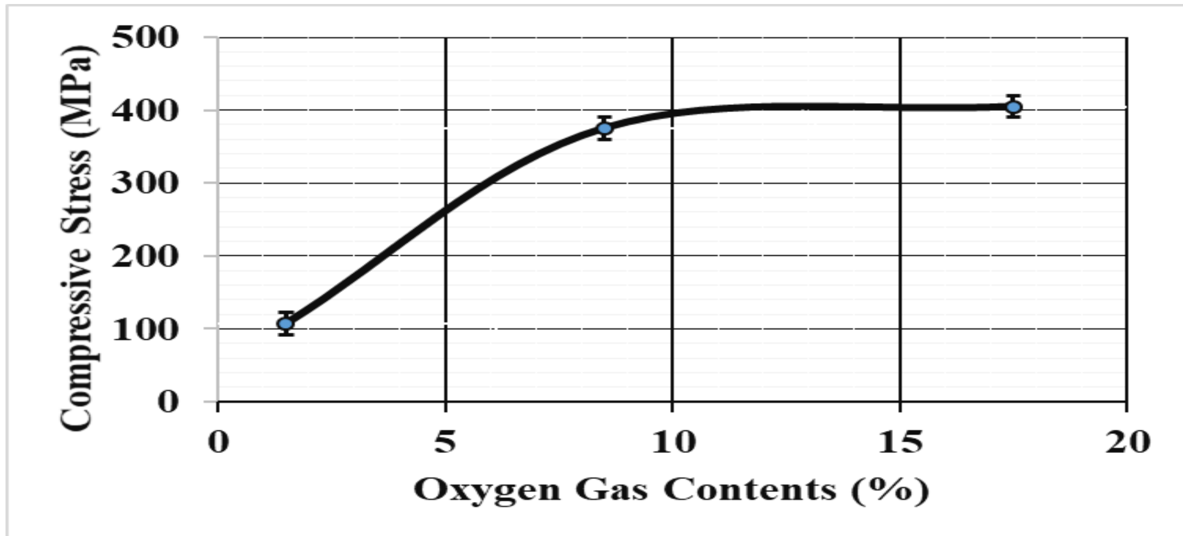

Figure 4-21: Residual Stress for Different Oxygen Gas contents

The beam bending formula is the basic principle of this method in which the deposition of the film modifies the substrate curvature. The stress of sputtered thin films usually depends on the mobility of the depositing atoms and becomes compressive due to densification of impinged atoms. The total stress of metal oxide thin films does not solely depend on oxygen gas content, and it is also influenced by film density, surface roughness and film thickness. According to previously reported data, the average residual stress of niobium oxide is usually compressive and it is below 480 MPa [149], which is consistent with the present results. However, the residual stress can be tensile for films annealed at high temperature [150]. In our case, the residual stress for both NbO_2 and Nb_2O_5 are compressive, as shown in Figure 4-21, and the values are 107 ± 15 MPa to 375 ± 20 MPa respectively, where the stated errors have been determined from multiple measurements. At higher deposition temperatures, the residual stress becomes lower. Nix et al [148] have shown that the average stress decreases with increasing grain size which is supportive in our case, comparing the grain sizes of NbO_2 and Nb_2O_5 films.

4.2.2.2 Hardness and Young's Modulus

The nanohardness and Young's modulus of NbO_2 thin films are shown in Table 4-3. is 5.8 GPa to 6.0 GPa. There is no readily available direct comparison with any previous work on NbO_2 thin films. The nanohardness of Nb_2O_5 thin films, as shown in Table 4-3. is 5.3 GPa to 13.5 GPa, which is in agreement with the reported nanohardness of Nb_2O_5 thin films [151].

These hardness values of thin films mostly depend on deposition methods and process parameters. Although, in general, it is difficult to correlate the oxygen gas content with mechanical properties such as hardness and Young's modulus, nonetheless, the higher oxygen gas content during deposition leads to more homogenous surface and better mechanical properties. Due to thinness of the coatings, the penetration depths in this work were below 15% to 20% of the thickness, even though widely used rule of thumb restricts the penetration depth to less than 10% of film thickness for soft films [152].

In this work, the error due to the substrate is negligible as the samples all have similar thicknesses and all have been deposited on the same substrate [151], and the surface roughness is negligibly small compared with the thickness. Different surface topography and roughness can also affect the hardness of thin films. The highest hardness (13 GPa) was exhibited by the Nb_2O_5 thin film deposited under an oxygen gas content of 21.5%. This Nb_2O_5sample shows similar orthorhombic structure. Its high hardness, which is very close to that of bulk Nb_2O_5, is probably attributed to its densely packed structure.

Table 4-3: Evolution of Mechanical Properties of NbO_x.

Oxygen Gas Content (%)	**Sample**	**Hardness (GPa)**	**Young's Modulus (GPa)**
1.50%	NbO_2	5.8 ± 1.2	146 ± 8
3.0 %		6.0 ± 1.0	
8.50%	Nb_2O_5	5.3 ± 1.2	137 ± 6
21.50%		13± 1.2	157 ± 6

4.2.3 Electrical Properties

Electrical conductivity is a property that is well knowing to show large variation among various material systems. It depends on the concentration of carriers and their drift mobility. In the case of NbO_x films in this work, unlike mechanical properties, electrical conductivity is highly dependent on the oxygen gas content. The conductivities observed are more than those of amorphous NbO_x oxides [153]. The conductivity values are smaller than typical metal values and are in the range of typical heavily doped semiconductors.

Conductivity decreases in one order while increasing oxygen gas content to 8.5%. Nb_2O_5 with 17.5% oxygen gas content is insulator like and the values are out of range in the four-point probe measurement. Dense surface structure and larger crystallite sizes of NbO_2 shows higher conductivity comparing with their Nb_2O_5 counterparts. These samples are deposited on p-type Si (100) substrates which have very high conductivity (conductivity more than 1 S-m). Therefore, the conductivity values are less reliable due to the effect of the substrates. To overcome the substrate effect, the samples were coated with two thin Au layer of electrodes with distance of 0.5mm. The slope of the electric field (ε) vs current density(j) curve reveals the conductivity of the samples. The measurements were conducted by electrometer and the conductivity of the samples are in the range of 110 S-m to 170 S-m. The samples also show threshold electrical switching at higher voltages (5 to 10V). Because of the pinhole of the coatings the effect of the substrate is not completely overcome. Therefore, to get more reliable data non conductive substrate is more preferable.

4.2.4 Optical Properties

The optical and structural properties of Niobium Oxide films are summarized in Table 4-4. Concentration of oxygen in reaction chamber during deposition seems to play the major role in properties of Niobium Oxide films. Films with higher oxygen concentration prone to be higher oxides Nb_2O_5 while lower oxygen concentration leads to NbO_2 formation.

Higher oxygen films seem to be more optically uniform with small or undetectable light scattering. Figure 4-22 shows reasonable agreement with model predictions for all samples excluding the sample with the lowest concentration of oxygen (1.5%) where the scattering was so severe that the model failed completely. However, even in the best samples the power in scattering expression ($\alpha_{scat}(\lambda) = a_s\lambda^{-m}$) was substantially lower than 4 pointing on scattering on objects (possibly microcrystals) with typical sizes larger than the wavelength.

Amorphization of Nb_2O_5 at 8.5% of oxygen leads to theoretically predicted increase of optical band gap (E_g) and reduction of optical density of the film (n_0) [154].

Table 4-4: Influence of Structure and Oxygen Concentration on Optical Properties of Niobium Oxide Films.

Structure	Oxygen Gas Content (%)	n_0	E_g (eV)	Scattering Intensity and m
c-Nb_2O_5	17.5	2.19	3.30	weak (m = 0.52)
c-Nb_2O_5	8.5	2.11	3.30	undetectable
a-Nb_2O_5	8.5	1.92	3.30(Sokolov) 3.43(Cody) 3.53(Tauc)	weak (m = 0.51)
c-NbO_2	3.5	2.20	3.40	strong (m = 1.4)
c-NbO_2	1.5	-	-	very strong

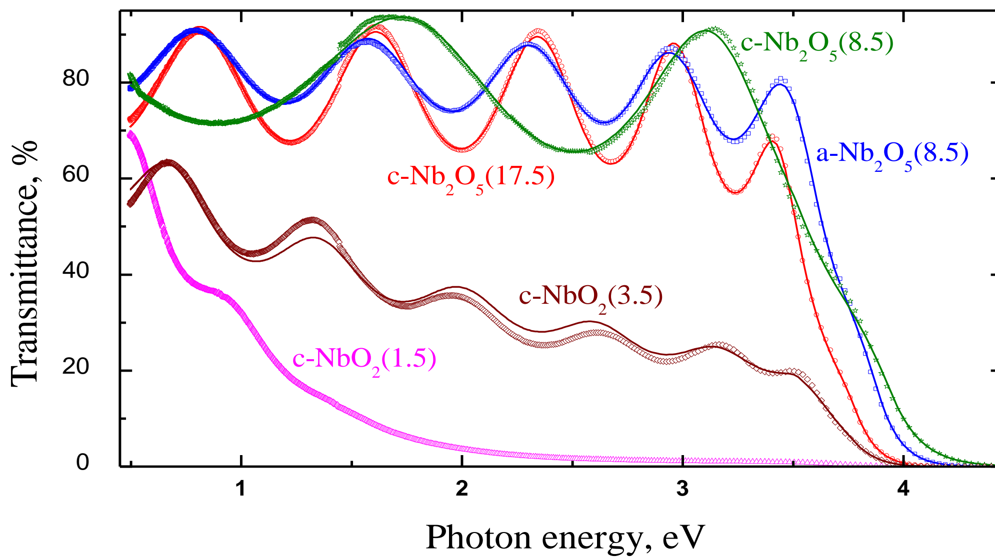

Figure 4-22: Optical Transmittance of Niobium Oxide Films. Points are Experimental Data. Lines are Results of Calculations Using the Model Described in Paper. No Fit could be Achieved for Sample c-NbO_2 (1.5). Explanation of Notation: “c-” Stands for Crystalline and “a-” for Amorphous Samples, Number in Brackets are Oxygen Concentrations (in %).

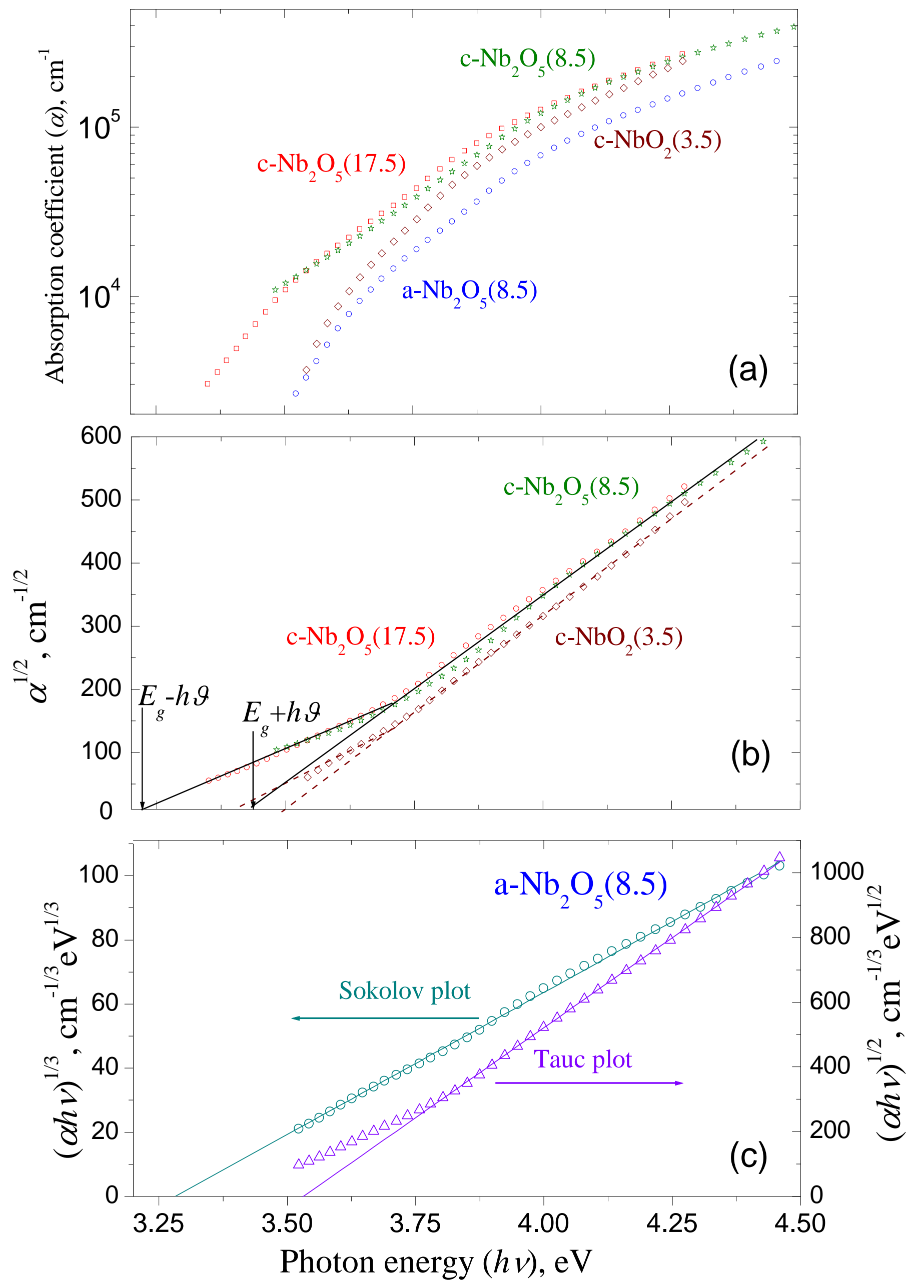

Figure 4-23: Optical Absorption Coefficient in Niobium Oxide Films. (a) Semi logarithmic Presentation, (b) Tauc's Presentation. Notations are the Same as in Figure 4-22.

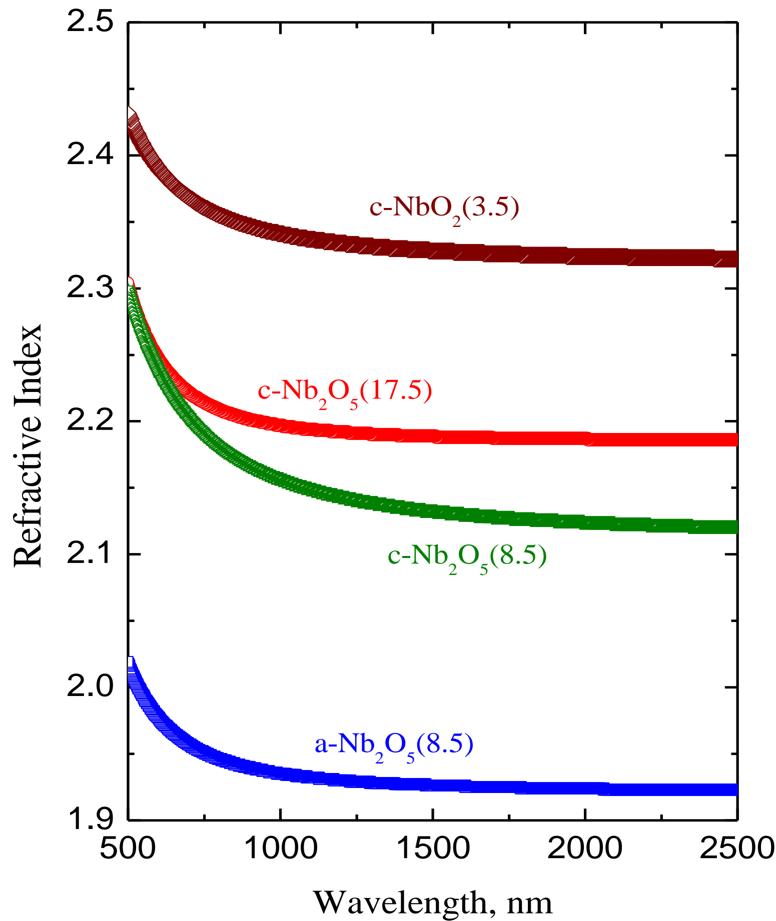

Figure 4-24: Refractive Index of Niobium Oxide Films. Notations are the same as in Figure 4-22.

When the fitting is done, α_{abs} (λ) or rather α_{abs} ($h\nu$) is calculated. The dependence of the absorption coefficient as a function of photon energy is presented in Figure 4-23(a). Figure 4-23(b) is the usual square root of $\alpha h\nu$ vs. $h\nu$ plot from which one can extract the bandgap based on the T_{auc} rule [139]. The dependence of the absorption coefficient as a function of photon energy is presented in Figure 4-23(a). Further derivation of optical band gap uses different approaches for crystalline and amorphous materials.

The Figure 4-23(b) shows the determination of optical gap E_g in crystalline Nb_2O_5 which is known to be an indirect gap semiconductor where the optical absorption is accompanied with absorption or emission of a phonon [151]. As a result the optical absorption

may be presented as a sum of two processes corresponding to phonon absorption and phonon emission [136].

$$\alpha_{\text{absorption}} = A[f_{\text{BE}}(h\vartheta)][h\nu - (E_g - h\vartheta)]^2 \; ; \; h\nu > (E_g - h\vartheta), \tag{4-4}$$

And

$$\alpha_{\text{emission}} = A\,[1 - f_{\text{BE}}(h\vartheta)][h\nu - (E_g + h\vartheta)]^2 \; ; \; h\nu > (E_g + h\vartheta), \tag{4-5}$$

Here, E_g is optical bandgap, A is a constant, $h\vartheta$ is phonon energy, $f_{\text{BE}}(h\vartheta)$ is the Bose-Einstein distribution function at the phonon energy $h\vartheta$, i.e. $f_{\text{BE}}(h\vartheta) = [(\exp(h\vartheta/k_BT) - 1]^{-1}$, where k_B is the Boltzmann constant and T is the temperature. The sum of (4-4) and (4-5) will give two straight lines in $\alpha^{1/2}$ vs. $h\nu$ coordinates with onsets at $(E_g - h\vartheta)$ and $(E_g + h\vartheta)$ as shown in Figure 4-23(b). E_g is obviously the average between these two onsets. The values of E_g are close 2.30 eV and are shown in Table 4-4.

The best fitting using Tauc relation is shown in Figure 4-23(c) and the value of E_{Tauc} = 3.53 eV is obtained. Both of the Cody and Sokolov relationships give better results than T_{auc} relation, and Sokolov expression gives the best near perfect fit which is shown in Figure 4-23 (c) with the value of E_{Sokolov} = 3.28 eV.

The structural variations due to different oxygen gas contents play important role in the optical properties of Niobium Oxide films. Films with high oxygen gas content seem to be more optically uniform with small or undetectable light scattering.

Figure 4-22 shows reasonable agreement with model predictions for all samples excluding the sample with the lowest oxygen gas contents (1.5%) where the scattering was so severe that the model failed completely. Even for the sample with 3.5% oxygen gas contents the scattering is so strong (m=1.4) that scattering on objects is larger than the wavelength.

We assume that it may be connected with non-uniformity of structure. Once oxygen gas content is high enough to form Nb_2O_5, further increasing oxygen level will not affect the optical properties of the films (Figure 4-23 (a), (b)). Amorphization of Nb_2O_5 at 8.5% of oxygen gas content leads to theoretically predicted increase of optical band gap (E_g) and reduction of optical density of the film (n_0) [154].

Based on XRD and Raman results, decreasing oxygen gas content to 3.5% and below leads to the formation of high purity NbO_2. The information on NbO_2 is scarce however it seems to have indirect E_g around 0.7 eV and direct E_g around 1.3 eV [53] that is well below our results shown in Table 4-4.

In our opinion this controversy may be related to the non-uniformity of the film which may consist of mixture of NbO_2 and Nb_2O_5 oxides with Nb_2O_5 forming "transparency windows" defining measured optical properties. This model would explain also strong scattering of light observed in low oxygen films. It is worth noting that similar results with similar explanation were obtained earlier [147].

4.3 V doped NbO_2 films

In this section Nb rich $V_xNb_{1-x}O_2$ films with different V concentrations and their structural and optical properties are explored subsequently.

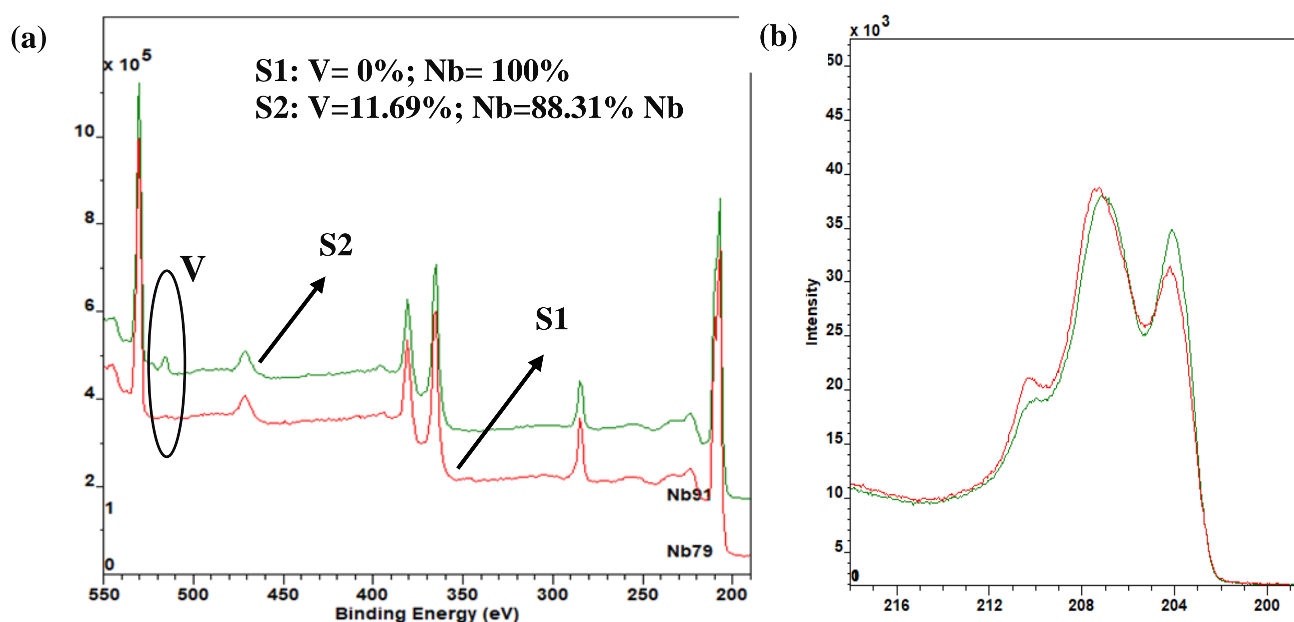

Figure 4-25: (a) Survey XPS Data (b) Nb 3d Spectra of V Doped NbO_2 Thin Films for (S1) 80W and (S2) 100W Sputtering Power of V.

Figure 4-25 shows the XPS survey spectra and Nb 3d spectra of V doped tetragonal NbO_2 thin films. No vanadium was detected in the samples deposited at V sputtering power of 80 W (S1), indicating that 80 W might below the V sputtering threshold, whereas Vanadium is

noticeable when the sputtering power of vanadium target was 100 W (S2), consistence with the XRD results where structural variations were observed due to the doping of V.

The composition for S2 estimated based on the survey XPS is close to $NbV_{0.1}O_{2.1}$. The High resolution Nb 3d spectra further confirms that there is a slight variation in stoichiometry of these two samples. S1 sample oxidises more comparing with S2. These slight oxidation variations would be due to the sputtering power difference of V target.

Figure 4-26 and figure 4-27 display the XRD results and Raman spectra of tetragonal NbO_2 doped with different amount of V, respectively. The X-ray diffraction peaks for S1 are identical with those of tetragonal NbO_2, indicating no other phases related to VO_x present in the film.

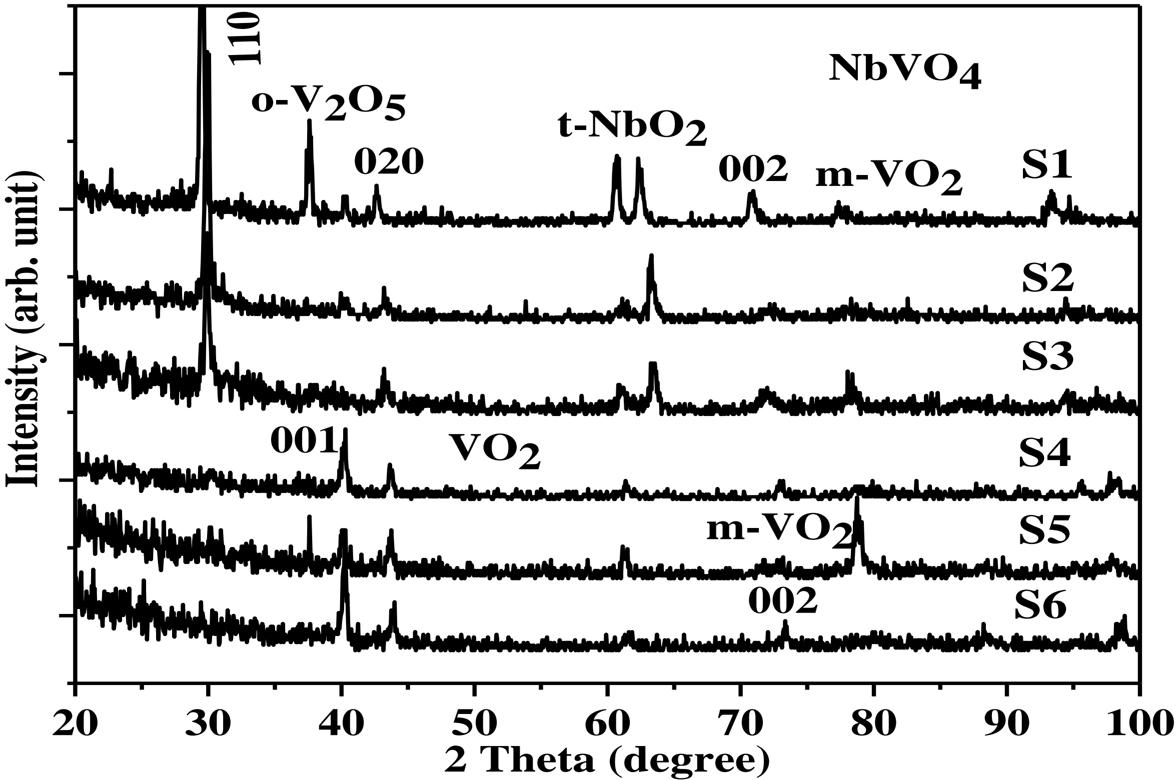

Figure 4-26: X-ray Diffraction of V Doped NbO_2

For sample S2 and S3 with higher amount of doped V, the peaks are shifted to higher angles and the higher the doping mount, the larger the shift. These results suggest that the doped V replaces Nb forming solid solution.

We know that V ions are smaller than Nb ions and the lattice parameters become smaller when Nb ions are replaced by V ions, which causes diffraction peaks shift to higher angles. Within the solubility limit, the higher the doped amount, the larger the shift. However, when the doped amount over the solubility limit, second phase or more phases form. This is the case for sample S4, S5, and S6. It has been seen that VO_x phases in addition to $Nb_xV_{1-x}O_2$ appear for sample S4, S5, and S6.

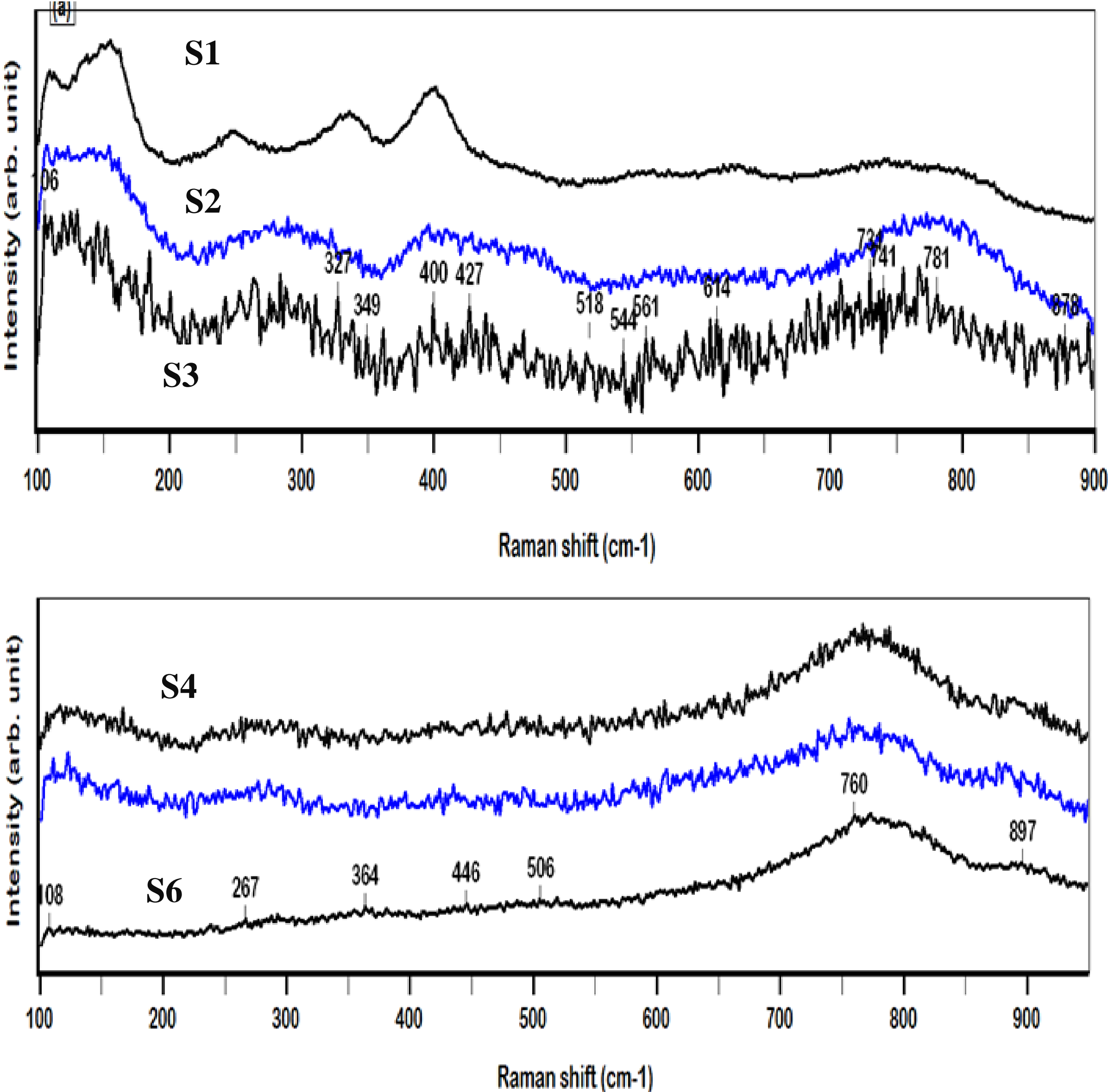

Figure 4-27: Raman Spectra of V Doped NbO_2 Thin Films with Different V Contents

The Raman spectra shown in Figure 4-27 confirm the results from XRD where for S1, the peaks are similar to NbO_2, those peaks disappear when the doped V over a certain amount. We know that both NbO_2 and VO_2 have distorted rutile structures with MO_6 octahedra.

Low Raman bands from 100 cm^{-1} to 250 cm^{-1} refer to V ion signals and high Raman bands from 600 cm^{-1} to 800 cm^{-1}) can be assigned as the symmetric extending mode of the basal oxygen ions within the VO_6 octahedra [155, 156]. The reported Raman spectra for NbO_2 have similar structure with VO_2 [157, 158] where low frequency bands are associated with Nb-Nb motions. V substitution detaches Nb-Nb bonds by destructing these two Raman bands. The lattice alteration of tetragonal NbO_2 declines with the rise of V contents and therefore, transition from distorted rutile to rutile lattice may occur while increasing V gas contents in the alloy.

For NbO_2, Raman bands at high frequencies are associated with internal modes of NbO_6 octahedra [159] because of the large binding forces. Nb-O band stretching is sensitive to the collation and this Nb-O stretching frequencies (700 cm^{-1} to 1000 cm^{-1}) are related to the length of Nb-O bands in edge sharing NbO_6. Raman bands at 342 and 401 cm^{-1} of NbO_2 are linked to diverse bending modes of Nb-O vibration within NbO_6 octahedra.

Therefore, peak shifts due to V substitutions can be the result of variations of metal-

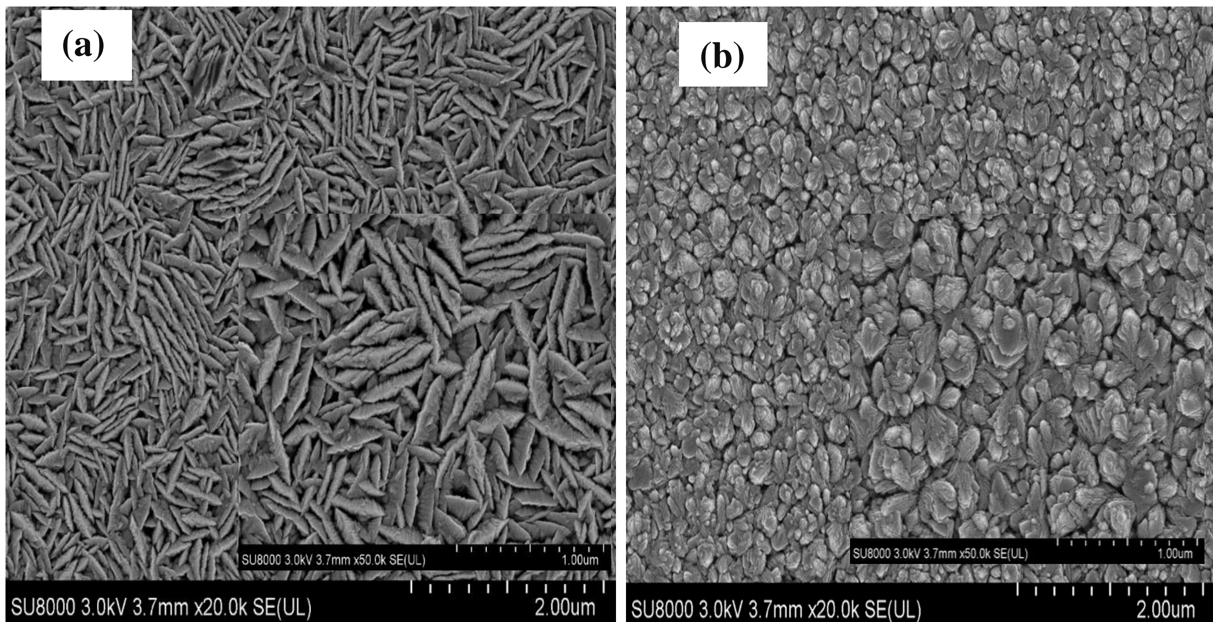

Figure 4-28: SEM micrographs of V doped NbO_2 for sample (a) S2 and (b) S4

oxygen bond lengths or change of inter atomic force factors prompted by V replacements.

Figure 4-28 shows the SEM surface images of the NbO_2 thin films doped with different amount of V. Up to 11% V concentrations the surface shows nanoslice structure and similar roughness as pure NbO_2. And the slices become denser due to V doping as illustrated in Figure 4-28 (a). It can be inferred that those thin films with low amount of doped V still uphold similar distorted rutile structure. However, for high amount V doping, the surface exhibits Nano granular morphology (Figure 4-28 (b)) like that of pure VO_2 thin films. This change of morphology is probably due to the formation of new phases as shown by XRD and Raman results

In summary, the results from XRD, Raman spectra and SEM surface morphology observation show that the addition of V to NbO_2 dislocates the Nb-Nb bonds. Increasing V contents attenuates lattice distortion that ultimately terminate the tetragonal structure of NbO_2.

The optical transmittances of the samples deposited on double side polished Si (100) substrate are illustrated in Figure 4-29. Although the big difference of V doping level in sample S2 and S6, their optical transmittance is similar, indicating that the V doping has little influence on the transmittance of NbO_2. Actually, high level of V doping (S6) makes the film more transparent in wavelengths ranging from 1000 nm to 2100 nm) than low level V doping (S2).

The transmittance of Si substrate is near zero at or below 1000 nm wavelength, therefore the transmittance of the samples are zero at those regions. The doped thin films are transparent in the infrared region that is helpful for IR wireless data transmission and the V doping makes

the film more electrically conductive.

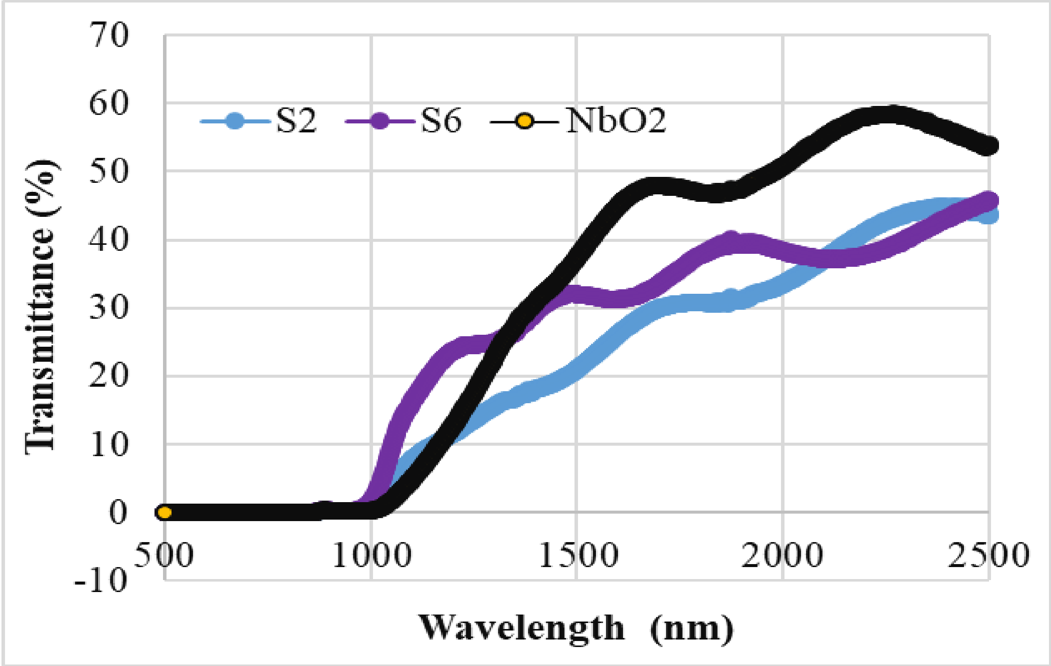

Figure 4-29: Optical Transmittance of sample S2, S3 and NbO_2 deposited on Si substrate

5. Summary, Conclusions and Future Works

5.1 Summary and Conclusions

NbO_x and V doped NbO_x thin films were prepared on Si (100) and Quartz substrates by reactive magnetron sputtering under different conditions and characterized using different advanced methods including XRD, Raman, XPS, SEM, and Spectrophotometer. The results and conclusions are summarized as follows:

1. The effect of influential deposition variables including oxygen concentration in the chamber, operation pressure, and deposition temperature on film structure and properties has been investigated and phase pure NbO_2 and Nb_2O_5 films have been successfully achieved. It has been observed that the deposition rate decreases significantly in the transition region for the formation of NbO_2 to Nb_2O_5. XRD, Raman spectra, and XPS analyses confirmed that tetragonal NbO_2 thin films form when the oxygen gas concentration is less than 5 %) and orthorhombic Nb_2O_5 films form when the oxygen gas concentration is higher than > 6.5%. Furthermore, a substrate temperature above 700°C under an appropriate operation pressure (8 to 10 mtorr) is required for obtaining high quality Niobium Oxide thin films with well crystallized structure.
2. The effect of annealing as-deposited NbO_x and metallic Nb thin films on the structure of the films has also been investigated. A mixture of different phases of NbO_x including new phases have been found in the annealed samples that requires further investigations.
3. The effect of V doping on the structure and properties NbO_2 samples has also been studied. The results show that V doping breaks the Nb-Nb bonding of NbO_2 and creates a new bonding in the structure and thus changes the optical transmittance of the films.
4. SEM studies illustrate two distinct surface morphologies of NbO_2 and Nb_2O_5 and V doping changes the morphologies of NbO_2.

5. The mechanical, electrical, and optical properties of films have been measured. All the films exhibit compressive residual stress. The nanohardness and Young's modulus values of NbO_2 films area approximately 6 GPa, and 146 GPa, respectively whereas the Nb_2O_5 films exhibit a nanohardness 5.3 to 13 GPa and a Young's modulus of 137-158 GPa depending on the processing conditions. The electrical conductivity of all the films were high in the rage of 10^4 S m^{-1}. The refractive index at a photon energy of 2 eV (620 nm) is approximately 2.38 for NbO_2 and 2.21 for Nb_2O_5 films. A bandgap energy of 3.42 eV has been determined for polycrystalline Nb_2O_5 films, and 3.50 for amorphous NbO_5 films.

5.2 Future Works

Based on the present outcomes several future works are recommended below:

1. Analyses of structural and physical properties of NbO_x this film on different substrate and with different interlayers are recommended be done as crystal structure of the substrate and interlayer materials affect the properties of the thin films. For example, optical grade Al_2O_3 substrate can enhance the optical properties of VO_2 thin films.
2. The detailed structural and physical properties of annealed NbO_x thin films and V doped NbO_2 thin films are recommended to be done as new phases have been formed in those films. synchrotron based X ray spectroscopy and diffraction would be useful to identify the new phases of Niobium Oxide s.
3. Investigations of Metal Insulator Transition (MIT) temperatures of NbO_2 and V doped NbO_2 thin films are very important for their application as optical switches. Since V doping can lower the transition temperature of NbO_2, it would be interesting to investigate their transition temperature by Differential Scanning Calorimetry (DSC).

References

[1] H.Y. Hwang, Y. Iwasa, M. Kawasaki, B. Keimer, N. Nagaosa, Y. Tokura, Emergent phenomena at oxide interfaces, Nature Materials. 11 (2012) 103–113. doi:10.1038/nmat3223.

[2] L.W. Martin, Y.H. Chu, R. Ramesh, Advances in the growth and characterization of magnetic, ferroelectric, and multiferroic oxide thin films, Materials Science and Engineering R: Reports. 68 (2010) 89–133. doi:10.1016/j.mser.2010.03.001.

[3] L. Bjaalie, B. Himmetoglu, L. Weston, A. Janotti, C.G. Van De Walle, Oxide interfaces for novel electronic applications, New Journal of Physics. 16 (2014). doi:10.1088/1367-2630/16/2/025005.

[4] Z. Yang, C. Ko, S. Ramanathan, Oxide Electronics Utilizing Ultrafast Metal-Insulator Transitions, Annual Review of Materials Research. 41 (2011) 337–367. doi:10.1146/annurev-matsci-062910-100347.

[5] M. Ruda, D. Farkas, J. Abriata, Interatomic potentials for carbon interstitials in metals and intermetallics, Scripta Materialia. 46 (2002) 349–355. doi:10.1016/S1359-6462(01)01250-7.

[6] H. Dosch, U. Schubert, T.H. Metzger, U. Schubert, J. Peisl, T. Bolze, H. Metzger, Diffuse X-ray scattering from interstitial nitrogen in Niobium . I . Huang diffuse scattering I . Huang diffuse scattering, (1984).

[7] M. Usta, I. Ozbek, M. Ipek, C. Bindal, A.H. Ucisik, A comparison of mechanical properties of borides formed on pure Nb and W, Materials Forum. 29 (2005) 65–70.

[8] M.J. Tallman, C. Santner, R.B. Miller, (12) United states patent, 1 (2006). doi:10.1038/incomms1464.

[9] J. Halbritter, On the Oxidation and on the Superconductivity of Niobium *, 28 (2000) 1–28.

[10] A.D. Batchelor, D.N. Leonard, P.E. Russell, F.A. Stevie, D.P. Gnffis, G.R. Myneni,

TEM and SIMS Analysis of (100), (110), and (111) Single Crystal Niobium, 72 (2007). doi:10.1063/1.2770680.

[11] N.F.O.R. Steelmaking, SCIENCE , TECHNOLOGY , INDUSTRY, 45 (2001) 34–35.

[12] C. Nico, T. Monteiro, M.P.F. Graça, Niobium oxides and niobates physical properties: Review and prospects, Progress in Materials Science. 80 (2016) 1–37. doi:10.1016/j.pmatsci.2016.02.001.

[13] I. Nowak, M. Ziolek, Niobium Compounds : Preparation , Characterization , and Application in Heterogeneous Catalysis, (1999). doi:10.1021/cr9800208.

[14] A.R. Alves, The Evolution of the Niobium Production in Brazil 1 . Historical Aspects, 18 (2015) 106–112.

[15] A. Itman Filho, R.V. Silva, W. da S. Cardoso, L.C. Casteletti, Effect of Niobium in the phase transformation and corrosion resistance of one austenitic-ferritic stainless steel, Materials Research. 17 (2014) 801–806. doi:10.1590/1516-1439.190113.

[16] F. Heisterkamp, T. Carneiro, NIOBIUM : FUTURE POSSIBILITIES – TECHNOLOGY AND THE, (n.d.).

[17] G. Tither, Progress in Niobium markets and technology 1981-2001, (2001).

[18] Y. Qi, Z. Wu, X. Zhang, C. Ma, Microstructure and phases of deposited metal of SUPER304H steel under high temperature Persistent stress, Scientific Reports. 8 (2018). doi:10.1038/s41598-018-20594-9.

[19] E.A. Chu, S., Critical Materials Strategy 2011, Energy. (2011) 191. doi:DOE/PI-0009.

[20] J. Hebda, W. Chang, Niobium alloys and high Temperature Applications, Proceedings of the International Symposium Niobium. (2001) 243–259.

[21] M.S. Rashid, T.E. Scott, Crystal structure of Niobium hydride, Journal of The Less-Common Metals. 30 (1973) 399–403. doi:10.1016/0022-5088(73)90151-3.

[22] D. Bach, H. Störmer, R. Schneider, D. Gerthsen, J. Verbeeck, EELS investigations of

different Niobium oxide phases, Microscopy and Microanalysis. 12 (2006) 416–423. doi:10.1017/S1431927606060521.

[23] F. Gervais, W. Kress, Lattice dynamics of oxides with rutile structure and instabilities at the metal-semiconductor phase transitions of NbO2 and VO2, Physical Review B. 31 (1985) 4809–4814. doi:10.1103/PhysRevB.31.4809.

[24] M.E. Straumanis, S. Zyszczynski, Lattice parameters, thermal expansion coefficients and densities of Nb, and of solid solutions Nb–O and Nb–N–O and their defect structure, Journal of Applied Crystallography. 3 (1970) 1–6. doi:10.1107/S002188987000554X.

[25] N. Terao, Structures des Oxydes de Niobium, Japanese Journal of Applied Physics. 2 (1963) 156. doi:10.1143/JJAP.2.156.

[26] F. Holtzberg, A. Reisman, M. Berry, M. Berkenblit, Chemistry of the Group VB Pentoxides. VI. The Polymorphism of Nb2O5, Journal of the American Chemical Society. 79 (1957) 2039–2043. doi:10.1021/ja01566a004.

[27] A. Taylor, N.J. Doyle, The thermal expansion of titanium, vanadium and Niobium monoxides, Journal of Applied Crystallography. 4 (1971) 103–109. doi:10.1107/S0021889871006447.

[28] G. V. Samsonov, V.I. Yakovlev, Effects of the iron-group metals upon the sintering of Niobium, Soviet Powder Metallurgy and Metal Ceramics. 14 (1975) 474–477. doi:10.1007/BF00823506.

[29] R.P. Elliott, COLUMBIUM-OXYGEN SYSTEM, Trans. Am. Soc. Metals. (n.d.).

[30] C. Nico, T. Monteiro, M.P.F. Graça, Niobium oxides and niobates physical properties: Review and prospects, Progress in Materials Science. 80 (2016) 1–37. doi:10.1016/j.pmatsci.2016.02.001.

[31] J.F. Marucco, Thermodynamic study of the system NbO2---Nb2O5 at high temperature, Journal of Solid State Chemistry. 10 (1974) 211–218. doi:10.1016/0022-4596(74)90028-0.

[32] C.N.R. Rao, G. V. Subba Rao, Transition Metal Oxides. Crystal Chemistry, Phase Transition and Related Aspects, (1975). http://nvlpubs.nist.gov/nistpubs/Legacy/NSRDS/nbsnsrds49.pdf.

[33] K. Naito, N. Kamegashira, N. Sasaki, Phase equilibria in the system between NbO2 and Nb2O5 at high temperatures, Journal of Solid State Chemistry. 35 (1980) 305–311. doi:10.1016/0022-4596(80)90526-5.

[34] M. Ronay, P. Nordlander, Barrier to oxygen penetration on metal and oxide surfaces, Physical Review B. 35 (1987) 9403–9406. doi:10.1103/PhysRevB.35.9403.

[35] P. Nordlander, M. Ronay, Calculation of the barrier for oxygen incorporation into metal and metal-oxide surfaces, Physical Review B. 36 (1987) 4982–4989. doi:10.1103/PhysRevB.36.4982.

[36] R. Pantel, M. Bujor, J. Bardolle, Continuous measurement of surface potential variations during oxygen adsorption on the (100), (110) and (111) faces of Niobium using mirror electron microscope, Surface Science. 62 (1977) 589–609. doi:10.1016/0039-6028(77)90103-0.

[37] I. Colera, S. Rey, J.L. de Segovia, Oxygen reaction on the Nb(110) surface after exposing to H2O and O2under electron bombardment, Surface Science. 251–252 (1991) 851–856. doi:10.1016/0039-6028(91)91111-A.

[38] I. Colera, J.L. de Segovia, P.L. Wincott, R. Casanova, G. Thornton, An ultraviolet photoemission study of H2O adsorption on Nb(110), Surface Science. 292 (1993) 61–66. doi:10.1016/0039-6028(93)90390-6.

[39] E.E. Latta, M. Ronay, Catalytic oxidation of Niobium, Physical Review Letters. 53 (1984) 948–951. doi:10.1103/PhysRevLett.53.948.

[40] H. Schäfer, R. Gruehn, F. Schulte, The Modifications of Niobium Pentoxide, Angewandte Chemie International Edition in English. 5 (1966) 40–52. doi:10.1002/anie.196600401.

[41] J.K. Hulm, C.K. Jones, R.A. Hein, J.W. Gibson, Superconductivity in the TiO and NbO

systems, Journal of Low Temperature Physics. 7 (1972) 291–307. doi:10.1007/BF00660068.

[42] W.W. Schulz, R.M. Wentzcovitch, Electronic Band-Structure and Bonding in Nb3O3, Physical Review B. 48 (1993) 16986–16991. doi:10.1103/PhysRevB.48.16986.

[43] M. Delheusy, X-ray investigation of Nb / O interfaces, (2008).

[44] A.M. Okaz, P.H. Keesom, Specific heat and magnetization of the superconducting monoxides: NbO and TiO, Physical Review B. 12 (1975) 4917–4928. doi:10.1103/PhysRevB.12.4917.

[45] T.W. Haas, A.G. Jackson, M.P. Hooker, Adsorption on Niobium (110), tantalum (110), and vanadium (110) surfaces, The Journal of Chemical Physics. 46 (1967) 3025–3033. doi:10.1063/1.1841173.

[46] Y. Qiu, D. Smyth, J. Kimmel, The stabilization of Niobium-based solid electrolyte capacitors, Active and Passive Electronic Components. 25 (2002) 201–209. doi:10.1080/08827510212343.

[47] C. Nico, M.R.N. Soares, J. Rodrigues, M. Matos, R. Monteiro, M.P.F. Graça, M.A. Valente, F.M. Costa, T. Monteiro, Sintered NbO powders for electronic device applications, Journal of Physical Chemistry C. 115 (2011) 4879–4886. doi:10.1021/jp110672u.

[48] R. Pynn, J. Axe, R. Thomas, Structural distortions in the low-temperature phase of NbO_{2}, Physical Review B. 13 (1976) 2965–2975. doi:10.1103/PhysRevB.13.2965.

[49] A.A. Bolzan, C. Fong, B.J. Kennedy, C.J. Howard, A powder neutron diffraction study of semiconducting and metallic Niobium dioxide, Journal of Solid State Chemistry. 113 (1994) 9–14. doi:10.1006/jssc.1994.1334.

[50] S.M. Shapiro, J.D. Axe, G. Shirane, P.M. Raccah, Neutron scattering study of the structural phase transition in NbO2, Solid State Communications. 15 (1974) 377–381. doi:10.1016/0038-1098(74)90780-7.

[51] V. Eyert, The metal-insulator transition of NbO2: An embedded Peierls instability, Europhysics Letters. 58 (2002) 851–856. doi:10.1209/epl/i2002-00452-6.

[52] N. Jiang, J.C.H. Spence, Electron energy-loss spectroscopy of the O K edge of NbO2, MoO2, and WO2, Physical Review B - Condensed Matter and Materials Physics. 70 (2004) 1–7. doi:10.1103/PhysRevB.70.245117.

[53] A. O'Hara, T.N. Nunley, A.B. Posadas, S. Zollner, A.A. Demkov, Electronic and optical properties of NbO2, Journal of Applied Physics. 116 (2014). doi:10.1063/1.4903067.

[54] D.S. Rimai, R.J. Sladek, Pressure dependences of the elastic constants of semiconducting NbO2 at 296 K, Physical Review B. 18 (1978) 2807–2811. doi:10.1103/PhysRevB.18.2807.

[55] R.F. Janninck, D.H. Whitmore, Electrical conductivity and thermoelectric power of Niobium dioxide, Solid State Communications. 4 (1966) 1183. doi:10.1016/0038-1098(66)90240-7.

[56] Y. Wang, R.B. Comes, S. Kittiwatanakul, S.A. Wolf, J. Lu, Epitaxial Niobium dioxide thin films by reactive-biased target ion beam deposition, Journal of Vacuum Science & Technology A: Vacuum, Surfaces, and Films. 33 (2015) 021516. doi:10.1116/1.4906143.

[57] A. O'Hara, A.A. Demkov, Nature of the metal-insulator transition in NbO2, Phys. Rev. B. 91 (2015) 94305. doi:10.1103/PhysRevB.91.094305.

[58] S. Helali, A. Abdelghani, I. Hafaiedh, C. Martelet, M.I. Prodromidis, T. Albanis, N. Jaffrezic-Renault, Functionalization of Niobium electrodes for the construction of impedimetric biosensors, Materials Science and Engineering C. 28 (2008) 826–830. doi:10.1016/j.msec.2007.10.078.

[59] K. Sasaki, L. Zhang, R.R. Adzic, Niobium oxide-supported platinum ultra-low amount electrocatalysts for oxygen reduction, Phys. Chem. Chem. Phys. 10 (2008) 159–167. doi:10.1039/B709893F.

[60] Y. Zhao, Z. Zhang, Y. Lin, Optical and dielectric properties of a nanostructured NbO2

thin film prepared by thermal oxidation, Journal of Physics D: Applied Physics. 37 (2004) 3392–3395. doi:10.1088/0022-3727/37/24/006.

[61] S. Kim, J. Park, J. Woo, C. Cho, W. Lee, J. Shin, G. Choi, S. Park, D. Lee, B.H. Lee, H. Hwang, Threshold-switching characteristics of a nanothin-NbO2-layer- based Pt/NbO2/Pt stack for use in cross-point-type resistive memories, Microelectronic Engineering. 107 (2013) 33–36. doi:10.1016/j.mee.2013.02.084.

[62] X. Liu, S.K. Nandi, D.K. Venkatachalam, K. Belay, S. Song, R.G. Elliman, Reduced Threshold Current in NbO2 Selector by Engineering Device Structure, IEEE Electron Device Letters. 35 (2014) 1055–1057. doi:10.1109/LED.2014.2344105.

[63] S. Lee, H. Yoon, I. Yoon, B. Kim, Single Crystalline NbO2 Nanowire Synthesis by Chemical Vapor Transport Method, Bulletin of the Korean Chemical Society. 33 (2012) 839–842. doi:Doi 10.5012/Bkcs.2012.33.3.839.

[64] F.J. Wong, N. Hong, S. Ramanathan, Orbital splitting and optical conductivity of the insulating state of NbO2, Physical Review B - Condensed Matter and Materials Physics. 90 (2014) 1–8. doi:10.1103/PhysRevB.90.115135.

[65] F.J. Wong, S. Ramanathan, Heteroepitaxy of distorted rutile-structure WO2 and NbO 2 thin films, Journal of Materials Research. 28 (2013) 2555–2563. doi:10.1557/jmr.2013.247.

[66] A.B. Posadas, A. O'Hara, S. Rangan, R.A. Bartynski, A.A. Demkov, Band gap of epitaxial in-plane-dimerized single-phase NbO2 films, Applied Physics Letters. 104 (2014) 9–14. doi:10.1063/1.4867085.

[67] G. Belanger, J. Destry, G. Perluzzo, P.M. Raccah, Electron Transport in Single Crystals of Niobium Dioxide, Canadian Journal of Physics. 52 (1974) 2272. doi:10.1139/p74-297.

[68] H.R. Philipp, L.M. Levinson, NbO2devices for subnanosecond transient protection, Journal of Applied Physics. (1979). doi:10.1063/1.326544.

[69] M.R.N. Soares, S. Leite, C. Nico, M. Peres, A.J.S. Fernandes, M.P.F. Graça, M. Matos,

R. Monteiro, T. Monteiro, F.M. Costa, Effect of processing method on physical properties of Nb2O5, Journal of the European Ceramic Society. 31 (2011) 501–506. doi:10.1016/j.jeurceramsoc.2010.10.024.

[70] R.A. Rani, A.S. Zoolfakar, A.P. O'Mullane, M.W. Austin, K. Kalantar-Zadeh, Thin films and nanostructures of Niobium pentoxide: fundamental properties, synthesis methods and applications, J. Mater. Chem. A. 2 (2014) 15683–15703. doi:10.1039/C4TA02561J.

[71] K. Kato, S. Tamura, Die Kristallstruktur von T-Nb2O5, Acta Crystallographica Section B Structural Crystallography and Crystal Chemistry. 31 (1975) 673–677. doi:10.1107/S0567740869004195.

[72] R. Brayner, F. Bozon-Verduraz, Niobium pentoxide prepared by soft chemical routes: Morphology, structure, defects and quantum size effect, Physical Chemistry Chemical Physics. 5 (2003) 1457–1466. doi:10.1039/b210055j.

[73] E. Sian Crawford, J.S. Anderson, Homogenenous solid state transformations in Niobium oxides, Philosophical Transactions of the Royal Society of London A. 304 (1982) 327–364. doi:10.1098/rspa.1952.0029.

[74] R.. K.O.. J.R.. W.M.. c Venkataraj S.a b Drese, Characterization of Niobium oxide films prepared by reactive DC magnetron sputtering, Physica Status Solidi (A) Applied Research. 188 (2001) 1047–1058. doi:10.1002/1521-396X(200112)188:3<1047::AID-PSSA1047>3.0.CO;2-J.

[75] B.M. Gatehouse, A.D. Wadsley, The Crystal Structure of the High Temperature form of Niobium Pentaoxide, Acta Crystallographica. 17 (1964) 1545–1554. doi:10.1107/S0567740869006005.

[76] S. Venkataraj, R. Drese, C. Liesch, O. Kappertz, R. Jayavel, M. Wuttig, Temperature stability of sputtered Niobium-oxide films, Journal of Applied Physics. 91 (2002) 4863–4871. doi:10.1063/1.1458052.

[77] C. Valencia-Balvín, S. Pérez-Walton, G.M. Dalpian, J.M. Osorio-Guillén, First-

principles equation of state and phase stability of Niobium pentoxide, Computational Materials Science. 81 (2014) 133–140. doi:10.1016/j.commatsci.2013.07.032.

[78] J. Eckert, H.C.S. Berlin, W. Goslar, F. Republic, Niobium and Niobium Compounds, Ullmanns Encyclopedia of Industrial Chemistry. (2005). doi:10.1002/14356007.a17_251.pub2.

[79] N. Özer, T. Barreto, T. Büyüklimanli, C.M. Lampert, Characterization of sol-gel deposited Niobium pentoxide films for electrochromic devices, Solar Energy Materials and Solar Cells. 36 (1995) 433–443. doi:10.1016/0927-0248(94)00197-9.

[80] Z. Weibin, W. Weidong, W. Xueming, C. Xinlu, Y. Dawei, S. Changle, P. Liping, W. Yuying, B. Li, The investigation of NbO2 and Nb2O5 electronic structure by XPS, UPS and first principles methods, Surface and Interface Analysis. 45 (2013) 1206–1210. doi:10.1002/sia.5253.

[81] Ö.D. Coşkun, S. Demirel, The optical and structural properties of amorphous Nb2O 5 thin films prepared by RF magnetron sputtering, Applied Surface Science. 277 (2013) 35–39. doi:10.1016/j.apsusc.2013.03.116.

[82] T. Blanquart, J. Niinistö, M. Heikkilä, T. Sajavaara, K. Kukli, E. Puukilainen, C. Xu, W. Hunks, M. Ritala, M. Leskelä, M. Leskela, Evaluation and Comparison of Novel Precursors for Atomic Layer Deposition of Nb2O5 Thin Films, Chem. Mater. 24 (2012) 975–980. doi:10.1021/cm2026812.

[83] M. Vinnichenko, A. Rogozin, D. Grambole, F. Munnik, A. Kolitsch, W. Möller, O. Stenzel, S. Wilbrandt, A. Chuvilin, U. Kaiser, Highly dense amorphous Nb2 O5 films with closed nanosized pores, Applied Physics Letters. 95 (2009). doi:10.1063/1.3212731.

[84] M.F. Pillis, G.A. Geribola, G. Scheidt, E.G. de Araújo, M.C.L. de Oliveira, R.A. Antunes, Corrosion of thin, magnetron sputtered Nb2O5 films, Corrosion Science. 102 (2016) 317–325. doi:10.1016/j.corsci.2015.10.023.

[85] S. Clima, G. Pourtois, A. Hardy, S. Van Elshocht, M.K. Van Bael, S. De Gendt, D.J.

Wouters, M. Heyns, J.A. Kittl, Dielectric Response of Ta2O5, Nb2O5, and NbTaO5 from First-Principles Investigations, J. Electrochem. Soc. 157 (2010) G20–G25. doi:10.1149/1.3253583.

[86] L.C.A. Oliveira, T.C. Ramalho, M. Gonçalves, F. Cereda, K.T. Carvalho, M.S. Nazzarro, K. Sapag, Pure niobia as catalyst for the oxidation of organic contaminants: Mechanism study via ESI-MS and theoretical calculations, Chemical Physics Letters. 446 (2007) 133–137. doi:10.1016/j.cplett.2007.08.037.

[87] L. Berger, H. Mähne, V. Klemm, A. Leuteritz, T. Mikolajick, D. Rafaja, Thermally activated crystallization of Nb 2O 5 grown on Pt electrode, Applied Physics A: Materials Science and Processing. 108 (2012) 431–437. doi:10.1007/s00339-012-6905-7.

[88] X. Liu, S.M. Sadaf, S. Park, S. Kim, E. Cha, D. Lee, G.Y. Jung, H. Hwang, Complementary resistive switching in Niobium oxide-based resistive memory devices, IEEE Electron Device Letters. 34 (2013) 235–237. doi:10.1109/LED.2012.2235816.

[89] A. Kohli, C.C. Wang, S.A. Akbar, Niobium pentoxide as a lean-range oxygen sensor, Sensors and Actuators, B: Chemical. 56 (1999) 121–128. doi:10.1016/S0925-4005(99)00191-4.

[90] I. Lindau, W.E. Spicer, Oxidation of Nb as studied by the uv-photoemission technique, Journal of Applied Physics. (1974). doi:10.1063/1.1663849.

[91] N. Norman, Metallic oxide phases of Niobium and tantalum I. X-ray investigations, Journal of The Less-Common Metals. (1962). doi:10.1016/0022-5088(62)90059-0.

[92] K. Obara, OXIDATION PROCESS OF METASTABLE SUPER-FINE NIOBIUM OXIDE PARTICLES, 99 (1990) 192–195.

[93] N. Norman, P. Kofstad, O.J. Krudtaa, Metallic oxide phases of Niobium and tantalum II. Metallographic studies, Journal of The Less-Common Metals. 4 (1962) 124–137. doi:10.1016/0022-5088(62)90011-5.

[94] Investigation of Metastable Niobium Oxides by Transmission Electron Microscopy, Comments on Inorganic Chemistry. 1 (1982) 361–377.

doi:10.1080/02603598208078104.

[95] R. Ghosh, M.K. Brennaman, T. Uher, M.-R. Ok, E.T. Samulski, L.E. McNeil, T.J. Meyer, R. Lopez, Nanoforest Nb2O5 photoanodes for dye-sensitized solar cells by pulsed laser deposition., ACS Applied Materials & Interfaces. 3 (2011) 3929–35. doi:10.1021/am200805x.

[96] M. Grundner, J. Halbritter, XPS and AES studies on oxide growth and oxide coatings on Niobium, Journal of Applied Physics. 51 (1980) 397–405. doi:10.1063/1.327386.

[97] L. Ben-dor, Y. Shimony, Crystal growth and phase transitions in the NbxCr1-xO2(x ≥ 0.5) system, Journal of Crystal Growth. 43 (1978) 1–4. doi:10.1016/0022-0248(78)90361-5.

[98] K. Kukli, M. Ritala, M. Leskelä, Properties of atomic layer deposited (Ta1−xNbx)2O5 solid solution films and Ta2O5–Nb2O5 nanolaminates, Journal of Applied Physics. 86 (1999) 5656–5662. doi:10.1063/1.371576.

[99] C.N.R. Rao, G.R. Rao, G.V.S. Rao, Semiconductor-metal transitions in NbO_2 and Nb1−xVxO2, Journal of Solid State Chemistry. 6 (1973) 340–343. doi:10.1016/0022-4596(73)90219-3.

[100] C.N.R. Rao, M. Natarajan, G. V. Subba Rao, R.E. Loehman, Phase transitions and conductivity anomalies in solid solutions of VO2with TiO2, NbO2, and MoO2, Journal of Physics and Chemistry of Solids. 32 (1971) 1147–1150. doi:10.1016/S0022-3697(71)80172-5.

[101] C.N.R. Rao, G.R. Rao, G.V.S. Rao, Semiconductor-metal transitions in NbO2and Nb1-xVxO2, Journal of Solid State Chemistry. (1973). doi:10.1016/0022-4596(73)90219-3.

[102] G. Villeneuve, A. Bordet, A. Casalot, J.P. Pouget, H. Launois, P. Lederer, Contribution to the study of the metal-insulator transition in the V1−xNbxO2 system: I — crystallographic and transport properties, Journal of Physics and Chemistry of Solids. (1972). doi:10.1016/S0022-3697(72)80494-3.

[103] G. Bräuer, B. Szyszka, M. Vergöhl, R. Bandorf, Magnetron sputtering - Milestones of

30 years, in: Vacuum, 2010: pp. 1354–1359. doi:10.1016/j.vacuum.2009.12.014.

[104] A. Anders, Plasma and ion sources in large area coating: A review, Surface and Coatings Technology. 200 (2005) 1893–1906. doi:10.1016/j.surfcoat.2005.08.018.

[105] A.P. Ehiasarian, W.D. Münz, L. Hultman, U. Helmersson, I. Petrov, F. Seitz, High power pulsed magnetron sputtered CrNxfilms, Galvanotechnik. (2003). doi:10.1016/S0257-8972(02)00479-6.

[106] A. Anders, Tutorial: Reactive high power impulse magnetron sputtering (R-HiPIMS), Journal of Applied Physics. 121 (2017). doi:10.1063/1.4978350.

[107] J. Böhlmark, Fundamentals of High Power Impulse Magnetron Sputtering, 2006. doi:10.1063/1.3700242.

[108] P. Sigmund, Theory of sputtering. I. Sputtering yield of amorphous and polycrystalline targets, Physical Review. 184 (1969) 383–416. doi:10.1103/PhysRev.184.383.

[109] D. Depla, S. Mahieu, J.E. Greene, Sputter Deposition Processes, in: Handbook of Deposition Technologies for Films and Coatings, 2010: pp. 253–296. doi:10.1016/B978-0-8155-2031-3.00005-3.

[110] A. Anders, A structure zone diagram including plasma-based deposition and ion etching, Thin Solid Films. (2010). doi:10.1016/j.tsf.2009.10.145.

[111] E.N. Kaufmann, Characterization of Materials, 2008. http://medcontent.metapress.com/index/A65RM03P4874243N.pdf.

[112] E. Smith, G. Dent, Modern Raman Spectroscopy - A Practical Approach, 2005. doi:10.1002/0470011831.

[113] P. Larkin, P. Larkin, Chapter 2 – Basic Principles, in: Infrared and Raman Spectroscopy, 2011: pp. 7–25. doi:10.1016/B978-0-12-386984-5.10002-3.

[114] P.J. Larkin, J. Wasylyk, M. Raglione, Application of Low- and Mid-Frequency Raman Spectroscopy to Characterize the Amorphous-Crystalline Transformation of

Indomethacin, Applied Spectroscopy. 69 (2015) 1217–1228. doi:10.1366/15-07926.

[115] W. Sun, J. Sun, L. Du, C. Du, Y. Gao, G. Yin, Synthesis of Nitrogen-doped Niobium Dioxide and its co-catalytic effect towards the electrocatalysis of oxygen reduction on platinum, Electrochimica Acta. 195 (2016) 166–174. doi:10.1016/j.electacta.2016.02.122.

[116] M.P.F. Graça, A. Meireles, C. Nico, M.A. Valente, Nb2O5 nanosize powders prepared by sol–gel – Structure, morphology and dielectric properties, Journal of Alloys and Compounds. 553 (2013) 177–182. doi:10.1016/j.jallcom.2012.11.128.

[117] Y. Lin, Y.J. Yang, C.C. Hsu, Synthesis of Niobium oxide nanowires using an atmospheric pressure plasma jet, Thin Solid Films. 519 (2011) 3043–3049. doi:10.1016/j.tsf.2010.12.024.

[118] M.P.F. Graça, M. Saraiva, F.N.A. Freire, M.A. Valente, L.C. Costa, Electrical analysis of Niobium oxide thin films, Thin Solid Films. 585 (2015) 95–99. doi:10.1016/j.tsf.2015.02.047.

[119] H. Stanjek, W. Häusler, Introduction To Powder/ Polycrystalline Diffraction, Hyperfine Interactions. 154 (2004) 107–119. doi:10.1023/B:HYPE.0000032028.60546.38.

[120] R. Govindaraj, R. Kesavamoorthy, R. Mythili, B. Viswanathan, The formation and characterization of silver clusters in zirconia, Journal of Applied Physics. 90 (2001) 958–963. doi:10.1063/1.1382831.

[121] P. van der Heide, X-Ray Photoelectron Spectroscopy. An Introduction to Principles and Practices, 2011. doi:10.1002/9781118162897.

[122] S. Nigo, M. Kubota, Y. Harada, T. Hirayama, S. Kato, H. Kitazawa, G. Kido, Conduction band caused by oxygen vacancies in aluminum oxide for resistance random access memory, Journal of Applied Physics. 112 (2012). doi:10.1063/1.4745048.

[123] Asm, ASM Handbook Volume 10 Materials Characterization, in: ASM Handbook, 1998.

[124] K.D. Vernon-Parry, Scanning electron microscopy: an introduction, III-Vs Review. 13

(2000) 40–44. doi:10.1016/S0961-1290(00)80006-X.

[125] J.I. Goldstein, D.E. Newbury, P. Echlin, D.C. Joy, C.E. Lyman, E. Lifshin, L. Sawyer, J.R. Michael, Scanning Electron Microscopy and X-ray Microanalysis, 2003. doi:10.1007/978-1-4615-0215-9.

[126] M. Ohring, Characterization of Thin Films and Surfaces, in: Materials Science of Thin Films, 2002: pp. 559–640. doi:10.1016/B978-012524975-1/50013-6.

[127] W. Oliver, G. Pharr, An improved technique for determining hardness and elastic modulus using load and displacement-sensing indentation systems, Journal of Materials Research. 7 (1992) 1564–1583. doi:10.1557/JMR.1992.1564.

[128] J. Alkorta, J.M. Martínez-Esnaola, J. Gil Sevillano, Detailed assessment of indentation size-effect in recrystallized and highly deformed Niobium, Acta Materialia. 54 (2006) 3445–3452. doi:10.1016/j.actamat.2006.03.034.

[129] J.A. Knapp, D.M. Follstaedt, S.M. Myers, J.C. Barbour, T.A. Friedmann, Finite-element modeling of nanoindentation, Journal of Applied Physics. 85 (1999) 1460–1474. doi:10.1063/1.369178.

[130] PerkinElmer Instruments, Lambda 800/900 User's Guide, (2001). UserAssistance@perkinelmer.com.

[131] P. Muhammed Shafi, A. Chandra Bose, Impact of crystalline defects and size on X-ray line broadening: A phenomenological approach for tetragonal SnO<inf>2</inf> nanocrystals, AIP Advances. 5 (2015). doi:10.1063/1.4921452.

[132] G.K. Williamson, W.H. Hall, X-ray line broadening from filed aluminium and wolfram, Acta Metallurgica. (1953). doi:10.1016/0001-6160(53)90006-6.

[133] X. Feng, Y. Huang, A.J. Rosakis, On the Stoney Formula for a Thin Film/Substrate System With Nonuniform Substrate Thickness, Journal of Applied Mechanics. 74 (2007) 1276. doi:10.1115/1.2745392.

[134] R. Swanepoel, Determination of surface roughness and optical constants of

inhomogeneous amorphous silicon films, Journal of Physics E: Scientific Instruments. (1984). doi:10.1088/0022-3735/17/10/023.

[135] W. Sellmeier, II. Ueber die durch Aetherschwingungen erregten Mitschwingungen der Körpertheilchen und deren Rückwirkung auf die ersteren, besonders zur Erklärung der Dispersion und ihrer Anomalien, Annalen Der Physik. (1872). doi:10.1002/andp.18722210403.

[136] S. Kasap and P. Capper, Optical Properties of Electronic Materials: Fundamentals and Characterization, in: Springer Handbook of Electronic and Photonic Materials, Second Edition, Springer, Heidelberg, Chapter 3., 2017: pp. 47–83. doi:10.1007/978-3-319-48933-9.

[137] A.D.E.R. Physik, N. Vol, (Beiträge zur Optik trüber Medien , speziell kolloidaller Metallösungen ; von Gustav Mie), Optik. (1908).

[138] A.K.R. S.O. Kasap, W.C. Tan, Jai Singh, Fundamental Optical Properties of Materials I, in: Optical Properties of Condensed Matter and Applications, Second Edition, Ed J. Singh (Wiley and Sons, Chichester, 2019) Chapter 1, 2019. doi:10.1007/s13398-014-0173-7.2.

[139] J. Tauc, Optical properties and electronic structure of amorphous Ge and Si, Materials Research Bulletin. (1968). doi:10.1016/0025-5408(68)90023-8.

[140] A.P. Sokolov, A.P. Shebanin, O.A. Golikova, M.M. Mezdrogina, Structural disorder and optical gap fluctuations in amorphous silicon, Journal of Physics: Condensed Matter. 3 (1991) 9887–9894. doi:10.1088/0953-8984/3/49/005.

[141] M. Mozetič, U. Cvelbar, M.K. Sunkara, S. Vaddiraju, A Method for the Rapid Synthesis of Large Quantities of Metal Oxide Nanowires at Low Temperatures, Advanced Materials. 17 (2005) 2138–2142. doi:10.1002/adma.200500728.

[142] V. V. Atuchin, I.E. Kalabin, V.G. Kesler, N. V. Pervukhina, Nb 3d and O 1s core levels and chemical bonding in niobates, Journal of Electron Spectroscopy and Related Phenomena. 142 (2005) 129–134. doi:10.1016/j.elspec.2004.10.003.

[143] M. Kang, S. Yu, J. Son, Voltage-induced insulator-to-metal transition of hydrogen-treated NbO2thin films, Journal of Physics D: Applied Physics. 48 (2015). doi:10.1088/0022-3727/48/9/095301.

[144] D. Music, R.W. Geyer, Theoretical and experimental study of NbO $_2$ nanoslice formation, Journal of Physics D: Applied Physics. 48 (2015) 305302. doi:10.1088/0022-3727/48/30/305302.

[145] A. Le Viet, M.V. Reddy, R. Jose, B.V.R. Chowdari, S. Ramakrishna, Electrochemical properties of bare and Ta-substituted Nb2O5 nanostructures, Electrochimica Acta. 56 (2011) 1518–1528. doi:10.1016/j.electacta.2010.10.047.

[146] S.A. O'Neill, I.P. Parkin, R.J.H. Clark, A. Mills, N. Elliott, Atmospheric pressure chemical vapour deposition of thin films of Nb2O5 on glass, Journal of Materials Chemistry. 13 (2003) 2952–2956. doi:Doi 10.1039/B307768n.

[147] A. Foroughi-Abari, K.C. Cadien, Growth, structure and properties of sputtered Niobium oxide thin films, Thin Solid Films. 519 (2011) 3068–3073. doi:10.1016/j.tsf.2010.12.036.

[148] W.D. Nix, B.M. Clemens, Crystallite coalescence: A mechanism for intrinsic tensile stresses in thin films, Journal of Materials Research. 14 (1999) 3467–3473. doi:10.1557/JMR.1999.0468.

[149] C.-C. Lee, C.-L. Tien, J.-C. Hsu, Internal stress and optical properties of Nb_2O_5 thin films deposited by ion-beam sputtering, Applied Optics. 41 (2002) 2043. doi:10.1364/AO.41.002043.

[150] E. Cetinörgü-Goldenberg, J.-E. Klemberg-Sapieha, L. Martinu, Effect of postdeposition annealing on the structure, composition, and the mechanical and optical characteristics of Niobium and tantalum oxide films., Applied Optics. 51 (2012) 6498–507. doi:10.1364/AO.51.006498.

[151] G. Ramírez, S.E. Rodil, S. Muhl, D. Turcio-Ortega, J.J. Olaya, M. Rivera, E. Camps, L. Escobar-Alarcón, Amorphous Niobium oxide thin films, Journal of Non-Crystalline

Solids. 356 (2010) 2714–2721. doi:10.1016/j.jnoncrysol.2010.09.073.

[152] D.E. Kramer, A.A. Volinsky, N.R. Moody, W.W. Gerberich, Substrate effects on indentation plastic zone development in thin soft films, Journal of Materials Research. 16 (2001) 3150–3157. doi:10.1557/JMR.2001.0434.

[153] T. Onozato, T. Katase, A. Yamamoto, S. Katayama, K. Matsushima, N. Itagaki, H. Yoshida, H. Ohta, Optoelectronic properties of valence-state-controlled amorphous Niobium oxide, Journal of Physics Condensed Matter. 28 (2016). doi:10.1088/0953-8984/28/25/255001.

[154] A.K. Jonscher, Electronic processes in non-crystalline materials, Thin Solid Films. (1972). doi:10.1016/0040-6090(72)90068-5.

[155] C. Marini, E. Arcangeletti, D. Di Castro, L. Baldassare, A. Perucchi, S. Lupi, L. Malavasi, L. Boeri, E. Pomjakushina, K. Conder, P. Postorino, Optical properties of V1-x Crx O2 compounds under high pressure, Physical Review B - Condensed Matter and Materials Physics. (2008). doi:10.1103/PhysRevB.77.235111.

[156] E. Arcangeletti, L. Baldassarre, D. Di Castro, S. Lupi, L. Malavasi, C. Marini, A. Perucchi, P. Postorino, Evidence of a pessure-induced metallization process in monoclinic VO2, Physical Review Letters. (2007). doi:10.1103/PhysRevLett.98.196406.

[157] M. Yang, Y. Yang, B. Hong, L. Wang, K. Hu, Y. Dong, H. Xu, H. Huang, J. Zhao, H. Chen, L. Song, H. Ju, J. Zhu, J. Bao, X. Li, Y. Gu, T. Yang, X. Gao, Z. Luo, C. Gao, Suppression of Structural Phase Transition in VO2by Epitaxial Strain in Vicinity of Metal-insulator Transition, Scientific Reports. (2016). doi:10.1038/srep23119.

[158] C. Zhang, Q. Yang, C. Koughia, F. Ye, M. Sanayei, S.J. Wen, S. Kasap, Characterization of vanadium oxide thin films with different stoichiometry using Raman spectroscopy, Thin Solid Films. 620 (2016) 64–69. doi:10.1016/j.tsf.2016.07.082.

[159] A.A. McConnell, J.S. Aderson, C.N.R. Rao, Raman spectra of Niobium oxides, Spectrochimica Acta Part A: Molecular Spectroscopy. 32 (1976) 1067–1076.

doi:10.1016/0584-8539(76)80291-7.